FINITE ELEMENT ANALYSIS OF TOTAL KNEE REPLACEMENT CONSIDERING GAIT CYCLE LOAD AND MALALIGNMENT

JUNFEN SHI

A thesis submitted in partial fulfilment of the
requirements of the University of Wolverhampton
for the degree of Doctor of Philosophy

June 2007

This work or any part thereof has not previously been presented in any form to the University or to any other body whether for the purposes of assessment, publication or for any other purpose (unless otherwise indicated). Save for any express acknowledgments, references and/or bibliographies cited in the work, I confirm that the intellectual content of the work is the result of my own efforts and of no other person.

Signature……..

Date……..

Abstract

This research has investigated the influence of gait cycle, malalignment and overweight on total knee replacements using a finite element method.

Dynamic and finite element models of fixed- and mobile-bearing implants have been created and solved; the fixed- and mobile-bearing implants demonstrated different performance on movement and contact pressure distribution in the tibio-femoral contact surfaces. More contact areas were found in the mobile-bearing implant than in the fixed-bearing implant, but the maximum contact pressures were almost the same in both. The thickness of the tibial bearing component influenced the fixed- and mobile-bearing implants differently.

A dynamic model of an implanted knee joint has been developed using MSC/ADAMS and MSC/MARC software. Stress shielding was found in the distal femur in the implanted knee joint. The stresses and strains in the distal femur were found to increase with body weight, especially during the stance phase. Serious stress shielding and more bone loss appear in condition of overweight. The increase of bone loss rate and stress in the distal femur with increase of body weight will result in a higher risk of migration of femoral component after total knee replacement. The peg size effect has been studied using this dynamic model; a longer peg with smaller diameter was found to be the best.

Varus/valgus malalignment redistributed the tibio-femoral contact force and stress/strain distribution in the distal femur. The difference between contact forces on the medial and lateral condyle decreased in the valgus malalignment condition. Contact pressure increased in the varus/valgus malalignment condition in the dynamic models of both the fixed- and mobile-bearing implant. However, the mobile-bearing implant performed better in conditions of malalignment, especially malrotation. Body weight had less influence on the maximum contact pressure in the mobile-bearing implant.

Acknowledgements

First and foremost I want to thank my supervisor Dr. Changjiang Wang. Without him, this dissertation would not have been possible. I thank him for his patience and encouragement that carried me on through difficult times, and for his insights and suggestions that helped to shape my research skills. His valuable ideas and feedback contributed greatly to this dissertation. I improved my knowledge in biomechanics, especially in finite element method applications, under his guidance.

I am grateful to my research adviser Dr. William Hart at New Cross hospital, Wolverhampton. He helped me to learn more about the clinical performance of a total knee replacement and gave valuable suggestions on my simulation models. I appreciate his contribution to the clinical aspect of this research. I also thank Dr. Tahar Laoui and Prof. Richard Hall, who advised me and helped me in various aspects of my research. I would also like to thank Dr. Fiona Berryman, who helped me to improve my English and shared her valuable research experience with me. I am also grateful to Julian Spence for his support on computer clusters and help on finite element modelling. I thank all other staff, students and friends, who gave me support in research and life, during the course of the project.

Last but not least, I thank my family, especially my husband, for always being there when I needed them most, and for supporting me through all these years.

Table of Contents

List of Figures

List of Tables

Nomenclature

ACL	Anterior cruciate ligament
AP	Anterior/posterior translation of tibia
BMD	Bone mineral density
BMI	Body mass index
BMU	Basic multicellular unit of bone
CT	Computed tomography
F/E	Flexion/extension of knee joint
FEM	Finite element method
IC	Initial contact at stance phase of gait cycle
ISw	Initial swing of gait cycle
L1-L10	Different zones of distal femur at lateral side
LCL	Lateral collateral ligament
LR	Load response at stance phase of gait cycle
M3-M10	Different zones of distal femur at medial side
MCL	Medial collateral ligament
ML	Medial/lateral translation of tibia
MSt	Mid-stance at stance phase of gait cycle
MSw	Mid-swing of gait cycle
PCL	Posterior cruciate ligament
PDTA	Sagittal posterior-distal transition angle of femoral component
PMMA	Polymethylmethacrylate
PSw	Pre-swing at stance phase of gait cycle
RAT	Sagittal anterior radius of tibial bearing component
RDF	Sagittal distal radius of femoral component

RFF	Frontal radius of femoral component
RFT	Frontal radius of tibial bearing component
RIF	Frontal inner radius of femoral component
RIT	Frontal inner radius of tibial bearing component
ROF	Frontal outer radius of femoral component
ROT	Frontal outer radius of tibial bearing component
RPF	Sagittal posterior radius of femoral component
RPSF	Sagittal posterior-superior radius of femoral component
RPT	Sagittal posterior radius of tibial bearing component
RSDF	Sagittal distal radius of femoral component
RSPF	Sagittal posterior radius of femoral component
RST	Sagittal radius of tibial bearing component
SED	Strain energy density
TKR	Total knee replacement
TSt	Terminal stance at stance phase of gait cycle
TSw	Terminal swing of gait cycle
UHMWPE	Ultra high molecular weight polyethylene
ε	Strain symbol
ρ	Bone density
σ	Stress symbol
$C(n,P)$	Coefficient of external bone remodelling
$\dot{D}_F$	Bone fatigue damage formation rate
$\dot{D}_R$	Bone fatigue damage formation rate
$\frac{dn}{dt}$	Bone remodelling at point P

$\frac{dM}{dt}$	Rate of net bone mass turnover
N_F	Density of refilling BMUs/area
N_R	Density of resorbing BMUs/area
p	Bone porosity
Q_F	Bone refilling rate for each BMU
Q_R	Bone resorbing rate for each BMU
S	Bone remodelling signal
s	Bone remodelling threshold
S_{ref}	Bone remodelling signal at same place of corresponding intact bone
u	Strain energy density symbol

Glossary

Abduction	Movement of a bone away from the midline
Adduction	Movement of a bone towards the midline
Arthritis	Inflammation of a joint, usually accompanied by pain, swelling, and sometimes change in structure
Arthroplasty	A surgical procedure in which an artificial joint replaces a damaged joint, usually a hip, knee, shoulder or ankle
Contralateral	Term used to describe the relative location of structures. Contralateral indicates that the structure is located on the opposite side of the body compared to the reference structure
Coronal plane	Divides the body into front and rear sections
Diaphysis	Shaft of a long bone
Endosteum	A membrane lining the medullary cavity within a bone
Epiphysis	The end of a long bone that contains spongy bone tissue
Ipsilateral	Term used to describe the relative location of structures. Ipsilateral indicates that the structure is located on the same side of the body as the reference structure
Metaphysis	The flared area of junction of the epiphysis with the diaphysis of a long bone
Obesity	An increase in the body weight greater than that required for normal function that is characterised by the accumulation of excessive fat
Osteoporosis	Abnormal reduction in quantity of bone tissue; a condition that develops when bone is no longer replaced as quickly as it is removed
Periosteum	The tough fibrous membrane surrounding a bone

Prosthesis	An artificial substitute for a missing body part, such as a hip, knee, shoulder or ankle joint
Sagittal plane	Divides the body into right and left sections
Transverse plane	Divides the body into upper and lower sections
Valgus	Tibia abduct with respect to femur
Varus	Tibia adduct with respect to femur

Chapter 1

Introduction

1.1 Introduction

Zihlmann *et al.* reported in 2005 that about 440,000 total knee replacements (TKR) are carried out worldwide each year. Because of adiposity and a higher life expectancy, the number of TKR implantations will increase in the future. Although the patient satisfaction rate is around 90% (D'Lima *et al.* 2001), the number of patient who need revision surgery is significant. Annually, 35,000 TKR are revised worldwide (Sharkey *et al.* 2002). The main reasons for TKR failure are: early wear of the ultra high molecular weight polyethylene (UHMWPE), aseptic loosening, tibial femoral instability, patellar instability, and fatigue failure of the tibial tray (Villa *et al.* 2004). Polyethylene wear and aseptic loosening are the most common reasons for TKR revision.

Early wear of UHMWPE is affected by the conformity of the articulating surfaces, the thickness of the polyethylene component and the elastic modulus of the polyethylene (Petty et al. 1999). It is also influenced by contact loads and surface kinematics (Bei et al. 2004, Fregly et al. 2003, McEwen et al. 2005). Multidirectional motion on tibio-femoral joint contributes to greater polyethylene wear. UHMWPE wear generates wear particles and may lead to osteolysis and long-term implant loosening (McEwen et al. 2001). Early wear of UHMWPE is related to the extension of contact areas and to the magnitude of contact pressure. The contact pressure and areas depend on the degree of conformity and operative techniques including mechanical alignment and fixation of the components. Wear can also lead to malalignment or instability of the knee joint. The limb alignment and the shape of the articulating surface strongly influence the bone-implant interface stress and the stress distribution in implanted bones. It is found that aseptic loosening usually results from malalignment (Vince 2003). Also long-term bone remodelling surrounding knee components controlled by mechanical stress will increase the degree of

malalignment. Malalignment is the main reason for polyethylene wear and aseptic loosening; however, malalignment is also the result of polyethylene wear and aseptic loosening.

The long-term performance of total knee replacement is dependent on the kinematics of knee joint. Retrieval studies have shown that the wear of total knee replacements is highly variable and this is attributable to the diverse kinematic and stress conditions that occur in vivo. Gait load is also an important factor influence TKR performance.

Longitudinal data have shown that obesity is a powerful risk factor in the development of knee osteoarthritis. With the global increase of obese TKR patients, the effect of obesity on the outcome of TKR needs to be investigated.

This research investigated the influence of gait cycle, malalignment and excessive body weight on total knee implants and the bone structure in the distal femur.

1.2 Structure of the thesis

The thesis consists of ten chapters.

Chapter 1 is the introduction giving an outline of the research and the structure of the thesis.

Chapter 2 introduces the structure of a knee joint. Motion of the knee joint and forces in the knee joint during the gait cycle are described.

Chapter 3 introduces the concept of total knee replacement. In this chapter, different types of knee replacement are introduced and failures of total knee replacement are reviewed.

In **Chapter 4**, stress distributions in fixed- and mobile-bearing implants in different conditions of malalignment and at three stages of gait cycle are compared using finite element methods. The influences of malalignment on fixed- and mobile-bearing implants are investigated.

In **Chapter 5,** the dynamic performance of fixed- and mobile-bearing implants is investigated. Using dynamic analysis and finite element models, motion and stress distribution during gait cycle are compared between fixed- and mobile-bearing implants in conditions of normal alignment and varus/valgus malalignment. The influence of the thickness of the tibial bearing component is discussed in this chapter.

In **Chapter 6**, dynamic stress models of an implanted knee joint are developed by combining MSC/ADAMS and MSC/MARC software. Stress distributions in the distal femur of an implanted and an intact joint are compared; stress shielding is clearly found in the implanted distal femur. The stress distributions in the distal femur in conditions of varus/valgus malalignment are systematically demonstrated and explained.

In **Chapter 7**, several designs of femoral component with various peg sizes are compared by examining the stress distributions in the distal femur. The stress shielding at the distal end of the femur after a TKR have been found to appear in all designs.

In **Chapter 8**, the influence of body weight on total knee replacement is investigated. Increased body weight results in increased stress and strain in the distal femur. Increased body weight also results in increased contact pressure on the tibial bearing component. The mobile-bearing implant is less affected by increased body weight and performs better than fixed-bearing implant in overweight patients.

Chapter 9 summarises the main findings and reports the conclusions of this research.

Chapter 10 is the last chapter of the thesis; it puts forward some recommendations for future work.

1.3 Original contribution to the body of knowledge

The original contributions of this thesis to the body of knowledge are:

- The dynamic performance of fixed- and mobile-bearing knee implants during the gait cycle is analysed and compared. Variations in maximum contact pressure during the gait cycle are investigated.

- The stress distribution in fixed- and mobile-bearing implants in different conditions of malalignment is analysed and compared; this is used to explain their performance.

- The influence of the thickness of the tibial bearing component and body weight on tibio-femoral contact pressure in fixed- and mobile-bearing implants is studied.

- Sophisticated dynamic models of the implanted knee joint are developed. Variation of stress in the distal femur during the gait cycle can be obtained from this model and used for further analysis.

- The influence of the femoral component peg design on stress distribution after TKR is investigated and shows the stress shielding in the distal femur.

- The effect of excessive body weight on TKR is comparatively analysed with normal weight patients

The above points collectively contribute to the body of knowledge on the performance characteristics of TKR. The main contribution of the research is to create a dynamic model of the implanted knee joint. This work is the first to combine movement of the knee with analysis of stress in the TKR during the gait cycle. Analysis of the TKR using the created model will definitely improve the design of total knee prostheses.

Chapter 2

The knee joint

2.1 Anatomy of the knee

The knee is the largest joint in the body and it is also one of the most complex joints. The knee joint is made up of four bones: femur, tibia, fibula and patella. The articulation of these bones forms the knee joint, and is shown in Figure 2-1, which is adopted from website http://www.aclsolutions.com/default.php. The two major articulations within the knee are the tibio-femoral and patello-femoral joints.

2.1.1 Tibio-femoral joint

In the knee, the distal end of the femur has a curved articular surface that is shaped somewhat like a 'horseshoe' with the bend of the 'horseshoe' in the front of the femur. The two ends of the femur extend backward, and are called the medial and lateral condyles. These surfaces articulate with the medial and lateral tibial condyles, forming the tibio-femoral joint, which flexes and extends the knee. Two fibro-cartilaginous discs (meniscus) lie between the tibial and femoral condyles to compensate for the incongruence of the articulating bones.

2.1.2 Patello-femoral joint

The patella, or what we call the kneecap, glides up and down on the front surface of the femur bone as the knee flexes and extends. Articulations of patella and femur form the patello-femoral joint. The patella is held in place at the front of the knee joint by:

- The quadriceps muscle which is located in the front of the thigh and used to extend (straighten) the leg.
- The quadriceps tendon which connects to the quadriceps muscle above the knee and covers the knee joint.

- The patellar tendon which connects the bottom edge of the patella to the front of the shinbone (tibia).

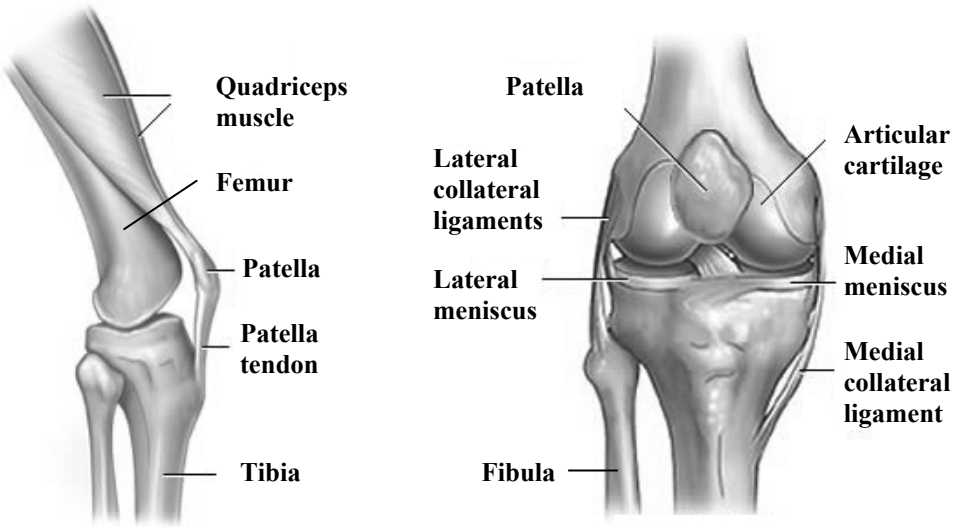

Figure 2-1 Knee anatomy

2.1.3 Ligament

The stability of the knee joint is achieved by a clever system of ligaments, strong muscles, and by a strong but elastic joint capsule. There are four ligaments connecting the femur and tibia (Figure 2-2). On the sides of the joint lie the medial collateral ligament (MCL) and the lateral collateral ligament (LCL), which serve as stabilizers for the side-to-side stability of the joint. The MCL is a broader ligament that is actually made up of two ligament structures, the deep and superficial components. The LCL, on the other hand, is a distinct cord-like structure. In the front part of the centre of the joint is the anterior cruciate ligament (ACL). This ligament is a very important stabilizer of the femur on the tibia and serves to prevent the tibia from rotating and sliding forward during agility, jumping, and deceleration activities. Directly behind the ACL is its opposite, the posterior cruciate ligament (PCL). The PCL prevents the tibia from sliding to the rear.

The quadriceps muscles on the front of the thigh are connected to the top of the patella by the quadriceps tendon, which covers the patella and becomes the patellar tendon. The patellar tendon then attaches to the front of the tibia.

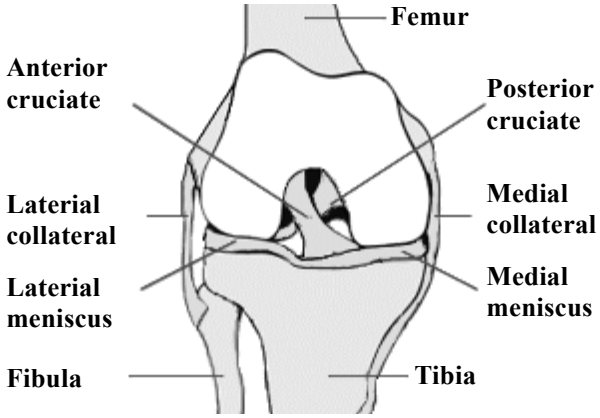

Figure 2-2 Knee ligaments

2.1.4 Mechanical axis

The mechanical axis is a static weight bearing axis which can be drawn on a radiographic image of the limb. The mechanical axis is defined in the frontal plane and the sagittal plane. The anatomical planes of the human body are defined in Figure 2-3, which has been adopted from website http://www.sci.port.ac.uk/rad/anatomy/. The mid-sagittal plane divides the body into right and left halves. Frontal (coronal) planes are drawn perpendicular to the sagittal lines and divide the body into anterior and posterior sections. Horizontal (transverse) planes divide the body into upper (superior) and lower (inferior) sections.

The mechanical axis of the lower limb in the frontal plane is defined as a line drawn from the centre of the femoral head to the centre of the ankle joint. In the sagittal plane, the normal mechanical axis runs from the centre of gravity to the centre of the ankle joint. This line is practically perpendicular to the ground. It therefore runs just behind the femoral head and just in front the knee (Figure 2-4). Figure 2-4 was adopted from website http://www.iol.ie/~rcsiorth/journal/volume2/issue5/figure1.jpg.

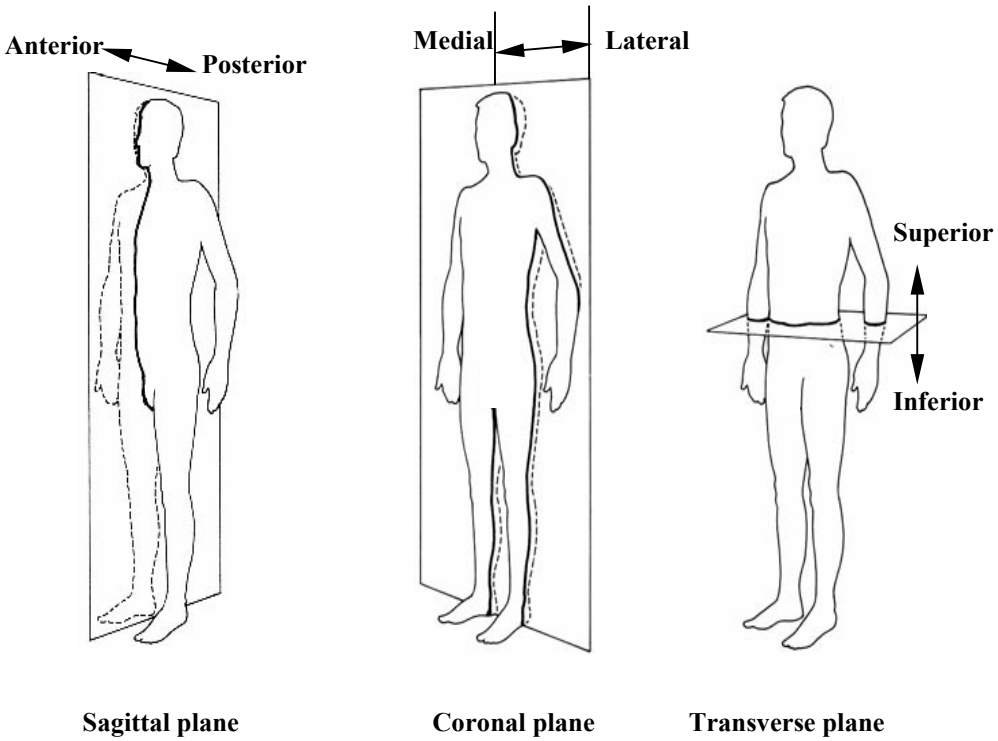

Figure 2-3 Anatomical planes of the human body

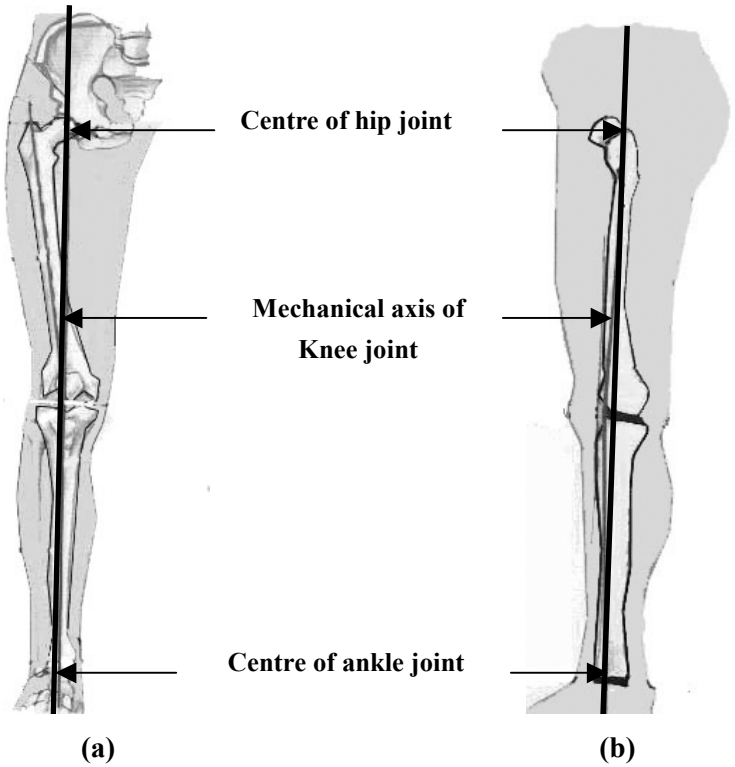

Figure 2-4 Mechanical axis of the knee joint: (a) mechanical axis in frontal plane; (b) mechanical axis in sagittal plane

2.1.5 Malalignment of knee joint

Deformity in the limb may occur in any plane, not just the anatomical sagittal or frontal planes. The common situation is for deformity to occur between these anatomical planes. In other words, angular deformity or malalignment may occur in any direction; medial or lateral, anterior and posterior or anywhere in between. Furthermore rotational deformity (internal or external) and translational deformity may coexist.

In a healthy, well-aligned knee joint, the mechanical axis passes through the middle of the knee in the frontal plane. In condition of abnormal alignment, the mechanical axis does not pass through the centre of the knee joint. The tibia adducted with respect to the femur is defined as varus malalignment; the tibia abducted with respect to the femur is defined as valgus malalignment in Figure 2-5, which is adopted and sketched from website http://moon.ouhsc.edu/dthompso/NAMICS/valgus.htm.

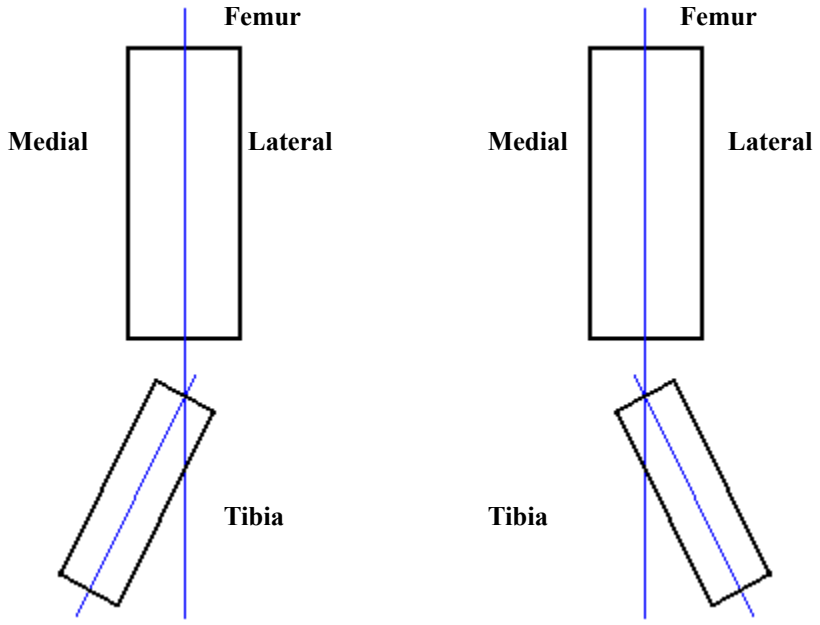

Figure 2-5 Varus (left) and valgus (right) malalignment

In many knee joint diseases, the mechanical axis is disturbed and does not pass through the centre of the joint. This disturbance results in overload of distinct areas of the knee joint leading to damage. The patella does not lie symmetrically

in its groove. The surgeon must restore the mechanical axis of the knee joint during the total knee replacement surgery, i.e. the new knee joint must be put in such a position that the mechanical axis passes through the middle of the new knee joint. It is called 'realigning of the total knee joint'. In this 'realigned' position, the patella once again glides symmetrically in its groove. A total knee prosthesis put in a badly aligned knee joint will be overloaded; the patella (or its prosthesis) will dislocate and eventually the whole total knee joint will loosen or break down.

2.2 Motion of knee

2.2.1 Freedom of knee joint

The knee joint is not a pure hinge joint but moves with a complex set of translations and rotations. It is a bicondylar, modified-hinge joint that exhibits 6 degrees of motion during dynamic activities. These 6 degrees of motion may be characterized as 3 rotations (flexion and extension, internal and external rotation, adduction and abduction rotation in Figure 2-6) and 3 translations (anterior and posterior translation, medial and lateral translation, compression and distraction, in Figure 2-6).

Flexion/extension (F/E) — rolling of the femur over the tibia; flexion is bending of the knee joint and extension is straightening of the knee joint

Anterior/posterior (AP) translation — back and forth sliding of the tibia

Internal/external (IE) rotation — rotation of the tibia about its long axis

Adduction/abduction rotation — rotation of the tibia in the frontal plane

Medial/Lateral (ML) translation — side to side sliding of the tibia

Superior/Inferior translation — movement of the femur and tibia along their own long axes

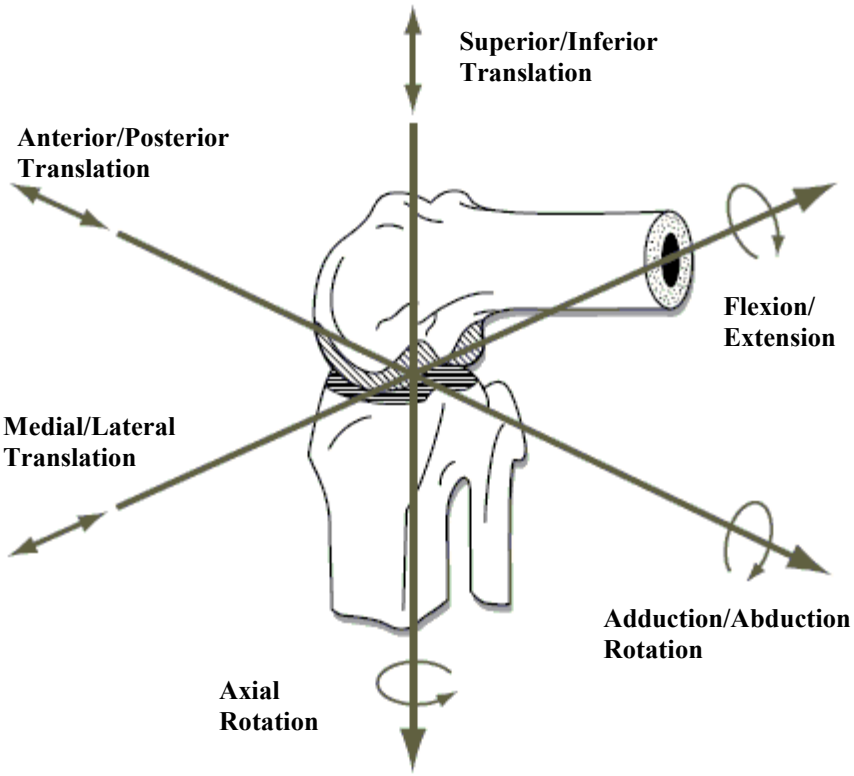

Figure 2-6 Knee motion

The three largest and most recognized movements of the knee are F/E, AP translation, and tibia IE rotation (Figure 2-6).

2.2.2 Range of motion

During routine knee flexion, tibio-femoral motion is a combination of sliding and rolling between the contacting tibia and femoral condoyle surfaces. Motion between the femur and the tibia is constrained by the geometry of the bony structures of the knee joint, the menisci and the muscular attachments via tendons and ligaments. The arc of motion of the knee defined by Hoppenfeld (1976) is typically about 0° extension to 135° of flexion. The amount of internal and external rotation about the knee is approximately 5° to 10° in each direction. It is in extension that the rotational component of the knee joint is necessary. The knee is unable to reach full extension without a small amount of external rotation of the tibia on the femur. This need for external rotation is due to the fact that the medial femoral condyle is approximately 1/2-inch longer than the

lateral femoral condyle. The external rotation of the tibia allows the knee to achieve full extension. This mechanism is known as the 'screw home' mechanism; it allows the knee to be held in full extension without undue fatigue of the surrounding musculature.

2.2.3 Normal gait cycle

Gait is the way locomotion is achieved using human limbs. Walking is the most common human gait. Gait characteristics are influenced by the shape, position and function of neuromuscular and musculoskeletal structures as well as by the ligamentous and capsular constraints of the joints.

Determining the accurate motions of the knee throughout one walking cycle has been the difficult goal of many researchers. Errors often arise in complex theoretical modelling or from skin and soft-tissue movement in experimental studies. LaFortune *et al.* (1992) reported the motions of the knee during one complete walking cycle. To avoid soft-tissue error during this study, traction pins were inserted directly into the femur and tibia of five subjects. Lafortune's results have often been referenced and compared with simulator studies (DesJardins *et al.* 2000, Walker *et al.* 1997).

The gait cycle is defined as the period from heel contact of one foot to the next heel contact of the same foot. This cycle is broken into two parts, stance and swing phase. On average, the gait cycle is about one second in duration with 60% in stance and 40% in swing. The stance phase is further divided into an initial double stance, followed by a period of single stance and then a final period of double stance. Double stance indicates that both feet are in contact with the ground; single stance is the period when only one foot is in contact with the ground. The walking gait cycle is illustrated in Figure 2-7, which has been adopted and redrawn from website http://www.gla.ac.uk/ibls/fab/tutorial/anatomy/hfgait.html. During the early part of the stance phase, the heel strikes the ground, progressing to foot-flat during single stance and then to the forefoot contact during the final double stance phase, ending with toe off.

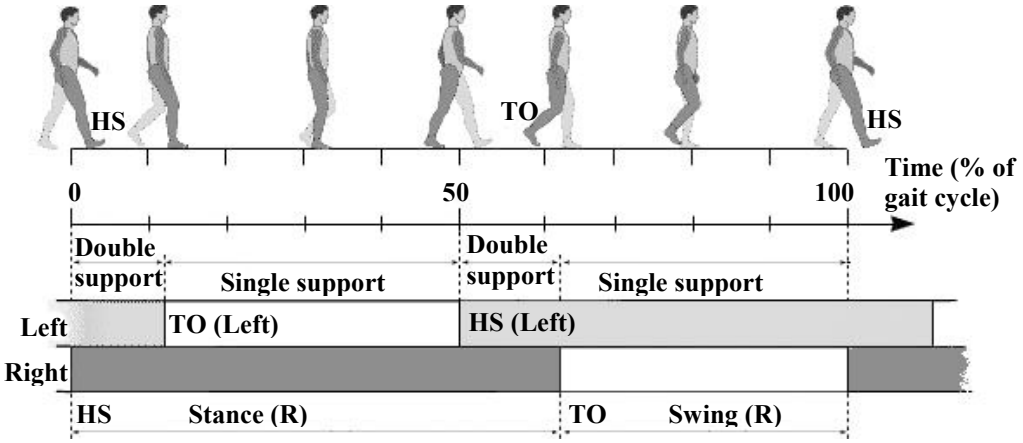

Figure 2-7 A walking gait cycle (HS stands for heel strike, TO stands for toe off)

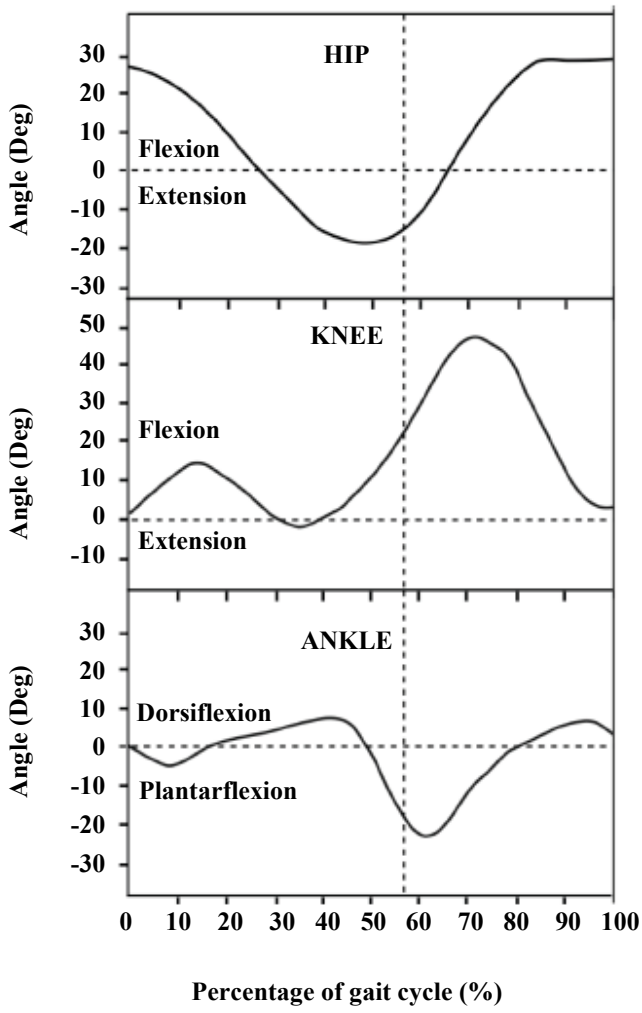

Figure 2-8 Joint angles during a walking gait cycle

Figure 2-8 illustrates joint angles during a walking gait cycle. At the hip, there is a single peak of flexion and extension in each cycle. Figure 2-8 is adopted from

website http://medicalsciences.med.unsw.edu.au/SOMSWeb.nsf/resources/ANAT314105/$file/FA2-21_WALKING2+biomech.pdf. The hip extends during the stance phase, and then starts to flex at about heel strike for the other leg, continuing flexion through the swing phase. The range of hip flexion/extension increases with strike length; the increase is mainly in flexion; the hip will not extend more than about 30 degrees. At the knee, there are two peaks of flexion: a small one in the stance phase and a larger peak that allows the foot to clear the ground. The flexion in stance phase increases with walking speed. The flexion in the swing phase is followed by an extension that ends just before heel strike.

2.3 Forces in knee joint

2.3.1 Forces in knee joint

The determination of in-vivo forces acting at the human knee and in-vivo torques acting across the tibio-femoral joint are of great value to clinicians, researchers and implant designers.

The two main techniques which have been used to determine in-vivo loading are telemetry, which is a direct experimental approach, and mathematical modelling, which predicts in-vivo contact loads on the basis of a theoretical evaluation.

The forces acting in the knee during activity were calculated in the late 1960s using a knee model with the input of gait analysis and force-plate data, together with geometrical measurements of the limb (Morrison 1970). The highest forces were obtained for descending stairs or a slope and then ascending, and the lowest for level walking. The more vigorous the activity, the higher the forces, as shown for active subjects walking downhill where forces of 8 body-weight (BW) were obtained (Kuster *et al.* 1997). In one study, a telemeterized distal femoral replacement was used to measure the forces directly, the first such measurements of its kind in the knee (Taylor *et al.* 1998). In walking activities, where the flexion angles in stance are about 20°, the patello-femoral forces are less than 2 BW, but, in higher flexion, forces as high as 7 BW have been

calculated. From several studies, the shear forces were determined to be higher in a direction that would tense the posterior cruciate ligament. In the telemetry study, the forces that would tense the anterior cruciate ligament in walking were found to be small. There are significant axial torques occurring during walking and other activities. The torques act at the foot as a consequence of the twisting of the body as it swings over the planted foot. The direction of the torque is internal, such that the lateral tibial plateau tends to move anteriorly. In walking, Taylor *et al.* (1998) measured the torque at around 8 Nm.

2.3.2 Typical pattern of knee contact force during walking gait cycle

Paul did one of the earliest studies on the knee joint forces in 1965 (Paul 1967). His resulting joint force curve still remains one of the standard loading configurations for many knee simulators. Morrison (1970) followed this lead with a similar curve to Paul's, with only slight differences due to different grouping of muscle forces and moments in his model. Their studies of gait cycle demonstrate a force pattern with three cyclic peaks occurring during stance phase. Figure 2-9 shows three peaks of the typical pattern of knee contact force during stance phase of level walking. The pattern was derived from studies reported by Schipplein and Andriacchi (1991).

The gait cycle can be described in the phasic terms of initial contact (IC), loading response (LR), mid-stance (MSt), terminal stance (TSt), pre-swing (PSw), initial swing (ISw), mid-swing (MSw) and terminal swing (TSw). The stance period consists of the first five phases: initial contact, loading response, mid-stance, terminal stance and pre-swing. The swing period is primarily divided into three phases: initial swing, mid-swing and terminal swing. Pre-swing, however, prepares the limb for swing advancement and in that sense could be considered a component of the swing phase.

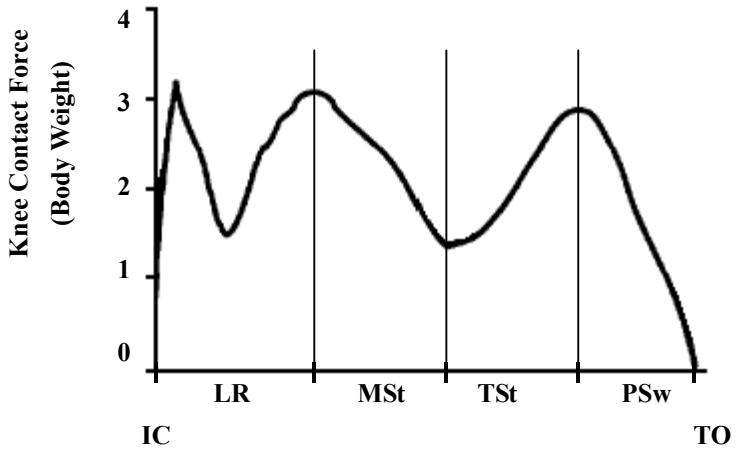

Figure 2-9 The typical pattern of knee contact force during level walking can identify with precision all five phases of gait occurring during stance (Schipplein *et al.* 1991)

Initial contact is an instantaneous point in time only and occurs the instant the foot of the leading lower limb touches the ground. Most of the motor function that occurs during initial contact is in preparation for the loading response phase that will follow.

The loading response phase occupies about 10% of the gait cycle and constitutes the period of initial double-limb support. During loading response, the foot comes in full contact with the floor and body weight is fully transferred onto the stance limb. The ascending initial peak of the vertical force graph reveals the period of loading response (see Figure 2-9).

Mid-stance represents the first half of single support, which occurs from the 10% to 30% periods of the gait cycle. It begins when the contralateral foot leaves the ground and continues as the body weight travels along the length of the foot until it is aligned over the forefoot. The descending initial peak of the vertical force graph reveals the period of mid stance (see Figure 2-9).

Terminal stance constitutes the second half of single-limb support. It begins with heel rise and ends when the contralateral foot contacts the ground. Terminal stance occurs from the 30% to 50% periods of the gait cycle. During this phase, body weight moves ahead of the forefoot. The ascending second

peak of the vertical force graph demonstrates the period of terminal stance (see Figure 2-9).

Pre-swing is the terminal double-limb support period and it occupies the last 12 percent of the stance phase, from 50% to 62% of the gait cycle. It begins when the contralateral foot contacts the ground and ends with ipsilateral toe off. During this period, the stance limb is unloaded and body weight is transferred onto the contralateral limb. The descending portion of the second peak of the vertical force graph demonstrates the period of pre-swing (see Figure 2-9).

The initial one-third of the swing period, from 62% to 75% of the gait cycle, is spent in initial swing. It begins the moment the foot leaves the ground and continues until maximum knee flexion occurs, when the swinging extremity is directly under the body and directly opposite the stance limb.

Mid-swing occurs in the second third of the swing period, from 75% to 85% of the gait cycle. Critical events include continued limb advancement and foot clearance. This phase begins following maximum knee flexion and ends when the tibia is in a vertical position.

Terminal swing is the final phase of the swing period from 85% to 100% of the gait cycle. The tibia passes beyond perpendicular, and the knee fully extends in preparation for heel contact.

2.4 Structure and mechanical properties of bone

2.4.1 Bone structure

Bone is an anisotropic, heterogeneous and viscoelastic material. It provides support for the body against gravity, serves as a lever system for muscles, and protects internal organs. Depending on shape, bone can be divided into three groups: long, short, and flat. In the leg and foot, only long and short bones are present.

At the macroscopic level, there are two major forms of bone tissue: cortical and cancellous/trabecular. The structure of bone is shown in Figure 2-10. Cortical bone is a compact and stiff material while cancellous/trabecular bone is a porous structure. Cortical bone is usually found in diaphyseal regions of long bearing bones, where it has a hollow cylinder shape. The external surface, generally smooth, is called the periosteum and the internal surface is called the endosteum. Cancellous bone is found in epiphyseal and metaphyseal regions of long bones, where it is continuous with the inner surface of cortical bone. The pores of cancellous bone are filled with marrow.

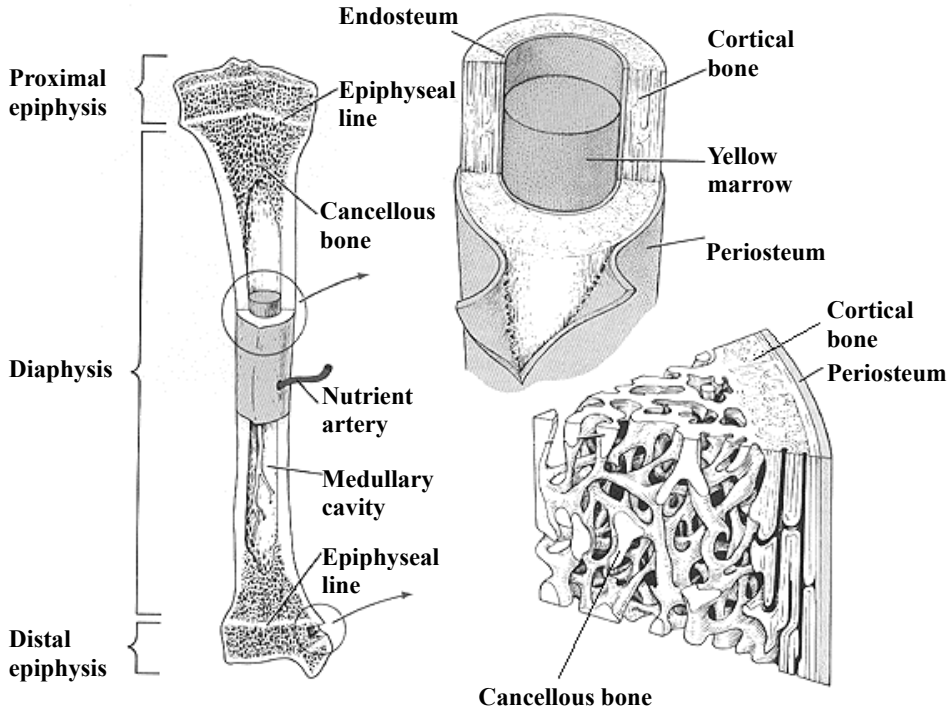

Figure 2-10 Bone structure (Galik 2002)

Cortical bone is a dense material with a maximal density of about 1.8 g/cm^3. The density of cancellous bone varies from 0.05 to 0.7 g/cm^3, (Terrier 1999).

2.4.2 Mechanical properties of bone

The mechanical properties of bone are primarily related to the presence of the mineral phase that permeates the organic matrix. The stress-strain law of cortical and trabecular bone is very sensitive to the porosity of bone and to the alignment

of the microstructures. Since the mineral content and the microstructure alignment are distributed in a very inhomogeneous way, bones have a complex inhomogeneous and anisotropic mechanical behaviour.

The viscoelastic behaviour of bone can be neglected when the applied loads are maintained below one Hz, as occurs in most common activities such as walking, running, etc. Therefore, in most situations bone can be considered as an inhomogeneous and anisotropic elastic material.

The major difference between cortical and trabecular bone is the difference in relative densities, which has a profound influence on the elastic modulus. Mechanical tests show that the elastic modulus is related to the relative density by a power law function with an exponent ranging between two and three. Although these relationships were initially derived from compression tests, tensile tests indicate that the elastic modulus of bone is approximately the same in compression and in tension. The elastic modulus of cortical bone depends on its porosity and that of trabecular bone depends on its degree of mineralization.

In general, cortical and trabecular bone are anisotropic. For cortical bone, this anisotropy is caused by the alignment of the osteons along the longitudinal axis of long bones. The longitudinal elastic modulus is about 50% greater than the transverse elastic modulus. The shear modulus and the Poisson ratio are also different in the longitudinal and transverse directions. For trabecular bone, the anisotropy is caused by the alignment pattern of the trabeculae.

Although cortical and trabecular bone are fully anisotropic, transverse isotropy is a good compromise between model complexity and validity. Indeed, for many bones, including long load-bearing bones, there is clearly a privileged direction, where the stiffness value is about twice the value of the other equivalent directions (Cowin and Hegedus, 1976).

The study of static mechanical properties of human cortical bone by Reilly and Burstein (1975) has been used as a reference in many papers. The experiments

were carried out on femoral diaphyseal cortical bone. The mechanical properties are listed in Table 2-1.

Table 2-1 Mechanical properties of femoral cortical bone from experiments by Reilly and Burstein (1975)

Mechanical property	**Longitudial**	**Transverse**
Young's modulus (MPa)	17,000	11,500
Ultimate tensile strength (MPa)	133	51
Ultimate compressive strength (MPa)	193	133
Ultimate strain	3.1%	0.7%

It has been demonstrated that the post-yield behaviour of cancellous bone is asymmetric, with different behaviour in tension and compression (Ford 1996, Fyhrie 2000, Keaveny 1994, Kopperdahl 1998, Linde 1992, Morgan 2001). In tension, cancellous bone fails in an almost brittle manner with little post-yield resistance against load. In compression, cancellous bone fails with pronounced strain softening and crushing. The mechanical properties of cancellous bone are shown in Table 2-2. In summary, the mechanical properties of cancellous bone show:

- The same tensile and compressive Young's moduli
- Asymmetric yield strengths, strongly dependent on density
- Asymmetric yield strains with no dependency on density and loading direction
- Asymmetric post-yield behaviour with brittle fracture in tension and strain softening in compression

Table 2-2 Mechanical properties of cancellous bone

Reference	Bone	Minimum principal strain (%)	Maximum principal strain (%)	Young's Modulus (Pa)
Compression				
-Keaveny (1994)	Bovine tibia	1.08	1.86	2380
-Morgan (2001)	Human tibia	0.73	N/A	1091
-Morgan (2001)	Great. Trochanter	0.70	N/A	622
-Morgan (2001)	Human Vertebra	0.77	N/A	344
-Morgan (2001)	Femoral neck	0.83	N/A	3230
-Fyhrie (2000)	Human Vertebra	0.67	1.5	500
-Kopperdahl (1998)	Human Vertebra	0.81	1.45	219
-Linde (1992)	Knee	N/A	2.0	408
Tension				
-Keaveny (1994)	Bovine tibia	0.78	1.37	2630
-Morgan (2001)	Human tibia	0.65	N/A	1068
-Morgan(2001)	Great. Trochanter	0.61	N/A	597
-Morgan (2001)	Human Vertebra	0.70	N/A	349
-Kopperdahl (1998)	Human Vertebra	0.78	1.59	301
Shear				
Ford (1996)	Bovine tibia	1.35	4.24	349

2.4.3 Bone remodelling

2.4.3.1 Theory of bone remodelling

Bone remodelling is a continuous process for which resorption and densification are usually balanced. Bone remodelling takes place mainly in conditions of changed mechanical loading. In artificial joint replacement, the orthopaedic prostheses, which are directly in contact with bones, alter enormously the stress distribution within the bones and induce therefore a functional adaptation of the bone tissue. In a total knee replacement, this bone reaction lasts several years and can lead to failure or permanent bone loss for revision.

Research regarding the relationship between mechanical environment and bone structure, Wolff suggested an important hypothesis that bone grows wherever it is needed and resorbs where it is not needed (Wolff, 1986). That is to say, bone growth, resorption and reconstruction are all relative to its mechanical environment. People usually call this Wolff's Law. Early classical studies based on the hypothesis of Wolff's Law showed the general scheme for remodelling, which was studied qualitatively but not quantitatively. One of the first fundamental theories of bone remodelling, which was proposed by Cowin and Hegedus (1976), was based on general continuum mechanics principles. In the 1980s, several attempts to quantify the bone remodelling process so as to investigate and predict the structure and remodelling behaviour of bone were reported in the literature. An approach to predict bone adaptation was proposed by Fyhrie and Carter (1986). In this case, they postulated that bone was a self-optimising material, adapting its orientation and density in response to its stress/strain state. Huiskes *et al.* (1987, 1989) and Weinans *et al.* (1992) described bone remodelling characteristic mathematically. They used the fixed, actual shape of the structure that was to be studied as the initial shape to predict the optimal structure inside. Their results were similar to the actual structures. They used the apparent density as the characterization of the internal morphology and the strain energy density (SED) as the stimulus.

Hurwitz *et al.* (1998) examined the relationship between the predicted loads at the knee and the distribution of bone between the medial and lateral sides of the tibia. The relationship between the knee adduction moment during gait and the ratio or distribution of medial to lateral tibial bone mineral content was studied. The sensitivity of the bone distribution in the proximal tibia to the expected dynamic load distribution in this study was very consistent with findings from other studies that examined the relationship between the tibial bone distribution and static factors likely to alter loading conditions at the knee (Akamatsu *et al.* 1997). Li and Nilsson (2001) investigated the relationship between changes in bone mineral density in the proximal tibia and fixation of the tibial component during 2 years postoperative and concluded that the early migration seems to be

related more to local activities at the interface rather than to changes in bone mineral density (BMD) assessed below the interface. The changes in BMD during 2 years reflect the bone remodelling caused by the normalization of alignment after operation and are not related to the implant fixation.

2.4.3.2 Simulation model for internal bone remodelling

Bone adapts to mechanical loads by internal or external bone remodelling. Internal remodelling can be expressed as a change of porosity. External remodelling can be expressed as a refinement of geometry.

In their femur FE model, van Rietbergen *et al.* (1993) used adaptive bone remodelling simulation theory based on a site-specific formulation, whereby it was assumed that the bone in the treated femur attempts to normalize its stress-strain patterns locally to the same value as in the untreated one, under the same loading conditions. The theory proposes that bone mass is regulated by the elastic strain energy per unit of mass, which is called the remodelling signal *S*. *S* can be determined from the strain-energy density $u = \frac{1}{2}\boldsymbol{\varepsilon} \bullet \boldsymbol{\sigma}$ (with $\boldsymbol{\varepsilon}$ the strain tensor and $\boldsymbol{\sigma}$ the stress tensor) and the apparent density ρ, it is expressed as

$$S = \frac{u}{\rho} \tag{2-1}$$

According to the site-specific formulation, the local bone in the operated femur strives to equalize its actual remodelling signal S to the corresponding local value S_{ref} in the non-operated one for the same external loads, by removing or adding bone. Hence, if the rate of net bone-mass turnover equals $\frac{dM}{dt}$, then

$$\frac{dM}{dt} \sim S - S_{ref} \tag{2-2}$$

The theory further assumes a threshold level for the remodelling response. Hence, when $|S\text{-}S_{ref}|$ is smaller than the threshold value, no remodelling response occurs. The remodelling objective can, thus, be formulated by

$$(1-s)S_{ref} \le S \le (1+s)S_{ref} \quad \textbf{(2-3)}$$

with s a constant. The region between $(1\text{-}s)S_{ref}$ and $(1+s)S_{ref}$ represents the nonreponsive area, or 'dead zone'.

The adaptive process in the operated bone can then be expressed in terms of the rate of net bone turnover:

$$\begin{aligned} \frac{dM}{dt} &= \tau A(\rho)\left[S-(1-s)S_{ref}\right], && if \quad S \le (1-s)S_{ref} \\ \frac{dM}{dt} &= 0, && if \quad (1-s)S_{ref} < S < (1+s)S_{ref} \\ \frac{dM}{dt} &= \tau A(\rho)\left[S-(1+s)S_{ref}\right], && if \quad S \ge (1+s)S_{ref} \end{aligned} \quad \textbf{(2-4)}$$

Figure 2-11 demonstrates the curve of bone adaptive process.

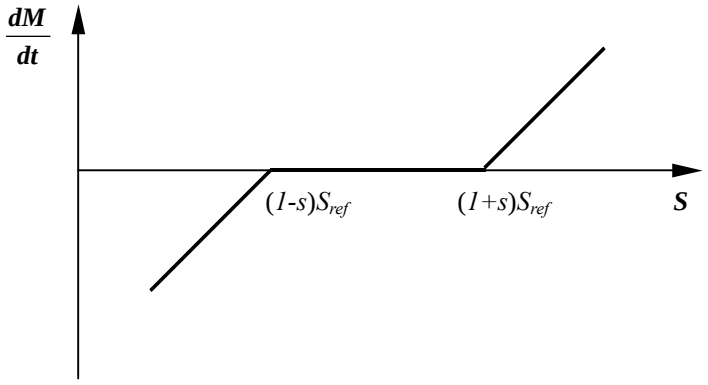

Figure 2-11 The bone adaptive process demonstrates the rate of net bone turnover $\frac{dM}{dt}$ as function of bone remodelling signal *S*

The rate of net bone turnover $\frac{dM}{dt}$ was expressed as the rate of change of the external geometry $\frac{dx}{dt}$(external bone remodelling):

$$\frac{dM}{dt} = \rho A \frac{dx}{dt} \quad \textbf{(2-5)}$$

with A the external surface area at which the rate of mass change $\frac{dM}{dt}$ took place and x a characteristic surface coordinate, perpendicular to the periosteal surface. For the adaptation of the internal bone mass due to porosity changes, they used

$$\frac{dM}{dt} = V\frac{d\rho}{dt} \quad \textbf{(2-6)}$$

with V the volume in which the bone mass change takes place and $\frac{d\rho}{dt}$ the rate of change in apparent density.

Hazelwood *et al.* (2001) developed a constitutive model for bone remodelling which includes a number of relevant mechanical and biological processes. The model simulated porosity and material property changes brought about by internal bone remodelling provoked by disuse and damage (Figure 2-12). Nyman *et al.* (2004) used this model to simulate the bone adaptation in long stemmed total knee arthroplasty.

This constitutive model was fundamentally based on two non-linear differential equations.

$$\dot{p} = Q_R N_R - Q_F N_F \quad \textbf{(2-7)}$$

$$\dot{D} = \dot{D}_F - \dot{D}_R \quad \textbf{(2-8)}$$

In equation (2-7), the rate of change of porosity, $\dot{p}$, was assumed to be a function of the mean bone resorbing (Q_R) and refilling (Q_F) rates for each basic multicellular unit (BMU), and the density of resorbing (N_R) and refilling (N_F) BMUs/area.

In equation (2-8), Damage (D) is defined here as total crack length per section area of bone, $\dot{D}_F$ and $\dot{D}_R$ represent the fatigue damage formation and removal rates respectively.

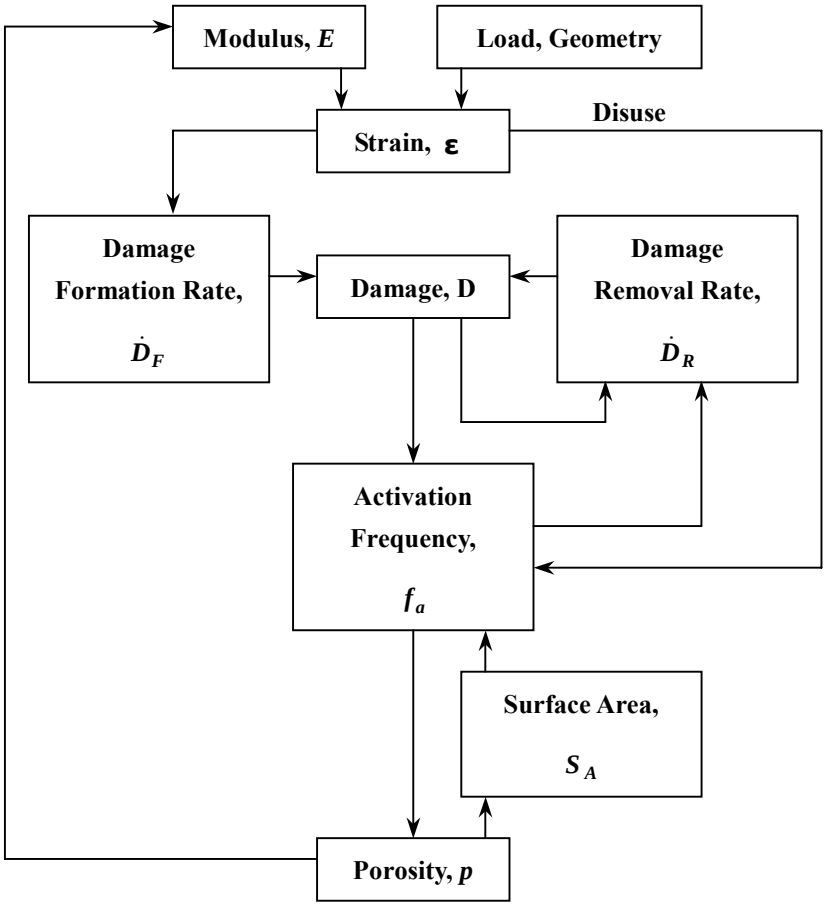

Figure 2-12 Schematic representation of the bone remodelling algorithm (Hazelwood *et al.* 2001)

2.4.3.3 Simulation model for external bone remodelling

Zhu *et al.* (2001) created an external bone adaptation model and used it to simulate the process of bone remodelling in total hip replacement. In this model, strain energy was the stimulus to control bone external remodelling.

$$\frac{dn}{dt} = C(n,P)[u(P) - u_0(P)] \qquad u = \frac{1}{2}\varepsilon \cdot \sigma; \quad u_0 = \frac{1}{2}\varepsilon_0 \cdot \sigma_0 \qquad \textbf{(2-9)}$$

In equation (2-9), $\frac{dn}{dt}$ is the remodelling rate at point *P* in the normal direction and *C(n,P)* is the coefficient of external remodelling.

Chapter 3

Introduction to total knee replacement

3.1 Common causes of knee pain and loss of knee function

The common causes of knee pain and loss of knee function in clinic are osteoarthritis, rheumatoid arthritis and post traumatic arthritis.

Osteoarthritis usually occurs after the age of 50 and often in an individual with a family history of arthritis. The cartilage that cushions the bones of the knee softens and wears away. The bones then rub against one another causing knee pain and stiffness.

Rheumatoid arthritis is a disease in which the synovial membrane becomes thickened and inflamed, producing too much synovial fluid, which over-fills the joint space. This chronic inflammation can damage the cartilage and eventually cause cartilage loss, pain and stiffness. Rheumatoid arthritis can follow a serious knee injury.

A knee fracture or severe tears of the knee's ligaments may damage the articular cartilage over time, causing knee pain and limiting knee function.

If the knee joint is severely damaged by arthritis or injury, it may be hard to perform simple activities such as walking or climbing stairs. The patient may begin to feel pain while sitting or lying down.

If medication, changing activity level and using walking supports are no longer helpful, total knee replacement surgery will be considered. By resurfacing damaged and worn surfaces of the affected knee joint, total knee replacement surgery can relieve knee pain, correct leg deformity and allow the patient to resume normal activities.

One of the most important orthopaedic surgical advances of this century, knee replacement was first performed in 1968 (ANON. 2001). Improvements in

surgical materials and techniques since then have greatly increased its effectiveness.

3.2 Types of knee replacement

A set of knee-prosthesis components consists of: an anatomically shaped distal femoral element, normally made of a cobalt-based alloy; a proximal tibial element that is normally made of ultra high molecular weight polyethylene (UHMWPE); and an optional patellar insert, typically made of titanium. Implantation of prosthesis typically requires removal of the anterior cruciate ligament and, depending on the prosthesis design, may also involve removal of the posterior cruciate ligament. The medial collateral ligament and lateral collateral ligament are critical in holding the joint in place and producing joint motion.

3.2.1 Unicompartmental knee replacement and total knee replacement

Sometimes osteoarthritis only affects one side of the joint, and it may be better to replace just this side. This is called a unicompartmental knee replacement. It involves replacing just one side of the knee joint, usually the inner (medial) part, leaving the undamaged part of the joint alone. However, if there is a risk that the arthritis may become more generalised in the joint, the surgeon may decide to perform a total rather than a unicompartmental replacement. Total knee replacement replaces the whole joint surfaces of the femur, tibia and patella (Figure 3-1). Figure 3-1 to Figure 3-3 were adopted from website http://www.totaljoints.info/TOTAL_KNEE_MAIN.htm.

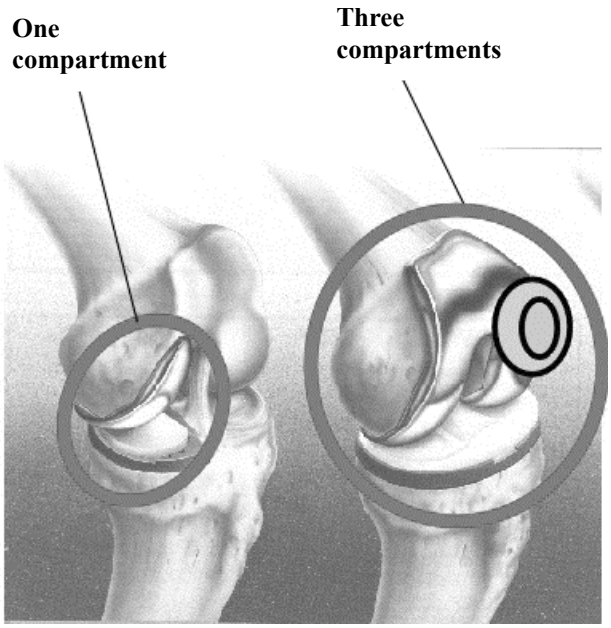

Figure 3-1 Unicompartmental knee replacement and total knee replacement

3.2.2 PCL retaining total knee replacement and posterior stabilized total knee replacement

The posterior cruciate ligament (PCL) is an important structure that stabilizes the knee joint. With some knee replacements, the posterior cruciate ligament is defective and removed, and with others it is left intact. The anterior cruciate ligament is usually removed for a total knee replacement, and left in place for a unicompartmental replacement.

After removal of the PCL, a special total knee prosthesis that simulates the function of the PCL should be implanted. The stabilization of the total knee joint in these prostheses is achieved by a ‘cam and post’ mechanism added to the prosthesis components. This mechanism replaces the function of the PCL (Figure 3-2).

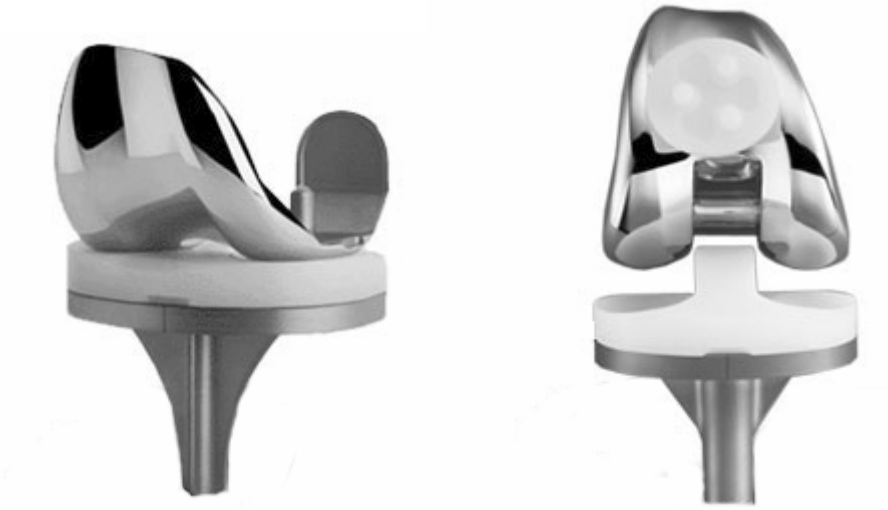

Figure 3-2 PCL retaining (left) and posterior stabilized total knee prosthesis (right)

3.2.3 Cemented and cementless (uncemented) total knee replacement

Knee prostheses can be cemented to the bone with polymethylmethacrylate (PMMA). PMMA is a polymer that is mixed at the time of implantation. An alternative to cementing is to rely on initial fixation of the components to bone. This can occur with 'press fitting' the implant onto the bone or with screws. The cementless implants have a roughened or porous surface at the bone/implant interface. During healing, bone grows into the porous surface of the implant and locks the components in place. Cementing the implants is the more common form of fixation due to its predictability.

There is another option called hybrid TKR with an uncemented femoral component and cemented tibial and patellar components.

3.2.4 Fixed- and mobile-bearing total knee replacement

Current TKR devices can be subdivided into two groups based on different fundamental design principles: fixed-bearing knees, in which the UHMWPE insert is snapped or press fitted into the tibial tray, and mobile-bearing designs which facilitate movement of the insert relative to the tray. In mobile-bearing knees, motion of the knee is designed to occur at two articulating surfaces. Such

designs differ according to the kinematics at the tray-insert interface and resulting axis of rotation of the knee. Some mobile-bearing designs allow both anterior-posterior translation and internal-external rotation at the tray-insert counter face, hence reducing the degree of rotation at the femoral-insert articulation. The polyethylene cushion may be part of the platform (fixed) or separate (mobile). In a mobile-bearing knee replacement, both the metallic femoral component and metallic tibial tray move across a polyethylene insert to create a dual-surface articulation (Figure 3-3).

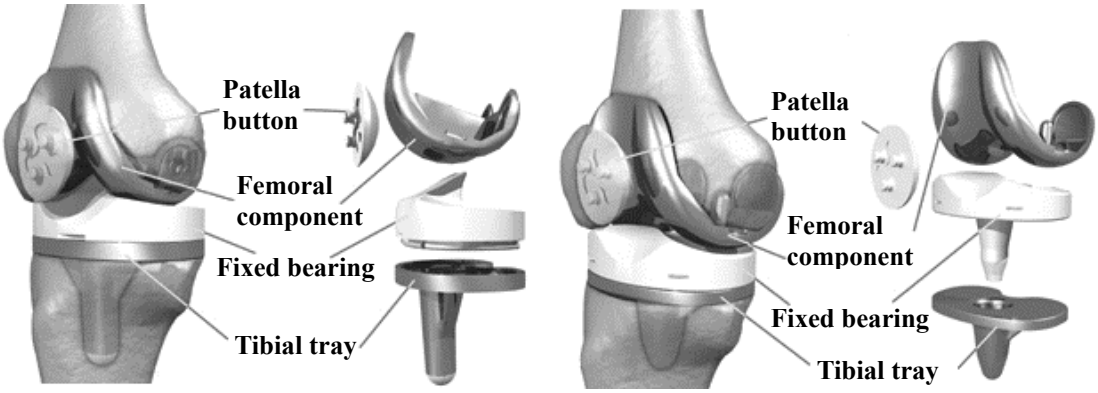

Figure 3-3 Fixed-bearing (left) and mobile-bearing (right) total knee prosthesis

3.3 Components of total knee prostheses

There are three primary components in total knee implants. These include the femoral, tibial and patellar components (Figure 3-3).

The femoral component is typically made of a metal called Cobalt-Chrome alloy (CoCr). CoCr is a very hard and durable material, allowing it to withstand the massive loads and cycles a knee endures on a daily basis. The other advantage of this metal is its ability to wear a highly polished surface that is durable. Other materials, such as Titanium alloy cannot hold a polish for a long period, as this metal is too soft and can become scuffed.

The tibial component is usually made up of two main pieces, the tibial tray and the tibial bearing component. The tibial tray is typically made of Titanium or Cobalt-Chrome. There are arguments for and against each of these materials and

as of now, probably either material is good. The tibial bearing component is the bearing between the femoral and tibial components. The bearing is made of a plastic called ultra high molecular weight polyethylene (UHMWPE) and is fixed to or allowed to rotate in the tibial tray. There are many different configurations of the tibial component depending on the manufacturer and the surgeon's preference. The insert can come already attached to the tray or can come separate and be placed on the tray at the time of surgery. Some tibial components are all polyethylene.

The patellar (knee cap) component is also made of plastic (UHMWPE). In the past, metal backed patellar implants were used; however, the majority of patellar components are all polyethylene.

3.4 Geometry of total knee prosthesis

The geometry of knee prostheses will influence the kinematics of the knee joint after TKR operation (Walker and Sathasivam 2000). The location of the knee joint contact point, which is decided by the geometry of the knee prostheses, directly affects the lever arm of the quadriceps, which determines the force that needs to be generated for a given external moment.

To explain the geometry and function of condylar TKR, a parametric description of geometry of conventional condylar replacement was defined in Figure 3-4, (Walker and Sathasivam 2000). In Figure 3-4: ROF, represents outer radius, femoral; RIF, inner radius, femoral; ROT, outer radius, tibial; RIT, inner radius, tibial; BS, bearing spacing; RDF, radius at the distal part of the femur; RPF, radius in the posterior part of the femur; RPSF, radius at the posterior-superior part of the femur; PDTA, posterior-distal transition angle, where the large distal-anterior radius RDF meets the smaller distal-posterior radius RPF; RPT, posterior radius, tibial; RAT, anterior radius, tibial. The two frontal geometries shown have very different mechanical functions. In Fregly's model, the tibio-femoral surface geometry was described by five radii: RFF, frontal radius, femoral; RFT, frontal radius, tibial; RSDF, sagittal distal radius, femoral; RSPF,

sagittal posterior radius, femoral; RST, sagittal radius, tibia (Figure 3-5) (Fregly 1999).

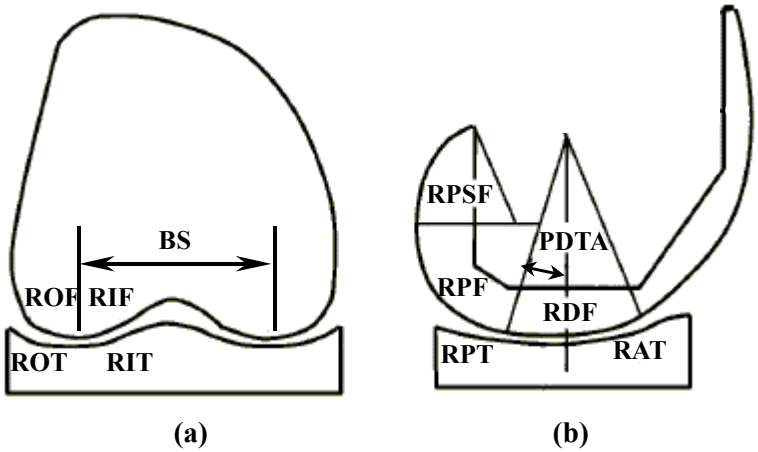

Figure 3-4 Definition of the geometry of condylar replacements in (a) the frontal plane and (b) the sagittal plane (Walker and Sathasivam 2000)

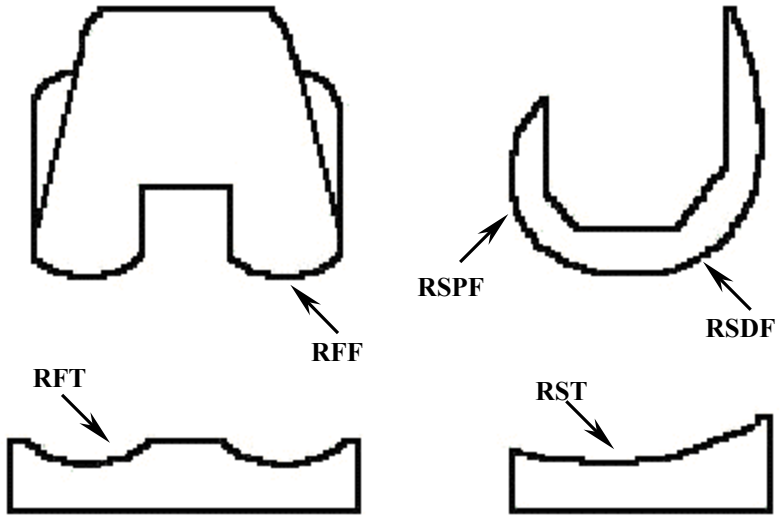

Figure 3-5 Schematic of geometry of knee implant in Fregly's model (Fregly 1999)

To simulate the patello-femoral joint, the femoral component has an anatomically shaped patellar groove. This accommodates a dome-shaped polyethylene patella assumed to replace half of the thickness of the natural patella.

3.5 Failure modes of total knee replacement

About 440,000 total knee replacements are carried out worldwide each year (Zihlmann *et al.* 2005). Because of adiposity and a higher life expectancy, the number of TKR implantations will increase in the future. Although the patient satisfaction rate is around 90% (D'Lima *et al.* 2001), the number of patients who need revision surgery is significant. Annually, 35,000 TKR are revised worldwide (Sharkey *et al.* 2002). The main reasons for TKR failure are: early wear of the UHMWPE, aseptic loosening, tibial femoral instability, patellar instability and fatigue failure of the tibial tray (Villa *et al.* 2004).

In a report of recently performed total knee revisions (Sharkey *et al.* 2002), more than 50% of them were performed within 2 years of primary surgery. The most common reason for revision was polyethylene wear (25%), followed by loosening (24%), instability (21%), and infection (17.5%).

3.5.1 UHMWPE wear

The bearing surface in knee replacements is made of UHMWPE. The early wear of the UHMWPE tibial bearing component is the main cause of TKR failure (Callaghan et al. 2004). UHMWPE debris particles from total knee replacement can produce osteolytic reactions leading to implant loosening and failure (Bei *et al.* 2004). Primary UHMWPE wear modes identified in TKR include pitting, delamination, and abrasion/adhesion (Harman *et al.* 2001, Muratoglu *et al.* 2003).

The pitting and delamination seen in UHMWPE tibial bearing component are due to fatigue loading, which causes cracks to propagate from surface or subsurface defects (Bartel *et al.* 1986). Pitting and delamination are influenced by the multiaxial stress state of the UHMWPE at and below the surface. Pitting is caused by cracks that start at the surface and propagate into the material, or by subsurface cracks that propagate toward the surface. Delamination is caused when subsurface cracks continue to propagate tangent to the surface. The combined stresses associated with these damage modes are the range of the

maximum principal stress acting tangent to the surface and the maximum shear stress that reaches its largest value approximately 1 mm beneath the articulating surface. The maximum shear stress is a measure of the distortion of the material, as is the von Mises stress which is used often as an alternative measure of distortion. In general, the range of maximum principal stress and the maximum shear stress (or von Mises stress) increase when the contact stress is increased (Bartel *et al.* 1995). The stresses associated with pitting and delamination on UHMWPE bearing surface are affected by the conformity of the articulating surfaces, by the thickness of the polyethylene component, and by the elastic modulus of the polyethylene (Petty *et al.* 1999).

Abrasive/adhesive (or mild) wear is influenced primarily by surface topography, contact loads and surface kinematics (Bei *et al.* 2004, Fregly *et al.* 2003, McEwen *et al.* 2005). Sliding distance is an important design factor of TKR to reduce mild wear of UHMWPE. For fixed-bearing TKR, kinematics is controlled by bearing surface geometry in both the frontal and sagittal planes. The most influential parameter is the sagittal radius of the tibial surface. Sagittal geometry affects both internal-external rotation and anterior-posterior displacement. In general, the less the constraint between the bearing surfaces, the greater the relative sliding and the greater the wear. In contrast to fixed-bearing TKR, kinematics in mobile-bearing TKR is controlled by the geometry of both the superior and inferior bearing surfaces. With the addition inferior bearing surface, mobile-bearing implant theoretically can increase conformity without transferring excessive stress to the implant-bone interface. It appears that wear can be reduced in mobile-bearing designs compared with fixed-bearing designs, primarily due to the larger contact areas. Another reason for less wear in mobile-bearing TKR is unidirectional motion. The rotating platform mobile-bearing design redistributes the motions between the femoral-insert and tray-insert articulating surfaces. Most of the rotation occurs at the tibial articulating surface of the UHMWPE insert, which is simply a unidirectional rotaion motion that is known to produce low wear (McEwen *et al.* 2005, Wang *et al.* 1996). Since the majority of the rotation occurs at the distal interface, the

proximal femoral articulating interface experiences very low rotation. Therefore, at the femoral-insert articulation the motion is also preferably unidirectional and similarly has a low wear rate. Hence, the unique design of the rotating platform mobile-bearing knee translates complex input motions into more unidirectional motions, thus benefiting from a reduced wear rate due to decreased cross shear on the molecularly oriented UHMWPE. However, the rotation of the knee with the fixed-bearing TKR occurs entirely at the femoral-insert articulation. The resulting multidirectional wear path at this interface increases the amount of cross shear on the polyethylene articulating surface and, therefore, produces a greater polymer wear rate when subjected to higher rotation kinematic inputs.

The early wear of UHMWPE is related to the extension of contact areas and to the magnitude of contact pressure. Additionally, the contact pressure and areas depend on the degree of conformity and operative techniques including mechanical alignment and fixation of the components (Argenson and O'Connor 1992, Plante-Bordeneuve and Freeman 1993, Wasielewski *et al.* 1994, Wright and Bartel 1986). Wear can also lead to malalignment or instability of the joint and can initiate fracture of the tibial component (Walker *et al*. 2000a).

3.5.2 Aseptic loosening

A prosthetic knee component can loosen from the bone due to relative motion between the component and the bone. Aseptic loosening of the tibial component has remained one major cause of failure after TKR (Windsor *et al.* 1989). Aseptic loosening of prosthetic components may eventually lead to pain, instability and loss of function, and thus constitutes a failure. The limb alignment and the shape of the articulating surface (constrained or not) influence strongly the local magnitude and the eccentricity of the tibial bone-implant interface pressure and have large effects on the distribution and amount of relative micro motions. Loosening of a cemented tibial component and failed ingrowth of an uncemented knee arthroplasty along with loosening from osteolysis usually result from varus malalignment (Vince 2003).

On the other hand, long-term remodelling of bone tissue surrounding the tibial component is controlled by mechanical stress, which is affected by the load transmission from implant to bone. The bone density of the proximal tibia beneath the tibial component decreased by a rate of up to 5% per year (Levitz *et al.* 1995). This large decrease of bone density should not be neglected if long-term fixation of the prosthesis is considered.

Both femoral component loosening and tibial component loosening will cause TKR failure (Figure 3-6 to Figure 3-8). Fehring and McAvoy (1996) described lateral fluoroscopic interface views of painful uncemented femoral components that showed loosening in a way that is often not apparent on plain films (Figure 3-6).

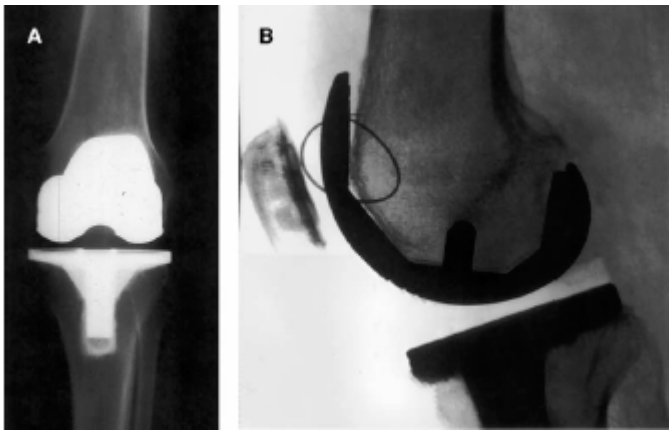

Figure 3-6 (A) Anterior-posterior radiograph of a patient with a painful knee arthroplasty in apparently good alignment. (B) Lateral fluoroscopic view of an uncemented femoral component of a painful knee arthroplasty (Fehring and McAvoy 1996).

Figure 3-7 Lateral radiograph of a hybrid knee arthroplasty 2 years after surgery with failure of ingrowth of the femoral cementless implant, bone loss also appear on tibia (Callaghan *et al.* 2004).

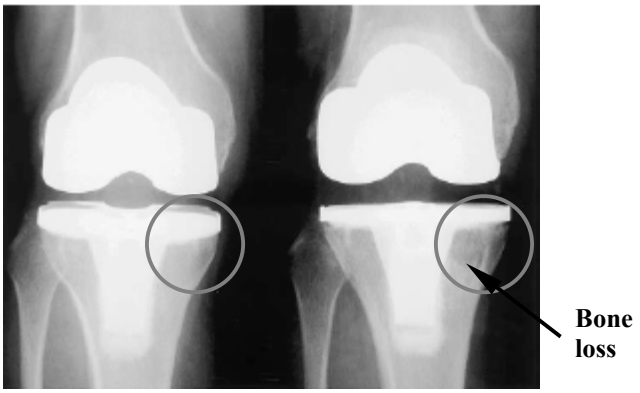

Figure 3-8 Radiographs immediately after a primary knee arthroplasty and at 4 years after surgery show the bone loss in the medial tibial plateau that was not present initially or at the 1-year follow-up (Callaghan *et al.* 2004).

3.5.2.1 Migration and loosening of femoral component after TKR

Inadequate bone stock is often found in revision surgery of femoral components of TKR. Bone loss in the distal femur can lead to loosening of the component (Soininvaara *et al.* 2004). In Chockalingam and Scott's research (2000), a survival analysis and radiological review were performed on a series of femoral TKR with prosthesis cemented or cementless, press-fit. The incidence of loosening of the femoral component at 6 years was 9.8 % with cementless

fixation and 0.6% with cemented. Walker *et al.* (2000b) measured the quantitative changes in bone mineral density (BMD) in the distal femur after cemented total knee arthroplasty in osteoarthritic knee joints. An average decrease in bone density of 17.1% was measured adjacent to the prosthesis at the 12-month follow-up. Bone loss was most rapid during the first 3 months after TKR. Spittlehouse *et al.* (1999) reported the greatest BMD decrease (16%) in the distal anterior femur over the first 6-month postoperative period in 16 patients with uncemented knee prostheses. They assumed that these reductions in BMD, which were most significant during the early postoperative phase, might be related to postoperative stress shielding. In the research of Nillson *et al.* (1995), the magnitude of migration did not differ between cemented and uncemented fixation in 2 years.

3.5.2.2 Migration and loosening of tibial component after TKR

Aseptic loosening of the tibial prosthesis component in TKR continues to be a primary concern for clinicians and patients. The radiographic and functional status of 101 tibial component of cementless TKR in 101 patients were evaluated 3, 12, and 24 months after implantation by Fuiko *et al.* (2003). Wedge-shaped radiolucent areas appeared at the tibia interface, which showed that the forces of displacement postoperatively overcame initial mechanical stability. The shape was determined 3 months postoperatively. Ryd *et al.* (1995) showed 1.9 mm migration for cementless and 0.8 mm migration for cemented tibial implants in the first year postoperatively. Hilding *et al* confirmed this subsidence. Perillo-Marcone *et al.* (2004) found that patients with press-fit implants had high risk of failure and were found to migrate the most. Patients with cemented implants were found to have low risk of failure and these implants migrated the least. Tissakht *et al.* (1995) evaluated relative displacements between the host bone and the tibial component of total knee implants. The results of the study showed that use of screws for immediate post-surgical fixation is likely to result in enhanced bone ingrowth. The research of Li and Nilsson (2000) found that most of the tibial component migration occurred within the first months and thereafter the implants seemed to stabilize

in knees with uncemented fixation. In the uncemented implants, there was a significant relationship between average BMD and migration. In knees with cemented fixation, subsidence was initially small but continuously increasing. The preoperative bone quality of the proximal tibia influences the magnitude and pattern of the migration of the uncemented tibial components. Fixation with bone-cement compensates for the variation in bone quality; however, the effect seems to diminish with time. Walker *et al.* (2000b) compared cemented and two types of uncemented tibial component fixation, the axial migrations were significantly less for cemented and HA-coating, compared with press-fit, at all time intervals.

3.5.3 Catastrophic failure of tibial tray

The tibial tray between polyethylene and bone was introduced to improve the distribution of forces between the implant and the bone and lower the incidence of failure attributable to loosening, subsidence, and polyethylene deformation (Chatterji *et al.* 2005). Fracture of the metal tibial tray after TKR is rare (Altintas *et al.* 1999). But once significant loss of sub-baseplate bone has occurred, the baseplate is at risk of fracture. In aseptic loosening, the interface between implant/cement and bone is overloaded, compressed, resorbed or remodelled so that the implant subsides, tilts and/or rotates. The position of the implant eventually becomes overtly changed, which can be seen on regular radiographs when it is more than 2-3 millimetres. Catastrophic failures of the tibial tray due to fatigue fracture have been reported in patients in consequence of loss of bony support through bone remodelling or osteolysis, severe varus or valgus deformities or as a result of stress shielding in response to a prosthesis implant (Abernethy *et al.* 1996, Altintas *et al.* 1999, Chen and Krackow 1994, Maruyama *et al.* 1994).

3.5.4 Conclusion from TKR failure literature review

Total knee replacement has become a very effective method to relieve pain in the knee joint; however, the failure of TKR has been widely reported. The most

common reasons for TKR revision are polyethylene wear and aseptic loosening. The generation of UHMWPE wear particles and the resulting osteolysis is a cause of long-term loosening of TKR joint. Malalignment is the main cause of both polyethylene wear and prosthesis loosening. However, failure of polyethylene and prosthesis loosening lead to further malalignment and thus instability in the joint. Because of the change of stress status postoperatively, bone remodelling after TKR is also an important factor causing malalignment and loosening. It is therefore important to conduct analysis of total knee replacement to address these issues.

Chapter 4

Finite element analysis of total knee replacement during gait cycle

4.1 Introduction

Wear of UHMWPE in total knee replacements remains a major limitation to the longevity of these clinically successful devices (Villa *et al.* 2004). Many factors leading to failure of the bearing surface of total knee prostheses have been reported including the material properties of polyethylene, the balance of the soft tissues, tibial insert thickness and patient body mass via its effect on joint loads; other factors include the patient's daily activity and the stress distribution on the contact surface (Bei *et al.* 2004, Liau *et al.* 1999).

The dominant UHMWPE wear modes in total knee implant are pitting and delamination (Bartel *et al.* 1995). The combined stresses associated with these damage modes are the range of the maximum principal stress acting tangent to the surface and the maximum shear stress that reaches its largest value approximately 1 mm beneath the articulating surface. The maximum shear stress is a measure of the distortion of the material. The range of the maximum principal stress and the maximum shear stress increase when the contact stress on UHMWPE surface is increased. Knowledge of contact pressures and areas in total knee replacements are considered a reliable tool to predict the potential wear of UHMWPE (Sathasivam *et al.* 2001). Bartel *et al.* (1991) demonstrated that more severe damage in total knee tibial components was associated with the higher contact stress on the tibial bearing component. The evaluation of contact areas and pressures in total knee replacement is a key issue to prevent early failure. The contact pressure and areas are dependent on the degree of conformity and operative techniques including mechanical alignment and fixation of the components (Argenson and O'Connor 1992, Plante-Bordeneuve and Freeman 1993, Wasielewski *et al*. 1994, Wright and Bartel 1986).

Using a finite element method, this chapter compares contact stresses and contact areas in fixed- and mobile-bearing implant with three types of malalignment at three stages of the gait cycle. It is very important to understand the effects of these conditions on the implant components and to compare the performance of fixed- and mobile-bearing implants.

4.1.1 FE analysis of failure of polyethylene

The human knee joint is a complex system of articulating bony structures that undergo large loads and large relative displacements during various activities of daily living. Finite element model studies have long been recognized and trusted as reliable complementary tools in the analysis of human articulations. An advantage of such numerical studies lies in the precise control of loading, motion, boundary conditions and structural alterations in parametric studies of joint response. Moreover, the ligament forces, contact forces/areas and cartilage stresses are invaluable output results of such model studies. Finite element methods have been widely adopted in investigation of TKR failure.

Villa *et al.* (2004) studied the contact stresses of UHMWPE inserts of mobile-bearing knee prostheses by means of FEM and experimental tests. Essner *et al.* (2003) considered the effect of tibial sagittal radius on wear. It was found that decreasing the sagittal conformity of a given TKR design gives a reduction in rotational stiffness and a trend toward lower wear associated with rotation. Rawlinson and Bartel (2002) analysed stress conditions of three contemporary tibial configurations using FEM with non-linear material properties. Taylor and Barrett (2003) analysed the influence of eccentric loading on the stress on the tibial articulating surface component by comparing the FEA results. Using dynamic method, Fregly *et al.* (2005) predicted contact pressure during gait cycle and calculated wear area and volumes of UHMWPE in a fixed-bearing total knee replacement. Knight et al. (2007) developed an adaptively remeshing model of TKR wear and compared it with an experimental knee wear simulator. In finite element analysis of TKR failure, most models include a femoral component, a tibia bearing component and a tibial tray. The femoral component

was modelled as a rigid body, and the tibial components were modelled as elastic material (Liau *et al.* 2002, Villa *et al.* 2004). Because the wear of UHMWPE has been agreed as the most important reason of TKR failure, the non-linear property of UHMWPE should be taken into account in FE analysis. Recently, UHMWPE has been modelled as a non-linear material (Otto *et al.* 2001, Rawlinson and Bartel 2002).

The model can only be complete when finite element analysis of a total knee replacement takes soft tissues into account. Godest *et al.* (2002) used springs in their model to simulate the action of the soft tissues of the knee. Moglo *et al*. (2003) used non-linear spring elements to model various ligaments.

4.1.2 FE analysis of TKR in conditions of malalignment

As stated before, malalignment is an important issue in TKR failure. Liau *et al.* (2002) compared the stresses of three kinds of prostheses (high conformity flat-on-flat, high conformity curve-on-curve and medium conformity flat-on-flat) subjected to different kinds of malalignment. The greatest increase of contact stress and von Mises stress occurred in the high conformity flat-on-flat design of knee prosthesis under the severest malalignment condition. Yang and Lin (2001) studied a new kind of rotating hinge with a spherical contact surface and mentioned the importance of this kind of design to malalignment. Perillo-Marcone *et al.* (2000) demonstrated that valgus orientation of the prosthesis reduces the risk of cancellous bone failure. Using explicit finite element model, Perillo-Marcone and Taylor (2007) reported investigation on the variations produced in bone strain distribution in the proximal tibia when the axial load is applied eccentrically.

4.1.3 FE analysis of TKR during gait cycle

Finite element method was used to estimate the stress distribution in implants during a gait cycle. Ishikawa *et al.* (1996) developed a two-dimensional finite element model to evaluate the effect of contact kinematics on polyethylene stresses during a gait cycle. The relative positions of the TKR components

during a gait cycle were determined from in vivo fluoroscopy data. Static FE analyses were performed to evaluate the pressure distribution on the polyethylene surface at various points during the gait cycle. Estupinan *et al.* (1998) used an idealised two-dimensional model of a non-conforming knee joint replacement to simulate the influence of cyclic loading on the polyethylene stresses. In the model of Estupinan *et al.* (1998), a 200 N load was applied to the femoral indenter, which was then displaced 4 mm across the polyethylene surface, the load was removed and the indenter returned to its original position. Reeves *et al*. (1998) used a two-dimensional sagittal plane model to examine the development of plastic strains in the polyethylene due to repetitive loading. The anterior-posterior motion of the femoral component was controlled by applying a displacement history adopted from the literature. Godest *et al.* (2002) used an explicit finite element approach to simulate the kinematics and the internal stresses in knee implants during a gait cycle. However, few papers have discussed the stress distribution in implants and bones during a gait cycle considering malalignment which comes from surgery or malalignment which has not been totally corrected. In the condition of malalignment, the total knee prosthesis will bear uneven loads and the maximum stress will be increased.

According to literature review, alignment is an important consideration in total knee replacement (TKR). Significant changes in the axial alignment of the femur and tibia will influence the loading distribution in the knee joint. These changes can also alter the stress distribution in the implant and sometimes result in TKR failure. The tibial component in total knee prostheses can be either a fixed- or a mobile-bearing. The long-term clinical performance of mobile-bearings has not been proved to be better than that of fixed-bearings (Woolson and Northrop, 2004). However, Cheng *et al.* (2003) investigated the effect of surgical maltranslation and malrotation on contact pressures of fixed- and mobile-bearing knee prostheses and concluded that the mobile-bearing design can reduce maximum contact pressure more significantly than the fixed-bearing design when malalignment conditions of the tibio-femoral joint occurred. These investigations (Cheng *et al.* 2003, Villa *et al.* 2004, Werner *et al.* 2005)

measured experimentally the contact pressure on the contact surfaces of the TKR; however, the stress distribution inside the prosthesis has not been analysed and neither has the stress in the tibial tray. Moreover, the effect of different flexion angles during the gait cycle has not been addressed. In order to clearly understand the biomechanical performance during gait cycle and malalignment, this chapter compares the stress distribution in the fixed- and mobile-bearing knee implants for both normal alignment and surgical malalignment at different flexion angles using a finite element method.

This study is based on the hypothesis that the pattern of contact stress at the tibial insert of knee prostheses at different stages of the gait cycle could be an indicator of the wear performance of knee prostheses. The knowledge of contact pressures and areas in total knee replacements are considered a reliable tool for predicting the potential wear of a PE insert (Sathasivam *et al.*, 2001).

4.2 Modelling method of TKR

4.2.1 Knee simulator

A knee simulator is used for evaluation of the performance of total knee replacements. The knee simulation machine designed by Walker *et al.* (1997) is commonly used (Figure 4.1). In the simulation machine, the femoral component can rotate about a transverse axis through the femur. Varus-valgus rotation is defined about an axis perpendicular to the transverse axis. Anterior-posterior displacement is motion of the tibial component along this perpendicular axis. Internal-external rotation is about the long axis of the tibia.

Regarding the forces and moments, the axial force, applied in line with the tibial axis, is the largest force with an immediate sharp peak in the stance phase followed by two shallower maxima, each of approximately 2-4 times body weight (Morrison, 1970). The anterior-posterior force and the internal-external torque significantly affect the sliding and rotation patterns between the joint surfaces and need to be controlled as inputs.

Table 4-1 shows how the various motions and forces were constrained in the design of the simulator.

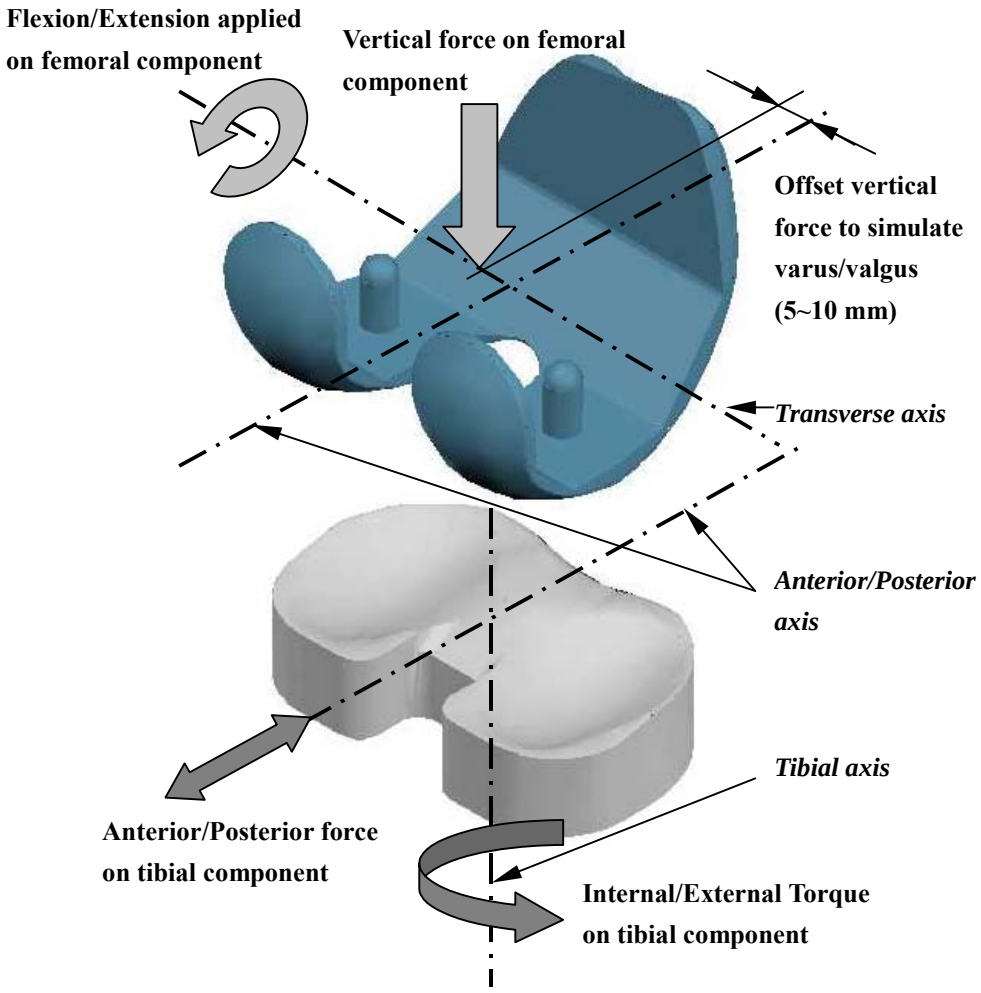

Figure 4-1 The mechanical arrangement for the knee simulation machine (Walker *et al.* 1997)

Table 4-1 The treatment of displacements, rotations, forces and moments in the knee simulation machine (Walker *et al.* 1997)

Mode	Femoral component	Tibial component
Displacements and rotations		
Axial	Unconstrained	Fixed
Anterior-posterior	Fixed	Restrained by springs
Medial-lateral	Fixed	Unconstrained
Flexion-extension	Controlled	Fixed
Varus-valgus	Unconstrained	Fixed
Internal-external	Fixed	Restrained by springs
Forces and moments		
Axial	Controlled	—
Anterior-posterior	—	Controlled
Medial-lateral	—	—
Flexion-extension	Applied	—
Varus-valgus	Controlled by offset axial force	—
Internal-external	—	Controlled

4.2.2 Malalignment

Separation or lift-off of femoral components has been observed and this has the potential to be extremely damaging to the polyethylene insert (Stiehl *et al.* 1997). Stiehl *et al.* (1997) reported that 90% of the patients examined had significant lift-off of the medial or lateral condyle at some stage during the gait cycle. The maximum medial lift-off was approximately 2 mm and the maximum lateral lift-off was approximately 3.5 mm. Lift-off of the lateral condyle results from varus malalignment and will distribute more contact force on the medial condyle.

In this chapter, tibial components were tilted to simulate varus malalignment. To evaluate the extent of varus by tilting tibial components 5°, the following models were developed in MSC/ADAMS.

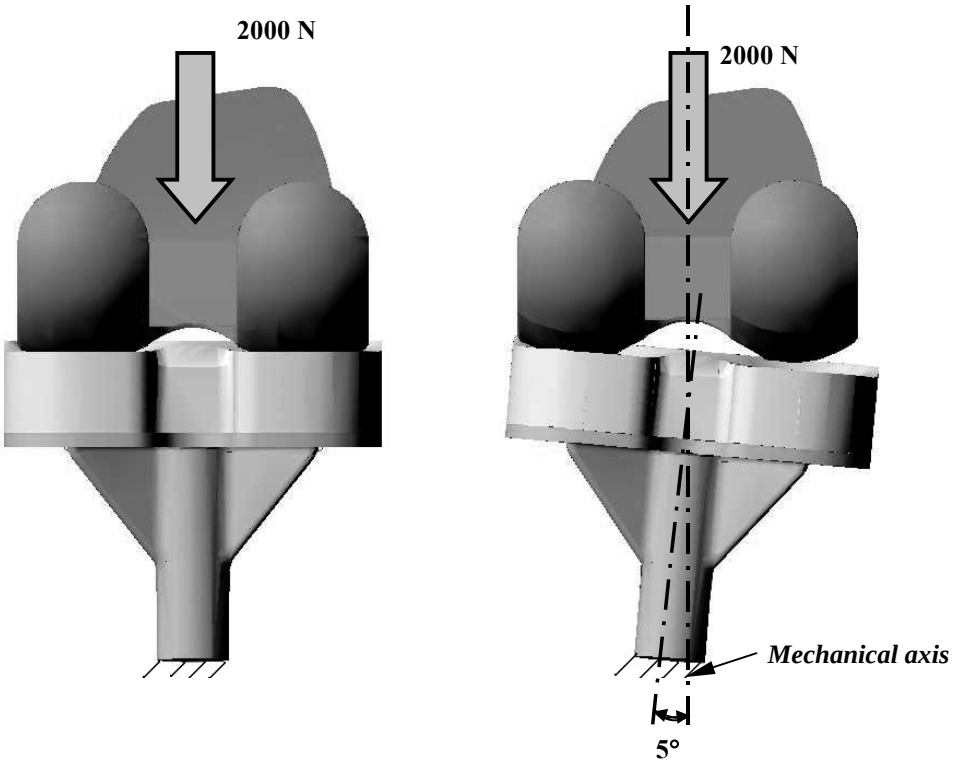

Figure 4-2 MSC/ADAMS model of knee components contact in condition of normal alignment (left) and varus malalignment (right)

In Figure 4.2, the tibial components were tilted 5° to simulate varus malalignment. In the condition of normal alignment and varus, the tibial component was fixed to the ground; the anterior-posterior translation, medial-lateral translation and internal-external rotation of femoral component were fixed. The femoral component had freedom in axial translation, varus-valgus rotation and flexion-extension rotation. A 2000 N vertical force was applied to the femoral component. Both sides of the condyle then come into contact with the application of the vertical force. In condition of varus, the calculated contact force at the medial and lateral sides were 1067 N and 933 N respectively. The varus malalignment simulated by tilting the tibial bearing component resulted in a ratio of 53.4 to 46.6 for the medial-lateral load distribution, which changed from an even load distribution in the normal alignment.

4.3 FE analysis of TKR at different stages of gait cycle

4.3.1 Method

Finite element (FE) models of fixed- and mobile-bearing knee implants were developed in ANSYS as shown in Figure 4-3 (Shi *et al.* 2005). The material for the femoral component, tibial bearing component and tibial tray are cobalt-chrome alloy, UHMWPE and titanium alloy respectively. The Young's modulus for cobalt-chrome alloy and titanium alloy is 193,000 MPa and 110,000 MPa respectively. The Poisson ratio for cobalt-chrome alloy and titanium alloy is 0.29 and 0.33 respectively (Galik 2002). The tibial bearing component with UHMWPE is modelled as a linear material (Young's modulus of 1016 MPa, and Poisson ratio of 0.46) and non-linear material (Figure 4-4) respectively. The coefficient of friction between the femoral component and tibial bearing component, and the tibial bearing component and tibial tray (in a mobile-bearing implant) is 0.04 (Galik 2002, Taylor and Barret 2003).

The tibial bearing components were 10 mm thick and had an articular surface with a sagittal radius of 40 mm and a coronal radius of 22 mm. The tibial trays were 3 mm thick. The femoral component had a distal sagittal articular radius of 35 mm, a posterior sagittal radius of 22 mm, and a coronal radius of 20 mm.

With these models, three different stages of the gait cycle (15°, 45°, 60° flexion) were simulated (Figure 4-5). At each load stage, the tibial tray was fixed to the ground and a vertical axial load was applied at the femoral component. The vertical loads were 2200 N, 3200 N and 2800 N at 15°, 45° and 60° flexion respectively as shown in Figure 4-6 (Villa *et al.* 2004). The condition of normal alignment, 5° varus, 3° malrotation and 2 mm maltranslation were simulated in each load stage respectively (Figure 4-7 and Figure 4-8). The stress distributions in the fixed- and mobile-bearing implants were compared under all conditions of alignment.

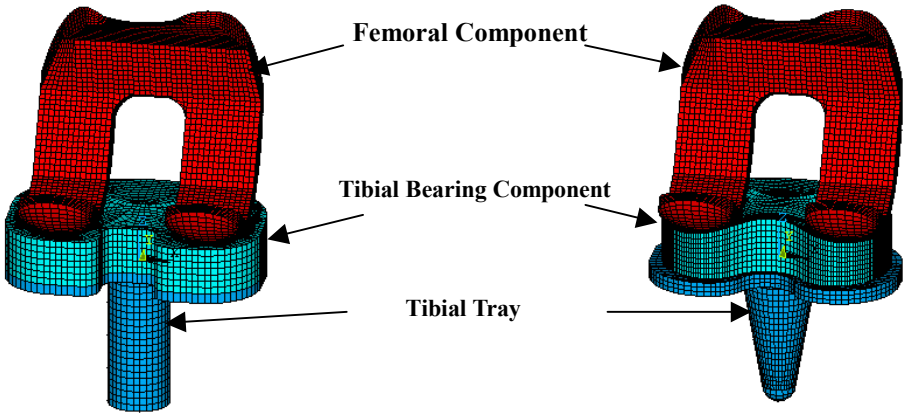

Figure 4-3 FE models of fixed-bearing implant (left) and mobile-bearing implant (right)

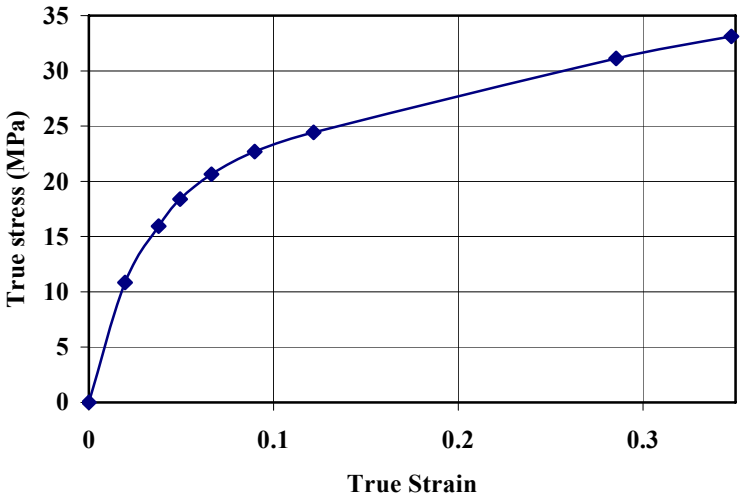

Figure 4-4 Non-linear true stress-true strain for UHMWPE material model (Taylor and Barret 2003)

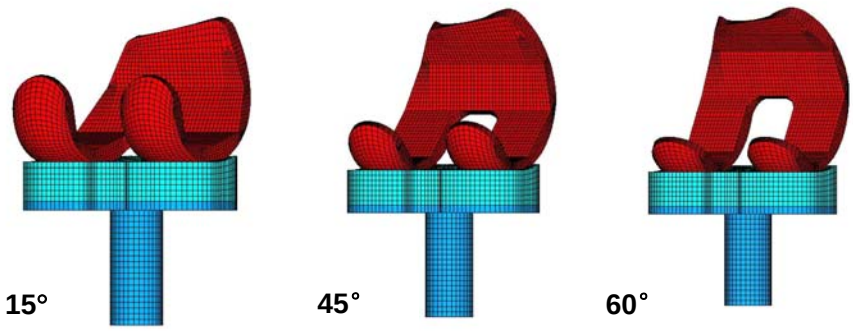

Figure 4-5 Model of different stages of gait

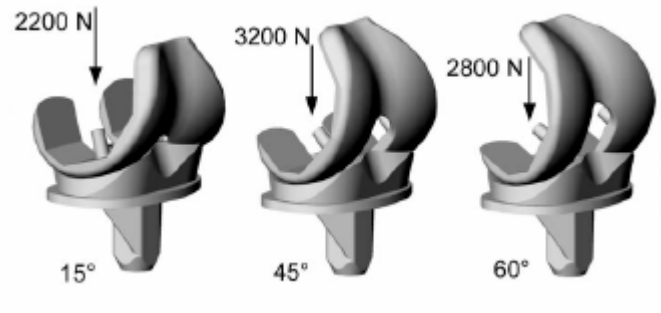

Figure 4-6 Different stages of gait cycle load (Villa *et al.* 2004)

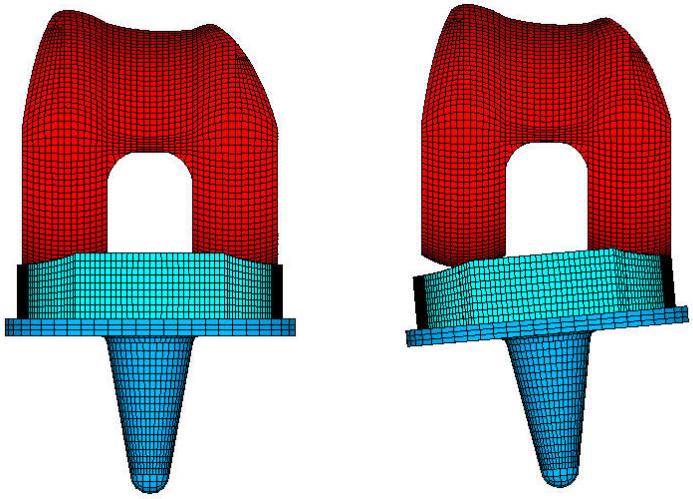

Figure 4-7 Normal alignment (left) and 5° varus (right)

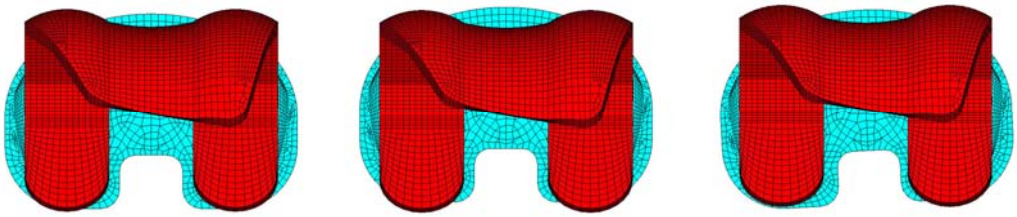

Figure 4-8 Normal alignment (left), 2 mm maltranslation (middle) and 3° malrotation (right)

4.3.2 Solution techniques

4.3.2.1 Application of load

As all components of the knee prosthesis were modelled as deformable bodies, load could not be applied on a control node of the femoral component. An extra rigid body was created which bonded with the femoral component (Figure 4-9).

The gait cycle loads were applied on a line of this rigid body. This line went through the centre of the sagittal articular axis of the femoral component.

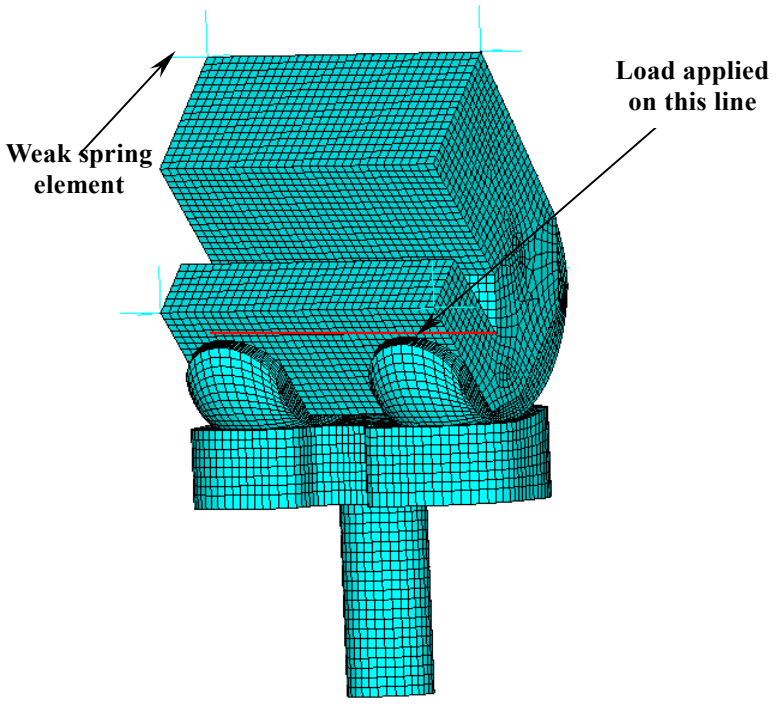

Figure 4-9 Application of load on knee prosthesis

4.3.2.2 Solution convergence

Contact problems are highly non-linear and require significant computer resources to solve. In addition, UHMWPE is a non-linear material in this research. In this non-linear structure, convergence problem were overcome using the following approaches.

- Control load steps. The maximum number of substeps was set to 1000 and automatic time stepping was also switched on. This ensured that all of the modes and behaviours of interest would be accurately included. ANSYS increases the time step size automatically.

- Use weak spring element to provide initial stability. A number of spring elements were used to fix the body in space (Figure 4.7). This technique

artificially restrained the system during intermediate load steps in order to prevent unrealistically large displacements from being calculated. By connecting the springs to nodes in space, the reactions at these nodes were negligible compared to the contact reaction force.

- The element size of all the models was 2 mm. Mesh sensitivity was studied; further mesh refinement changed the predicted peak contact pressure by less than 5%.

4.4 Results

Through finite element models of fixed- and mobile-bearing implant, stress distributions in tibial bearing components were simulated for different conditions of alignment.

Table 4-2 Comparison of maximum contact pressure when UHMWPE was modelled as linear and non-linear material

			2200 N at 15° flexion		3200 N at 45° flexion		2800 N at 60° flexion	
			Maximum contact pressure (MPa)	Contact areas (mm^2)	Maximum contact pressure (MPa)	Contact areas (mm^2)	Maximum contact pressure (MPa)	Contact areas (mm^2)
Linear	Mobile-bearing implant	Superior surface	20.1	197.4	29.4	163.9	39.6	131.2
		Inferior surface	6.1	1032.5	8.7	1008.1	8.04	964.5
	Fixed-bearing implant		20.5	207.9	32.5	223.4	39.1	152.6
Non-linear	Mobile-bearing implant	Superior surface	18.2	653.4	19.4	306.5	23.9	237.5
		Inferior surface	2.8	1477	4.3	1455.2	3.9	1430
	Fixed-bearing implant		16.3	676.0	17.0	507.8	23.2	249.5

The maximum contact pressures and von Mises stress obtained in the tibial bearing component with the linear UHMWPE model were much higher than

those obtained with the non-linear UHMWPE material (Table 4-2 and Table 4-3). For a fixed-bearing implant, the maximum tibio-femoral contact pressures were 16.3 MPa, 17.0 MPa and 23.2 MPa using the non-linear models at 15°, 45° and 60° flexion respectively; the values obtained using the linear models were 10%, 52% and 68% higher respectively. For the mobile-bearing implant, the contact pressures with the linear models increased by 25%, 91% and 69% respectively from 18.2 MPa, 19.4 MPa and 23.9 MPa found using the non-linear models.

Table 4-3 Comparison of maximum von Mises stress (MPa) in implant when UHMWPE was modelled as linear and non-linear material

			2200 N at 15° flexion	3200 N at 45° flexion	2800 N at 60° flexion
Linear	Mobile-bearing implant	Tibial bearing component	8.4	16.3	17.7
		Tibial tray	5.6	8.4	6.8
	Fixed-bearing implant	Tibial bearing component	9.2	17.2	16.6
		Tibial tray	5.3	7.8	7.2
Non-linear	Mobile-bearing implant	Tibial bearing component	5.6	9.0	8.4
		Tibial tray	1.8	2.8	2.5
	Fixed-bearing implant	Tibial bearing component	6.9	6.9	9.5
		Tibial tray	4.5	6.9	6.6

The stress distributions in the fixed- and mobile-bearing implants were then compared in conditions of normal alignment and malalignment with the non-linear material model for UHMWPE.

Figure 4-10 to Figure 4-23 display contour plots of contact pressure and von Mises stress in the fixed- and mobile-bearing implants in different alignment conditions at 45° flexion.

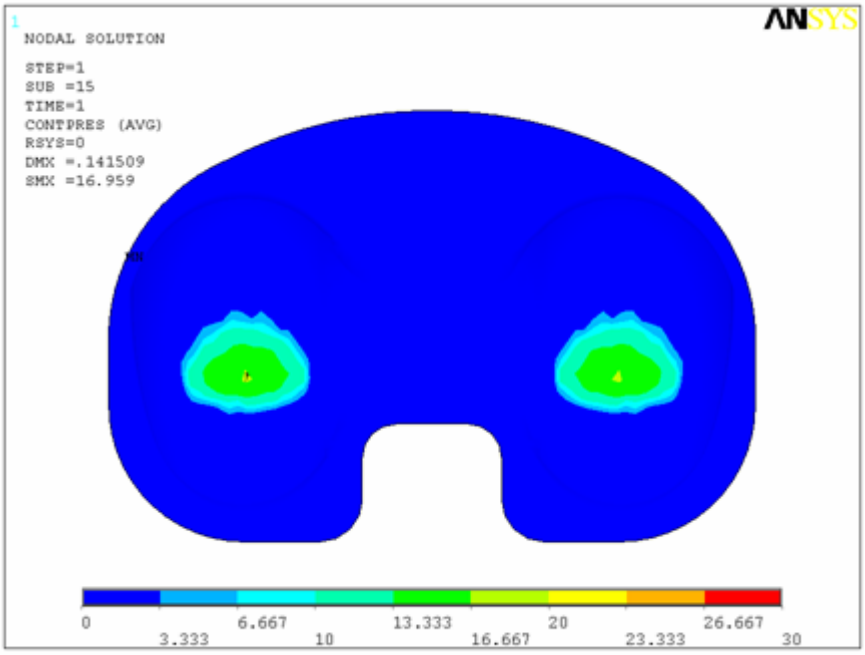

Figure 4-10 Contact pressure distribution on tibial bearing component of fixed-bearing implant at 45° flexion

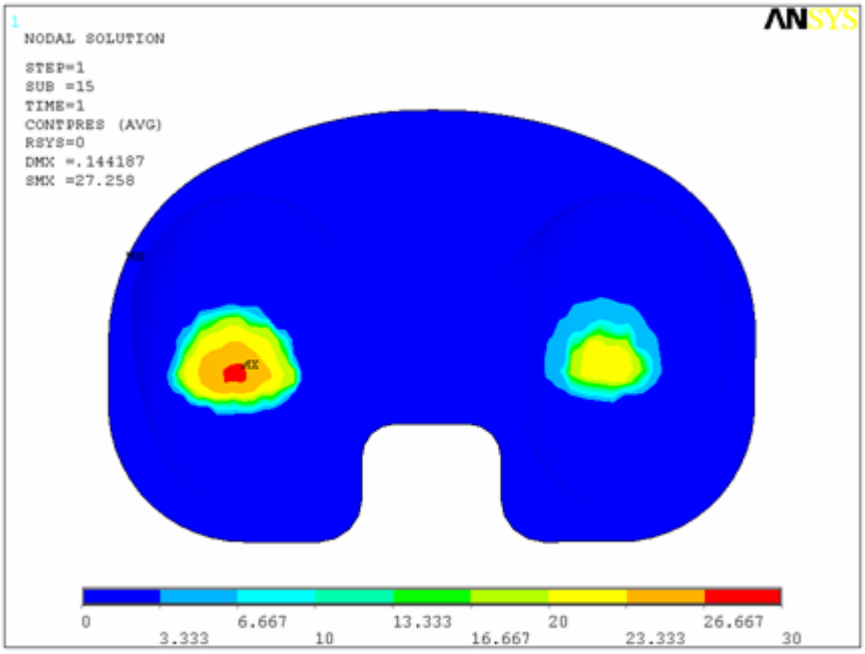

Figure 4-11 Contact pressure distribution on tibial bearing component of fixed-bearing implant at 45° flexion and 5° varus

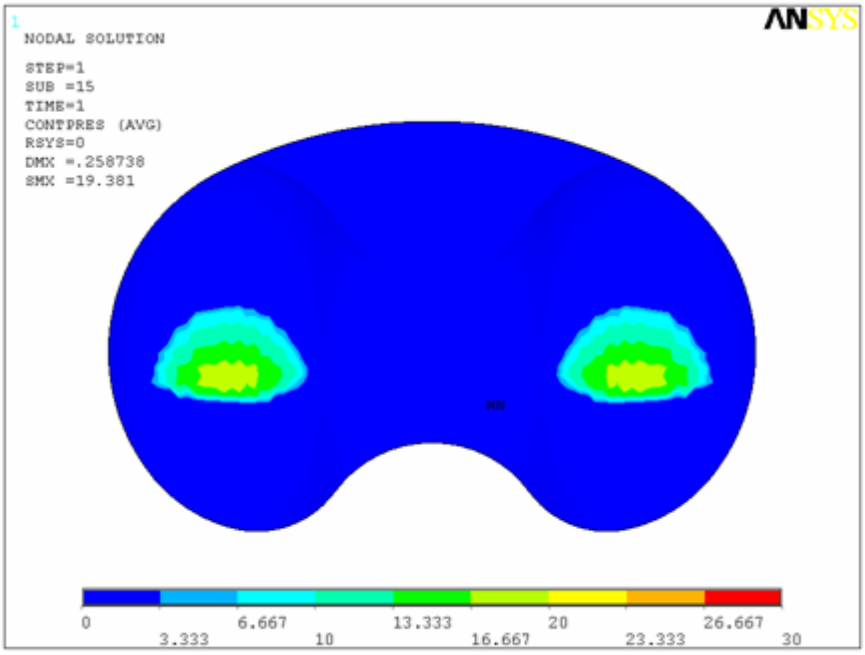

Figure 4-12 Contact pressure distribution on superior surface of tibial bearing component of mobile-bearing implant at 45° flexion

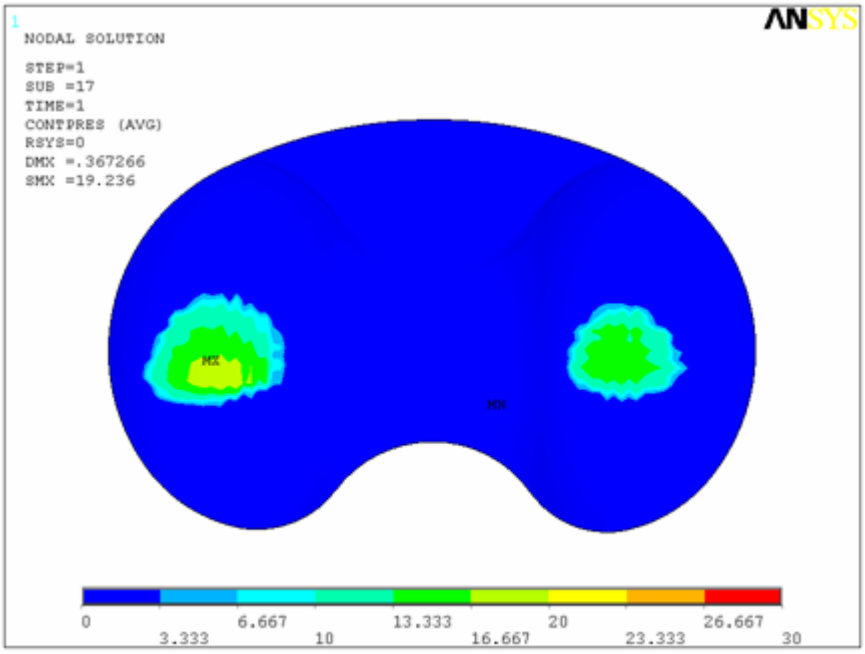

Figure 4-13 Contact pressure distribution on superior surface of tibial bearing component of mobile-bearing implant at 45° flexion and 5° varus

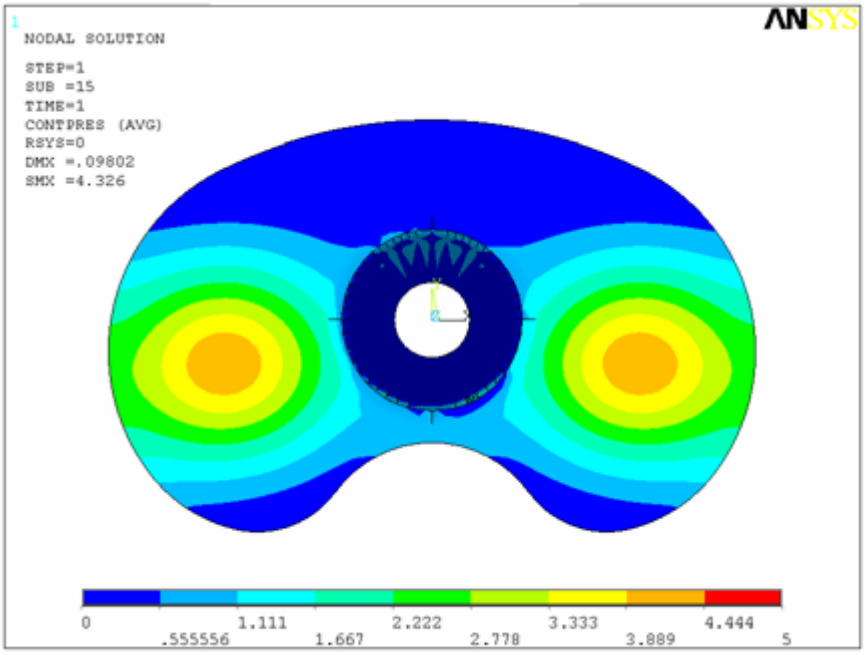

Figure 4-14 Contact pressure distribution on inferior surface of tibial bearing component of mobile-bearing implant at 45° flexion

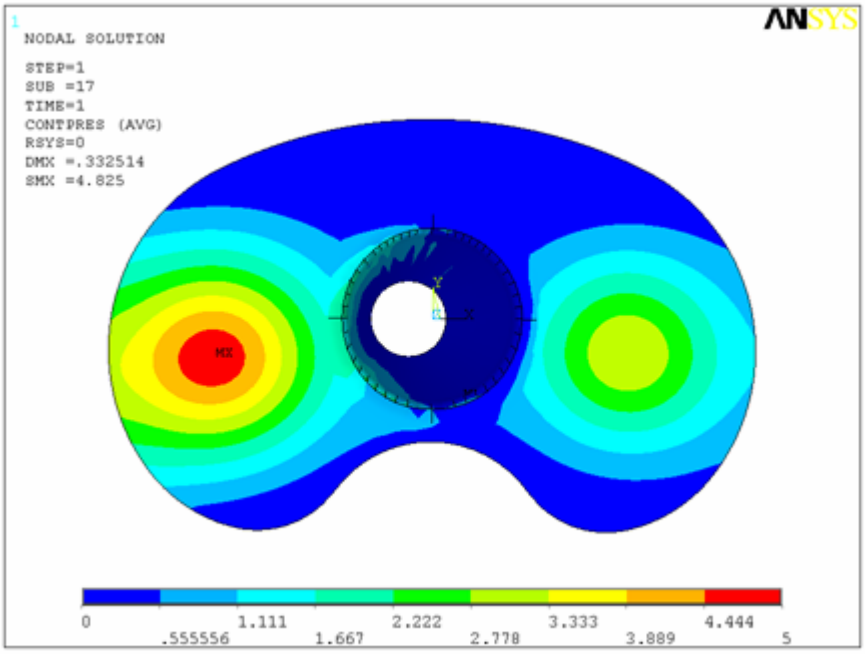

Figure 4-15 Contact pressure distribution on inferior surface of tibial bearing component of mobile-bearing implant at 45° flexion and 5° varus

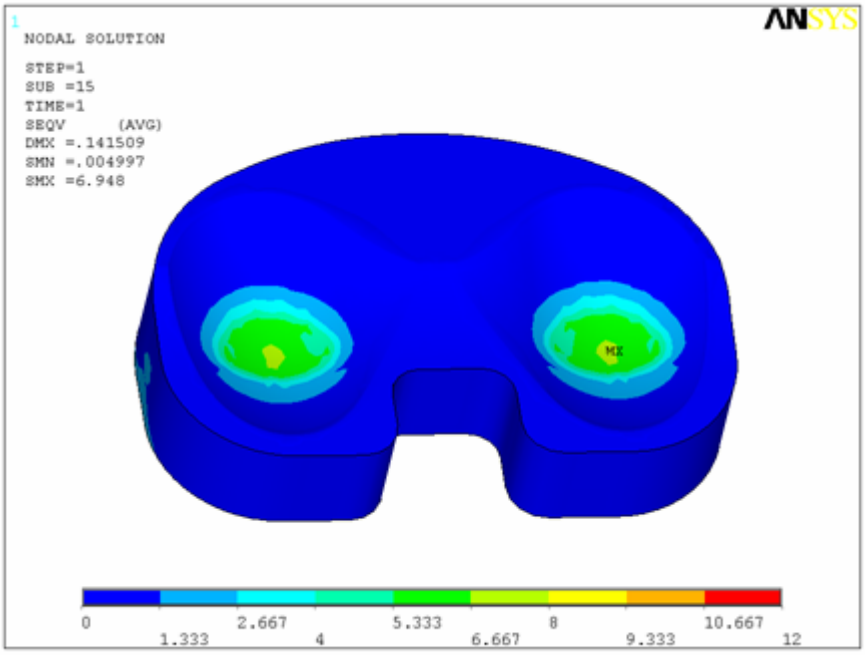

Figure 4-16 Von Mises stress distribution in tibial bearing component of fixed-bearing implant at 45° flexion

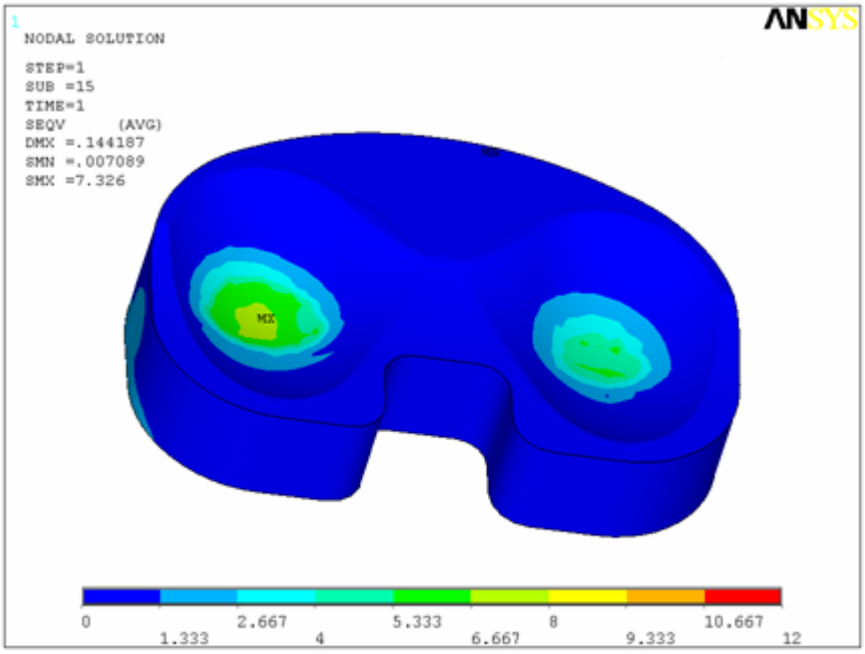

Figure 4-17 Von Mises stress distribution in tibial bearing component of fixed-bearing implant at 45° flexion and 5° varus

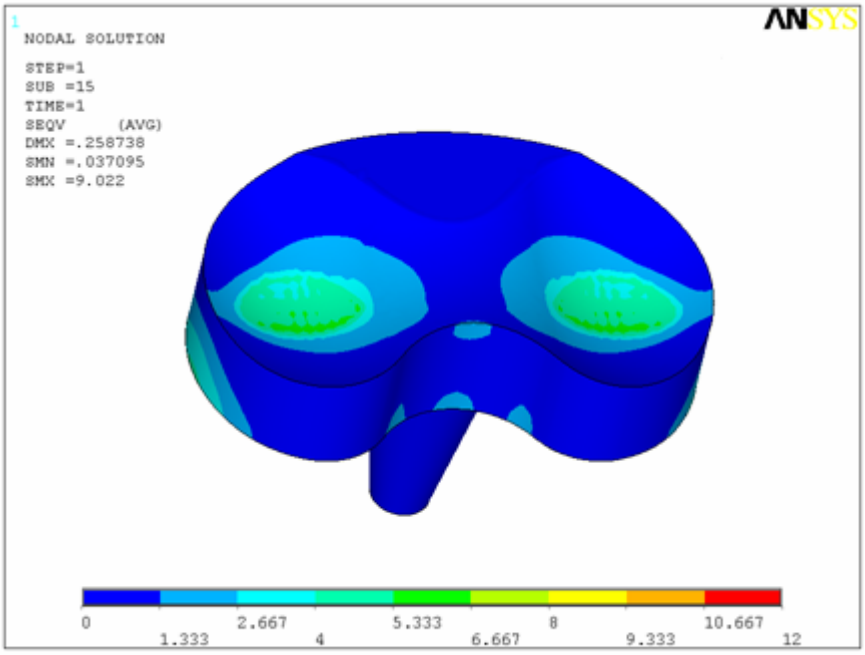

Figure 4-18 Von Mises stress distribution in tibial bearing component of mobile-bearing implant at 45° flexion

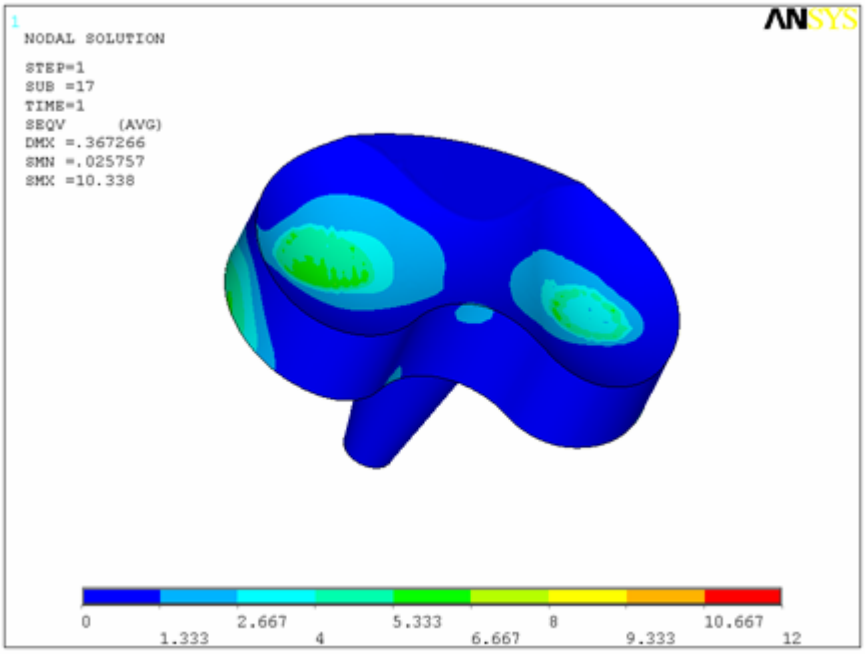

Figure 4-19 Von Mises stress distribution in tibial bearing component of mobile-bearing implant at 45° flexion and 5° varus

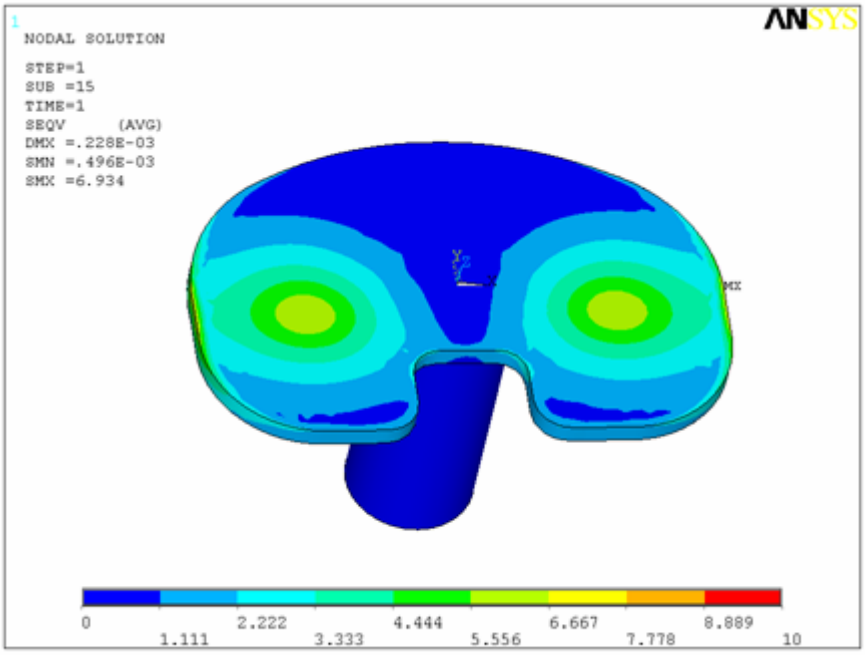

Figure 4-20 Von Mises stress distribution in tibial tray of fixed-bearing implant at 45° flexion

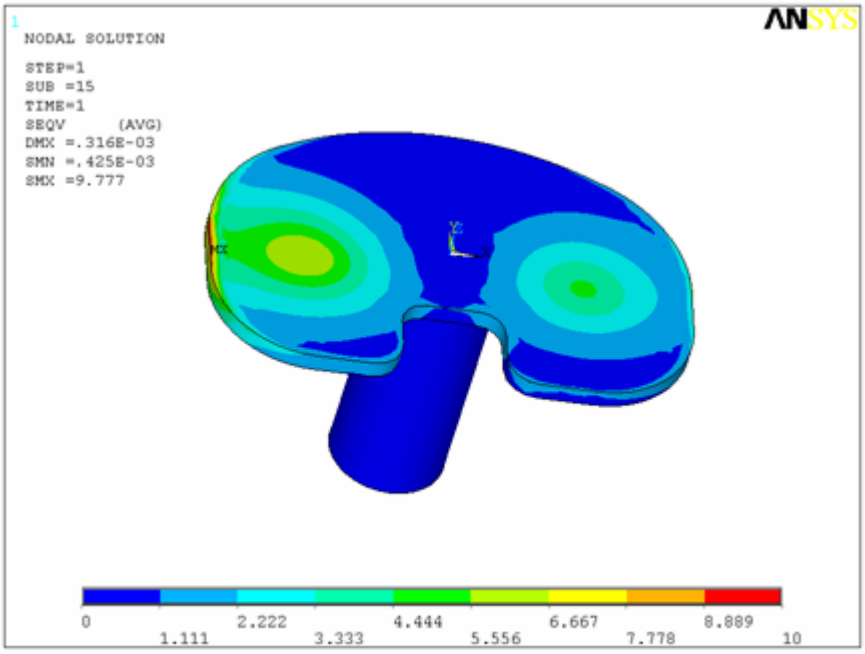

Figure 4-21 Von Mises stress distribution in tibial tray of fixed-bearing implant at 45° flexion and 5° varus

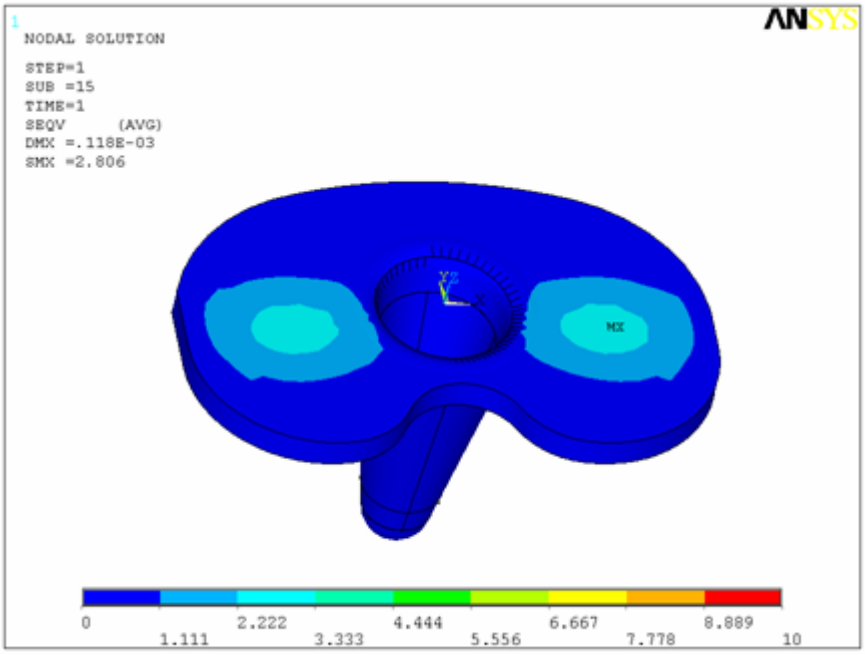

Figure 4-22 Von Mises stress distribution in tibial tray of mobile-bearing implant at 45° flexion

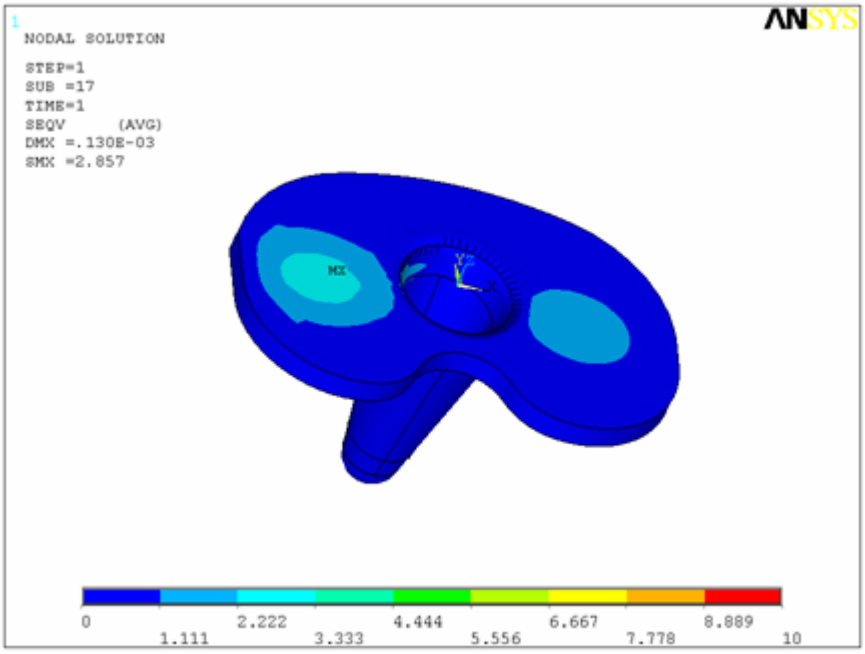

Figure 4-23 Von Mises stress distribution in tibial tray of mobile-bearing implant at 45° flexion and 5° varus

Figure 4-24 to Figure 4-35 are comparisons of maximum stress in different alignment conditions and at different stages of the gait cycle.

In Figure 4-24 to Figure 4-35:

MS stands for superior surface of mobile-bearing implant,

MI stands for inferior surface of mobile-bearing implant,

FS stands for superior surface of fixed-bearing implant,

MB stands for tibial bearing component in mobile-bearing implant,

MT stands for tibial tray in mobile-bearing implant,

FB stands for tibial bearing component in fixed-bearing implant,

FT stands for tibial tray in fixed-bearing implant.

Figure 4-24 shows maximum contact pressure at different stages of gait cycle in condition of normal alignment. The maximum contact pressures on superior contact surface in fixed-bearing implant were slightly less than those in mobile-bearing implant at 15º and 45º flexion. Although the same geometry parameter were used for the fixed- and mobile-bearing implant as stated in section 4.3.1, the larger tibial bearing component in the fixed-bearing implant resulted in slight less contact pressure in fixed-bearing implant.

Comparing Figure 4-24 and Figure 4-25, the maximum contact pressure in the fixed-bearing implant increased significantly when the alignment changed from normal to varus. The increase in maximum contact pressure at 45º and 60º of flexion are 10.3 MPa (61%) and 8.9 MPa (38%) respectively. However, the increases in contact pressure from normal alignment to varus were relatively small in the mobile-bearing implant; at 15º of flexion the maximum contact pressure on the superior contact surface of the mobile-bearing implant decreased, the reason of the decrease on maximum contact pressure is change of conformity with movement of femoral component in condition of 5º varus.

Comparing the results of Figure 4-24 and Figure 4-26 shows that contact pressure in the fixed-bearing implant increased with the change from normal alignment to malrotation at lower levels of flexion. However, malrotation had little influence on the mobile-bearing implant. The contact pressure in the fixed-bearing implant increased with malrotation by 13.3 MPa (78%) at 45º of flexion. Both maximum contact pressures decreased when changing from normal alignment to malrotation with 60º of flexion. The reason for this decrease is that the higher curvature of the contact surfaces at 60º of flexion results in an increased tolerance of malalignment. Change of contact pressure on the inferior surface of the mobile-bearing implant followed the same trend with load in all alignment conditions.

Comparison of Figure 4-24 and Figure 4-27 shows that the contact pressure increased by 5.5 MPa (34%) in the fixed-bearing implant and 7.2 MPa (40%) in the mobile-bearing implant with 15º of flexion and 2 mm maltranslation. At higher flexion, the implant is more tolerant of maltranslation and the maximum contact pressure decreased for both the fixed- and mobile-bearing models.

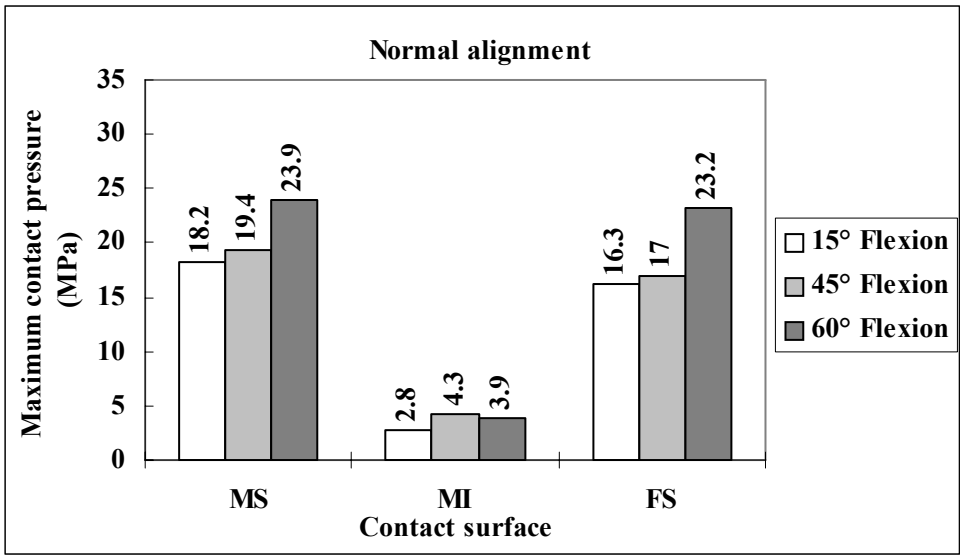

Figure 4-24 Maximum contact pressure at different stages of gait cycle in condition of normal alignment

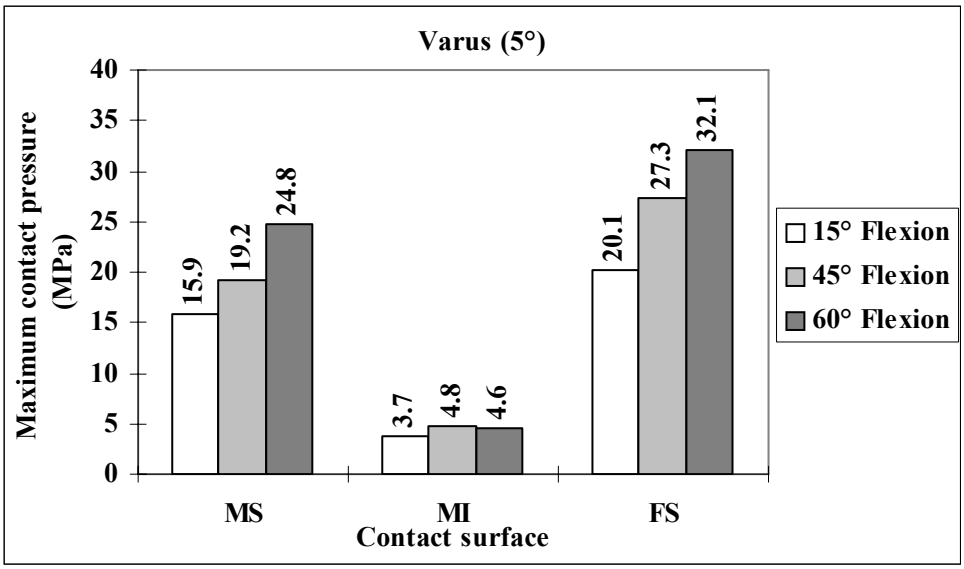

Figure 4-25 Maximum contact pressure at different stages of gait cycle in condition of 5° varus

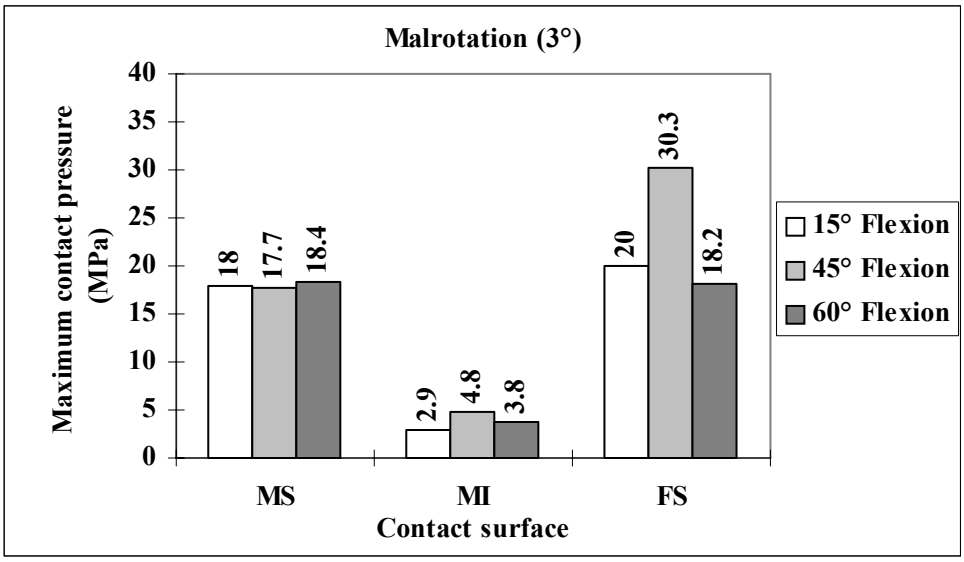

Figure 4-26 Maximum contact pressure at different stages of gait cycle in condition of 3° malrotation

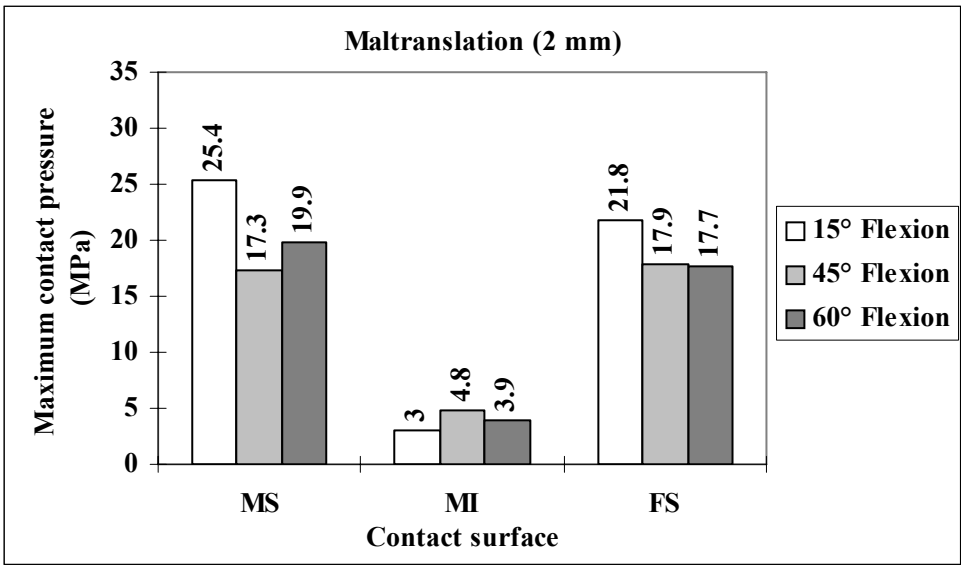

Figure 4-27 Maximum contact pressure at different stages of gait cycle in condition of 2 mm maltranslation

Figure 4-28 to Figure 4-31 show the contact area in different alignment conditions. The contact area decreased as flexion increased from 15° to 60° because of the curvature of the femoral component surface.

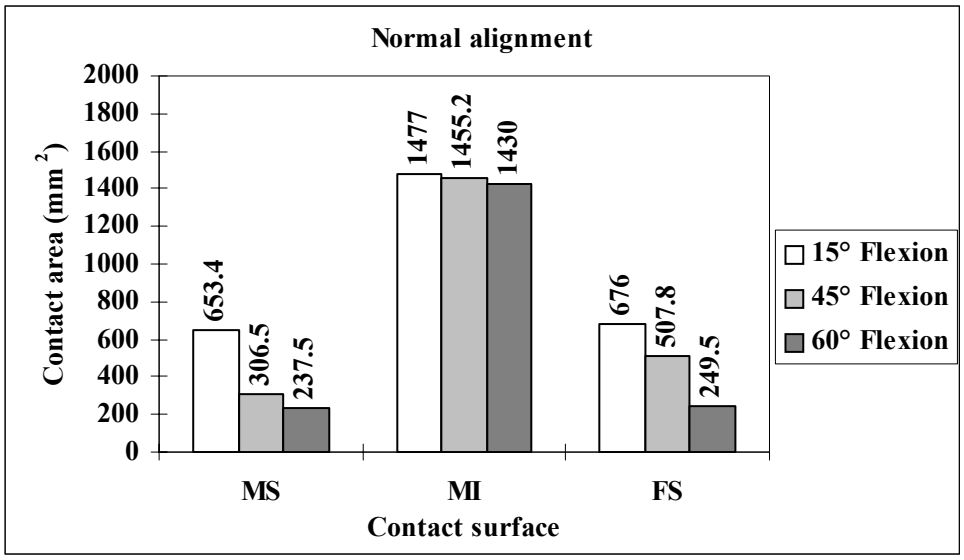

Figure 4-28 Contact area at different stages of gait cycle in condition of normal alignment

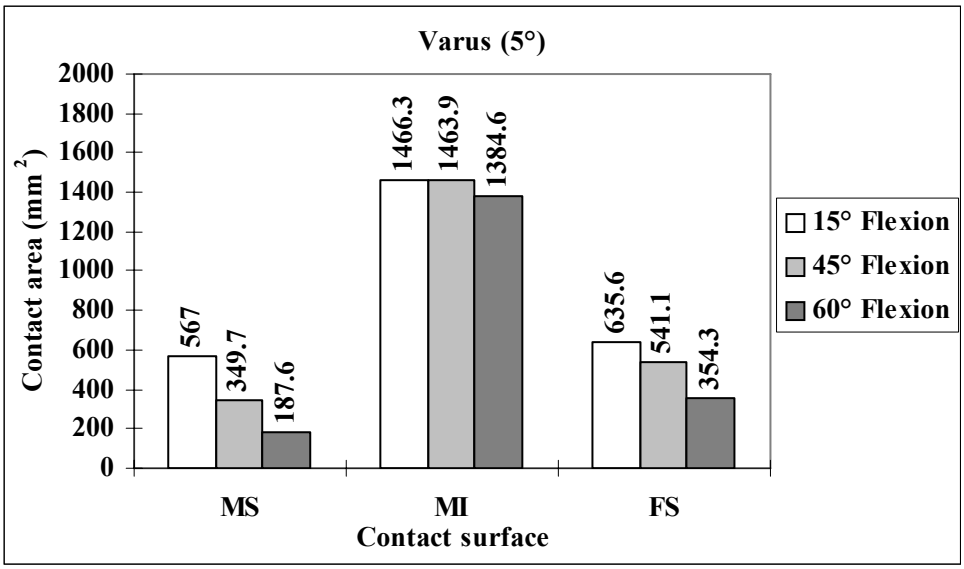

Figure 4-29 Contact area at different stages of gait cycle in condition of 5° varus

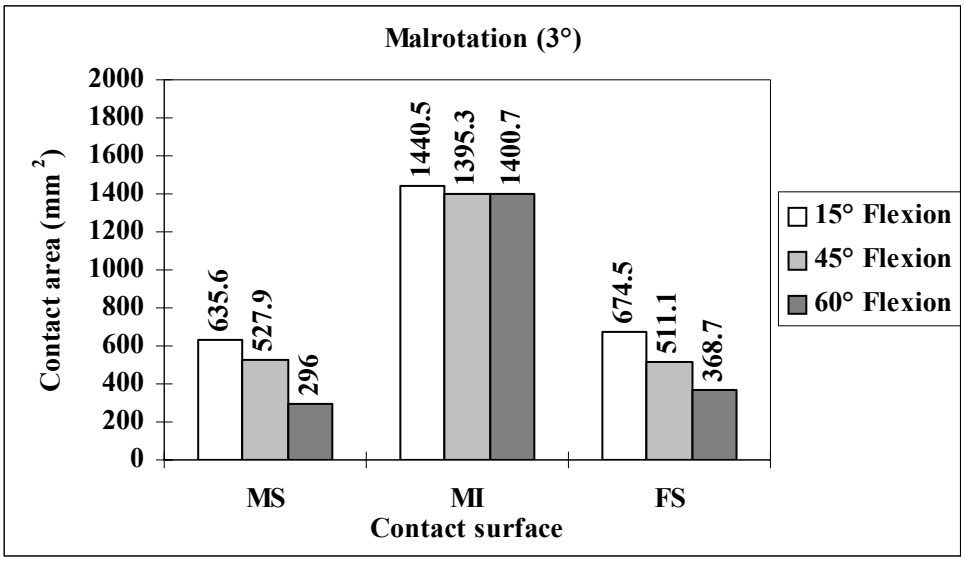

Figure 4-30 Contact area at different stages of gait cycle in condition of 3° malrotation

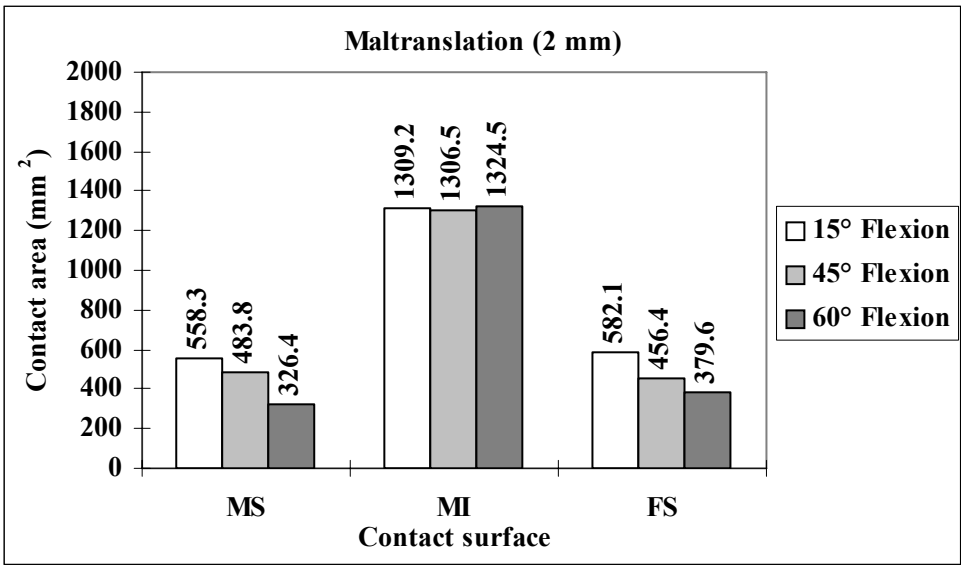

Figure 4-31 Contact area at different stages of gait cycle in condition of 2 mm maltranslation

Figure 4-32 to Figure 4-35 show the maximum von Mises stress in the prostheses for different alignment conditions. The maximum von Mises stress generally increased in the fixed-bearing implant from normal alignment to varus; it increased with the increase of flexion in the varus condition. For malrotation and maltranslation, the maximum von Mises stress in the tibial bearing component decreased at 60° flexion. The change of maximum von Mises stress

in the mobile-bearing implant had the same trend with the change of load in all alignment conditions. Comparing normal alignment with three types of malalignment, the malalignment demonstrated less influence on von Mises stress in the mobile-bearing implant. The maximum increment of von Mises stress in the mobile-bearing implant is at 15º of flexion, from 5.6 MPa for normal alignment to 8 MPa for 5º varus malalignment.

Comparing Figure 4-32 with Figure 4-33 to Figure 4-35, significant increases of von Mises stress were found in the tibial tray of the fixed-bearing implant, especially for the 5º varus condition. However, slight increases of von Mises stress were also found in the tibial tray of the mobile-bearing implant.

In summary, all of the studied malalignment conditions had a significant influence on the fixed-bearing implants. Mobile-bearing implants, on the other hand, could reduce the influence of coronal plane and rotational malalignments on maximum contact pressures. However, maltranslation increased the maximum contact pressures in mobile-bearing implants at low flexion ranges. The maximum von Mises stress in the tibial tray of the mobile-bearing implant was much lower than that in the fixed-bearing implant for all conditions, both aligned normally and malaligned.

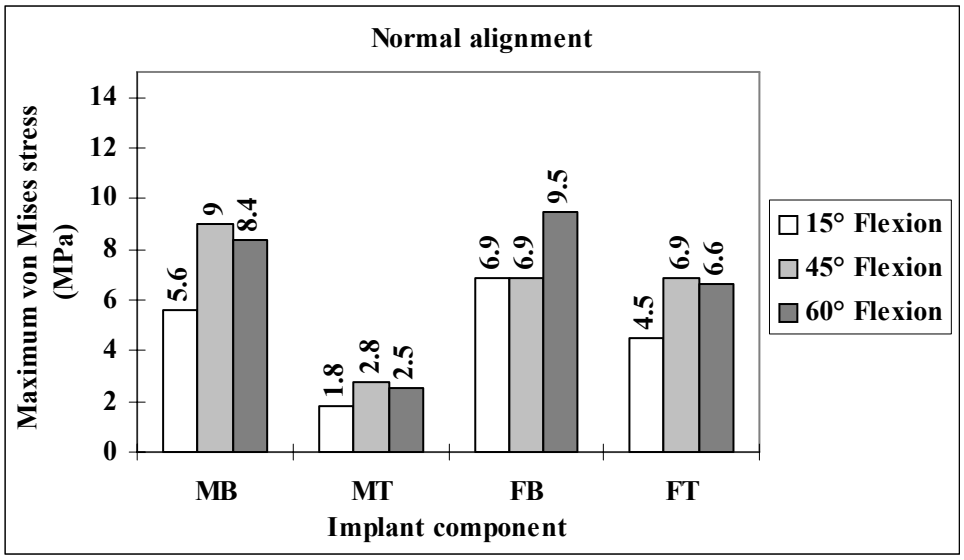

Figure 4-32 Maximum von Mises stress at different stages of gait cycle in condition of normal alignment

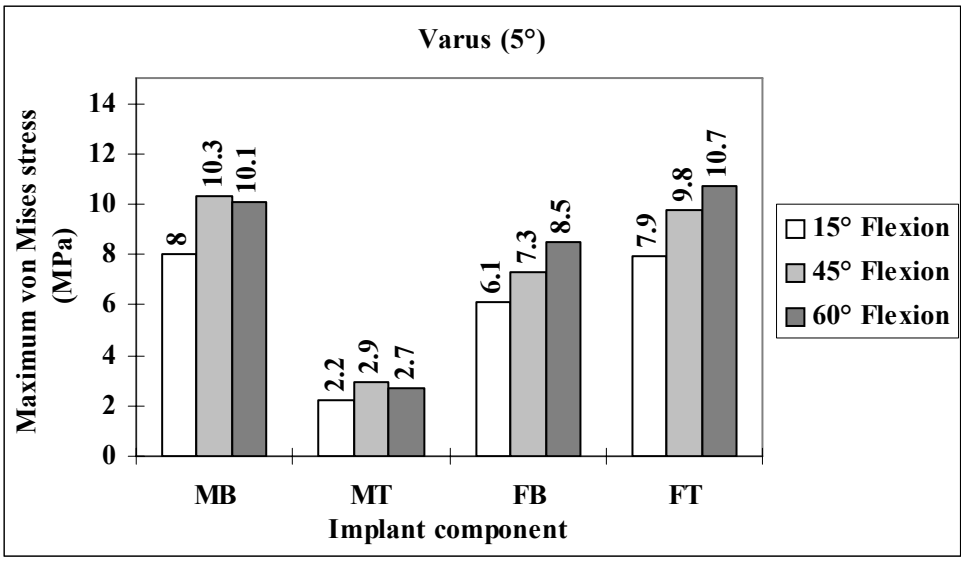

Figure 4-33 Maximum von Mises stress at different stages of gait cycle in condition of 5° varus

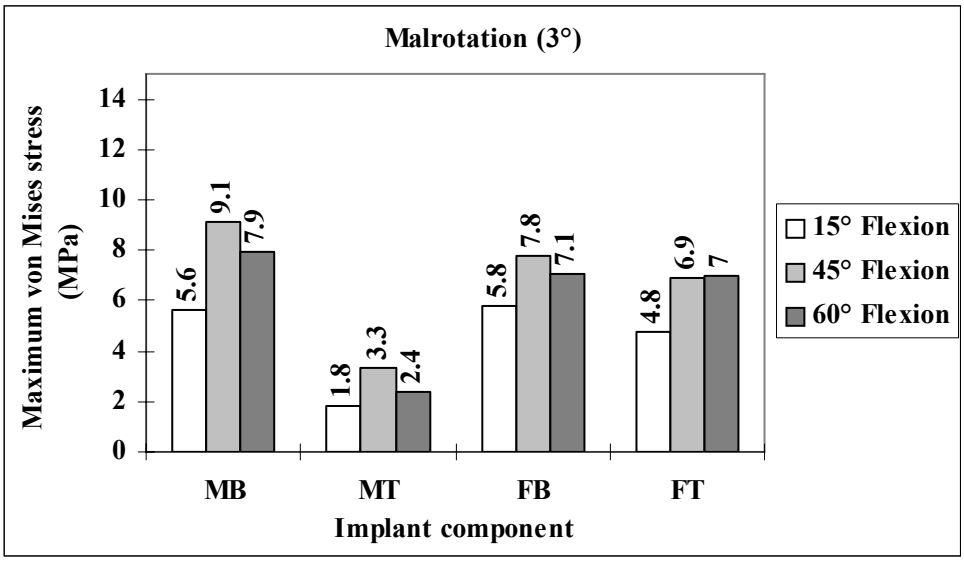

Figure 4-34 Maximum von Mises stress at different stages of gait cycle in condition of 3° malrotation

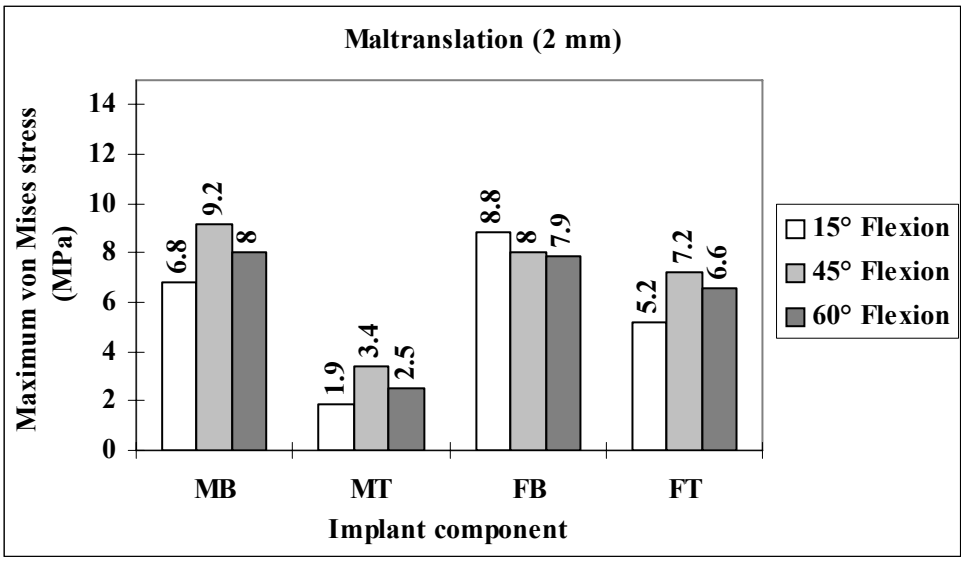

Figure 4-35 Maximum von Mises stress at different stages of gait cycle in condition of 2 mm maltranslation

4.5 Discussion and conclusions

Direct comparison of the results of this study with others is difficult, due to different implant geometries and differences in the loading and boundary conditions. The load cases in this chapter referred to Villa's research (Villa *et al.* 2004). However, Villa and his colleague used a rotating platform total knee prosthesis purposely designed and prototyped for their research. In Villa's

research, the contact area increased slightly with increase of flexion due to high conformity between the femoral component and the tibial bearing component. In their results, the contact pressure on the superior surface showed the same trend with vertical load and maximum contact pressure occurred at 45° flexion. In this chapter, the low conformity between the femoral component and the tibial bearing component happened at 60° flexion, i.e. 22 mm sagittal posterior radius of the femoral component against 40 mm sagittal radius of the tibial bearing component gave a low conformity resulting in a smaller contact area at 60° flexion (Figure 4-28). Therefore, maximum contact pressure occurred at 60° flexion in this research (Figure 4-24). However, the inferior surface was less affected by the conformity of the superior surface. Figure 4-24 shows the contact pressure on the inferior surface of the mobile-bearing implant and it demonstrates the same trend with vertical load as Villa's research results.

In this chapter, the results showed no significant difference in the calculated maximum contact pressures for fixed- and mobile-bearing implants in the normal alignment condition.

From comparative analysis on the two types of implants under vertical loading, it was found that maximum contact pressure in the fixed-bearing implant increased significantly from normal alignment to malalignment conditions. The largest increase of maximum contact pressure for the fixed-bearing implant was 10.3 MPa (61%) from normal alignment to 5º varus alignment at 60º flexion. The mobile-bearing implant performed better in minimising the influence of varus and malrotation.

In the fixed-bearing implant, malalignment caused stress increase in both tibial bearing component and tibial tray. Larger increases of von Mises stress were found in the tibial tray of the fixed-bearing implant than in that of the mobile-bearing implant; this is because the fixed tibial bearing component and tibial tray are joined together and less flexible in condition of malalignment. In contrast, malalignment had less influence on the stress in the tibial tray of the mobile-bearing implant.

It can be concluded that the mobile-bearing implant performed better under the condition of malalignment during gait cycle. This is attributed to the mobility of the tibial bearing component relative to the tibial tray in the mobile-bearing implant; therefore, it can accommodate surgical malalignment very well. In fact, the conformity of the tibial and femoral components in the mobile-bearing implant is always better than that in the fixed-bearing implant, the favourable lower contact pressures in the mobile-bearing implant being produced by the increase in tibio-femoral contact area.

In terms of lower stresses, the mobile-bearing implant performed particularly well in the malrotation condition compared to other malalignment conditions. Lower maximum stress in the tibial bearing implant can reduce the possibility of failure of the polyethylene; the lower maximum stress in the tibial tray can also reduce the possibility of failure of the tibia tray and loosening.

For both fixed and mobile-bearing implants, the performance at 60º flexion was the least affected by malalignment. This is because the low conformity at 60º flexion makes the implant more flexible between the femoral and the tibial components. However, this could cause more translation between the components with the potential failure of the polyethylene. It was thus necessary to study the relative movement between the components of total knee replacement and this is reported in the next chapter.

Chapter 5

Dynamic stress analysis of fixed- and mobile-bearing implant

5.1 Introduction

The long-term performance of a total knee replacement is dependent on the kinematics and stresses generated within the bone-implant construct. Retrieval studies have shown that the wear of total knee replacements is highly variable and this is probably attributable to the diverse kinematic and stress conditions that occur in vivo. Blunn *et al.* (1997) stated that the kinematics is the most dominant factor affecting the wear of polyethylene in total knee replacements. Barbour *et al.* (1997) found that UHMWPE wear was affected not only by the contact stress magnitude but also by the manner in which the stress is applied. The results from Barbour's tests indicated that the wear factor of UHMWPE decreased with increasing contact stress if the stress was not varied with time. If a time dependent or spatially varying stress was applied, the wear factor increased greatly when compared to similar magnitude constant contact stress.

For fixed-bearing TKR, the kinematics is controlled by bearing surface geometry in both the frontal and sagittal planes. Frontal geometry affects internal-external rotation. More concaved and conforming surfaces are more constrained than shallower surfaces. Sagittal geometry affects both internal-external rotation and AP displacement. The most influential parameter is the sagittal radius of the tibial surface.

In contrast to fixed-bearing TKR, the kinematics in mobile-bearing TKR is controlled by the geometry of both the upper and lower bearing surfaces, as well as the design of the connection between the mobile polyethylene insert and the metallic tray. Upper surface geometry can be fully conforming and thus restricted to uniaxial motion with complete contact. The upper bearing surface can also be a combination of fully and partially conforming at different ranges of flexion; a reduced contact area with flexion allows some rolling and sliding.

The mobile-bearing insert-tray connection can be designed to allow primarily AP translation, only internal-external rotation, or both.

Retrieval studies have shown that delamination associated with fatigue wear often occurs on the medial or lateral periphery of the polyethylene insert, suggesting that edge loading is occurring (Blunn *et al.* 1997, Stiehl *et al.* 1997). Polyethylene wear failure may occur under ideal alignment conditions, dependent on the activity of the patient or design and materials. However, when a design is subjected to poor alignment conditions, failure will be more rapid and complete (Taylor and Barrett 2003).

Typical experimental evaluations generally require a great deal of time, expense, and expertise. The objective of this chapter is to estimate the six degree-of-freedom tibio-femoral kinematics and the contact pressure distribution on polyethylene during a walking gait cycle. This chapter compares the kinematics of fixed- and mobile-bearing implant and the contact pressure on the tibial bearing component during the gait cycle in conditions of normal alignment and coronal malalignment.

5.2 Model description

In this chapter, a dynamic model and a finite element model were combined to simulate the contact mechanics of a fixed- and mobile-bearing implant. In the dynamic model, the motion of the knee implant was predicted using multi-body dynamics. The motion of the knee implant was then imported into the finite element model and the contact pressure in the polyethylene tibial bearing component was predicted.

5.2.1 Description of dynamic model

Models of fixed- and mobile-bearing implant refer to PFC Sigma system implants. These are slightly different from the FE models of fixed- and mobile-bearing implant described in Chapter 4. The PFC Sigma system, which was introduced clinically in the early 1980s, employs an essentially flat-on-flat

femoral-insert. The PFC Sigma implant system was introduced with the femoral component being rounded in the coronal plane and with stabilised polyethylene bearings. The PFC Sigma Rotating Platform (RP) mobile-bearing designs, which allow rotation of the tibial insert relative to the tibial tray, were also investigated in this work. The PFC Sigma RP tibio-femoral contact geometry is similar to that of the PRC Sigma fixed-bearing components. The PFC total knee replacement is a non-conforming posterior-cruciate retaining prosthesis with a polyethylene insert that is essentially flat in the sagittal plane. The PFC Sigma implant geometry data (size 3) were supplied by DePuy international, but some details of the implants were removed; only the outlines of the implants were used.

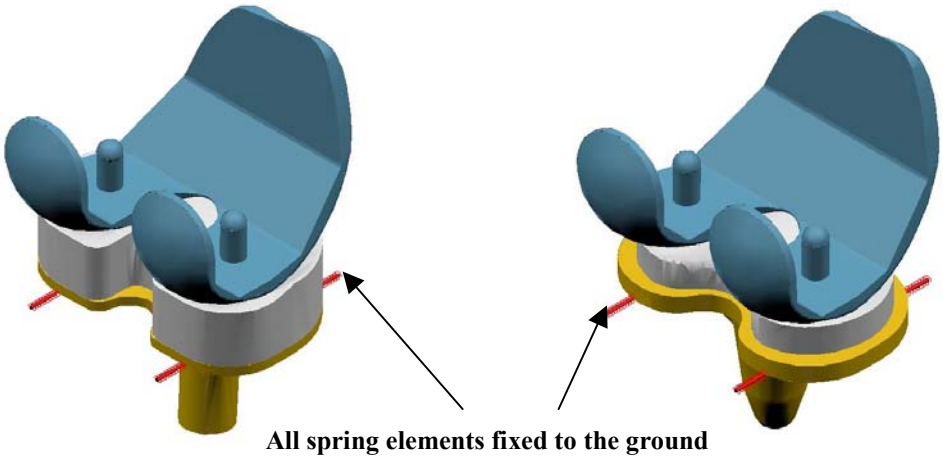

Figure 5-1 Dynamic model of fixed-bearing implant (left) and mobile-bearing implant (right)

Dynamic models of fixed- and mobile-bearing implants were developed in MSC/ADAMS (Figure 5-1). The boundary conditions applied to the model were aimed at reproducing the simulation machine for TKR performance evaluation developed by Walker *et al.* (1997). This machine has already been described in Chapter 4. The dynamic models have six degrees of freedom, three translations and three rotations of the knee joint. The femoral component was allowed to move vertically in the inferior-superior direction, to rotate about a frontal axis to simulate valgus and varus rotation and to rotate about a transverse axis to simulate flexion and extension. The tibial components were allowed to translate

in the AP and ML direction and rotate about a fixed vertical axis located in the middle of the tibial condyles to simulate internal and external rotation. With these models, a gait cycle was simulated. The time histories for the axial force, internal and external torque, AP force, and flexion and extension angles are adopted from ISO 14243-1 (Loading and displacement parameters for wear-testing machines with load control and corresponding environment conditions for test). A complete gait cycle was simulated for 1 second. The gait cycle loads are shown in Figure 5-2. The vertical axial load and the flexion-extension angle were applied to the femoral component. During normal gait, except for the occurrence of a brief valgus moment after initial contact, the knee joint is subjected to an external varus moment throughout the stance phase (Krohn 2002). The vertical load was offset by 5 mm from the centre towards the medial side to simulate varus in the normal intact knee. The anterior-posterior force and the internal-external rotational torque were applied on the tibial tray.

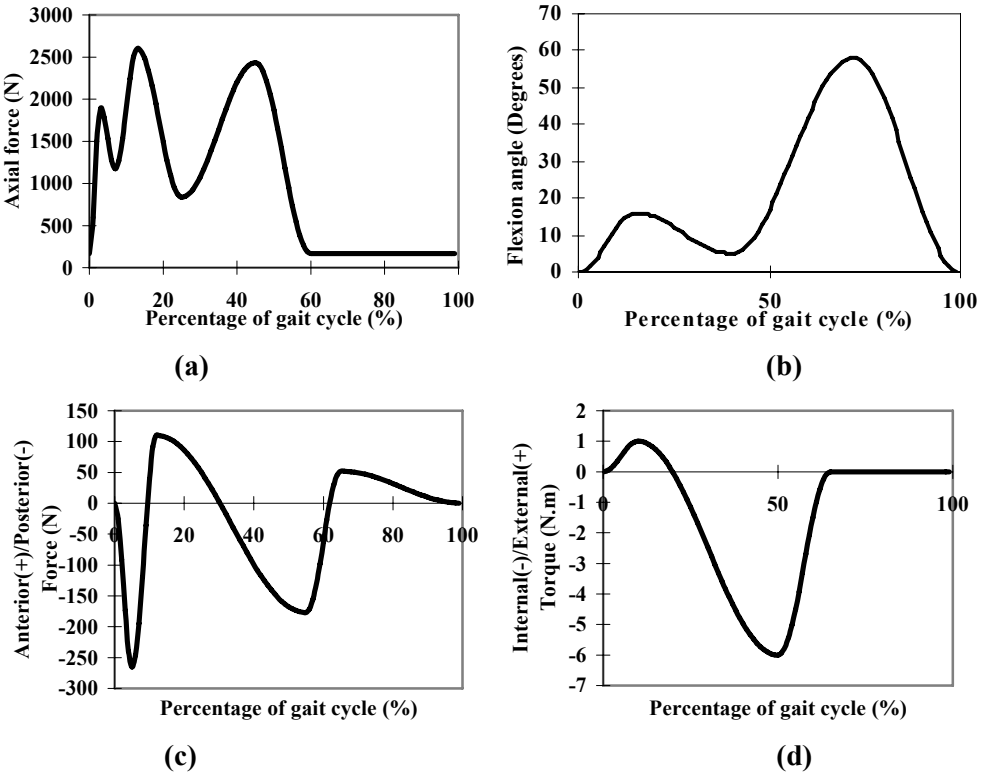

Figure 5-2 The variation of: (a) Axial force; (b) Flexion angle; (c) A/P force; (d) I/E torque as a percentage of the gait cycle

In the model of the fixed-bearing implant, contact was defined between the femoral component and the tibial bearing component. The tibial bearing component and tibial tray were fixed together. In the model of the mobile-bearing implant, two pairs of contacts were defined: the contact between the femoral component and the tibial bearing component, and the contact between the tibial bearing component and the tibial tray. In both models, the contact friction coefficient was 0.04. Four linear elastic springs and a torsion spring were used in both models to restrain the AP motion and IE rotation of the tibial tray. The four AP restraint springs were applied through a dummy part connected with the tibial tray to ensure no torsion was applied through these springs. The dummy part has only translational freedom and the tibial tray can rotate relative to the dummy part. The rotation between the tibial tray and the dummy part was restrained by the torsion spring. The total AP translation restraint spring stiffness was 30 N/mm and the IE rotation restraint was 0.6 Nm per degree according to ISO 14243-1.

5.2.2 Description of finite element model

Finite element models of fixed- and mobile-bearing implants were developed in MSC/MARC. In these models, the femoral component and the tibial tray were modelled as rigid bodies. The tibial bearing component was modelled as a deformable body. The material of the tibial bearing component, UHMWPE, was defined as a non-linear material. The definition of material property of UHMWPE is the same as in Chapter 4 (Figure 4.2). Figure 5-3 shows the finite element models of the tibial bearing component of fixed- and mobile-bearing implants.

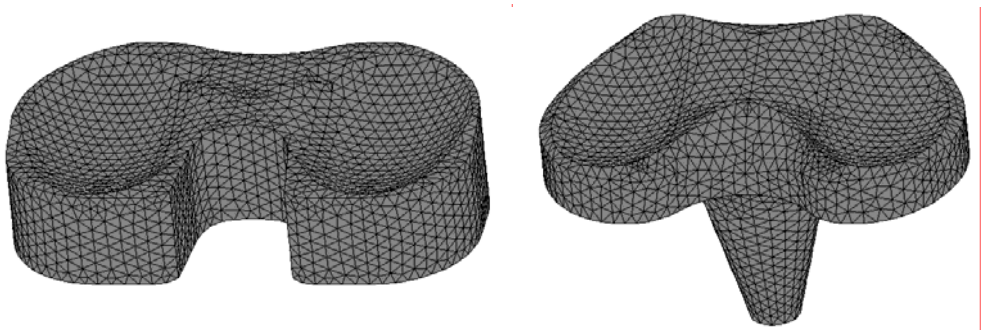

Figure 5-3 Finite element model of tibial bearing component of fixed- and mobile-bearing implant

A gait cycle was simulated in the finite element models. The motion of the tibial tray obtained from dynamic model was applied to the tibial tray in the finite element model; the axial force and flexion angle in Figure 5-2 were applied on the femoral component.

5.3 Results

Based on the dynamic models, the motion of the tibial components during the gait cycle was predicted. Using finite element models, the contact pressures in the tibial bearing components were then sequentially generated with the gait cycle load and corresponding knee positions. These results were plotted and explained in the following sections.

5.3.1 Dynamic analysis results

5.3.1.1 Contact traces on tibial components

Figure 5-4 shows the distribution of the contact points on the tibial components during a simulated gait cycle. As can be seen from the figure, the contact points on the surface of the fixed-bearing implant are distributed over a smaller area than those on the mobile-bearing implant. In the mobile-bearing implant, high conformity between the femoral component and the tibial bearing component resulted in a greater contact area, which explains the more scattered contact points in mobile-bearing implant.

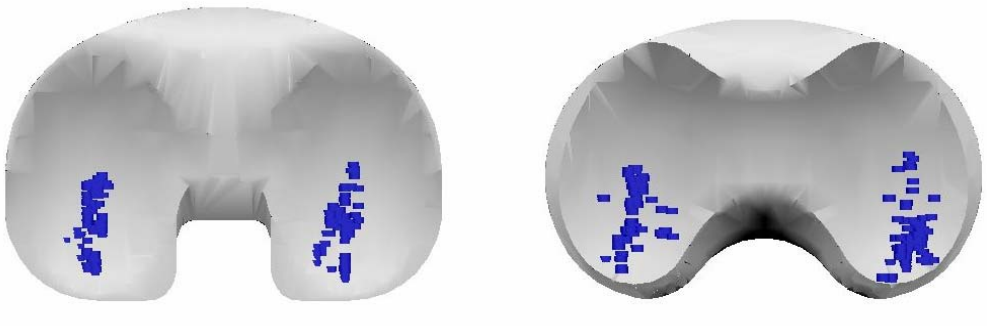

Figure 5-4 Contact trace on tibial bearing component of fixed-bearing (left) and mobile-bearing implant (right) during gait cycle

5.3.1.2 Movement of tibial components

Gait cycle loads were applied to the dynamic models developed in MSC/ADAMS. Figure 5-5 and Figure 5-6 demonstrate anterior/posterior (AP) displacement and internal/external (IE) rotation of the different tibial components.

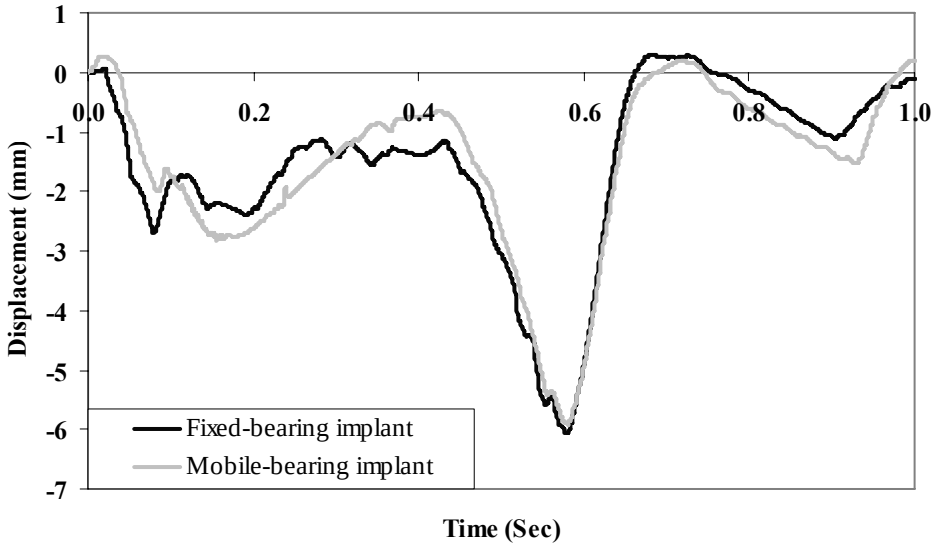

Figure 5-5 Anterior(+)/Posterior(-) displacement of tibial components in fixed- and mobile-bearing implant

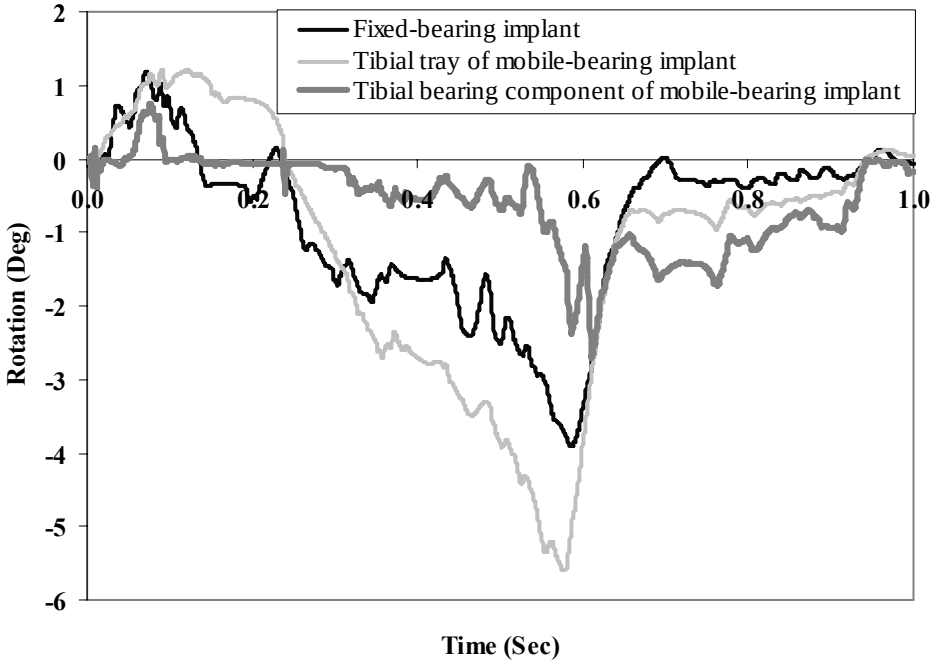

Figure 5-6 Internal(-)/External(+) rotation of tibial components in fixed- and mobile-bearing implant

Figure 5-5 indicates a similar AP translation in fixed- and mobile-bearing implant. However, the IE rotation of the two kinds of knee implant were significantly different, the IE rotation of the tibial tray in the mobile-bearing implant being much larger than that in the fixed-bearing implant (Figure 5-6).

The change of IE rotation of the tibial components in both implants followed the same trend as the rotation torque applied on the tibial tray. During the normal gait cycle, the highest rotation torque was from 0.3 to 0.6 second of the gait cycle (terminal stance to pre-swing preiod). This large rotation torque could result in rotation of the tibial tray; however, as a large axial force is also being applied on the femoral component, the rotation of the tibial components should be restricted by the friction force. In the mobile-bearing implant, the tibial bearing component and the tibial tray were not fixed. The increased congruity between the femoral component and the tibial bearing control the rotation of the tibial bearing component on the bearing surface. There is, however, the potential for rotational movement between the underside of the bearing and the top of the tibial tray. It is this uncoupling of the planes of movement which is potentially

of benefit for wear. After 0.6 second of the gait cycle (swing phase) the rotational torque reduces as the knee extends and soft tissue tensions cause the tibial tray to rotate back. The axial load reduces to a value of 167 N, the frictional force between the femoral component and the tibial bearing reduces, and the tibial bearing rotates together with the tibial tray. Figure 5-6 shows the relatively lower rotation magnitude of the tibial bearing component. The maximum rotation in the fixed-bearing implant was 3.82º internal rotation at 0.59 second. In the mobile-bearing implant, the maximum rotation of the tibial bearing component and tibial tray were 2.64º at 0.61 second and 5.44º at 0.58 second respectively. However, the maximum relative rotation between the tibial bearing component and the tibial tray was 4.39º at 0.54 second of gait cycle. There was no AP translation between the tibial bearing component and the tibial tray in the mobile-bearing implant. The relatively lower rotation between the femoral component and the tibial bearing component and no AP translation between the tibial bearing component and the tibial tray resulted in less friction distance on both contact surfaces in the mobile-bearing implant compare to the fixed-bearing implant. The lower friction distance will reduce the wear of the polyethylene.

In the mobile-bearing implant, larger rotational displacement has been observed in the finite element models. The larger rotation movement of the tibial tray will require increased restraint torque from the ligaments.

The results of the modelling of the motion of the tibial components shared similar trends with other researchers' findings (Godest *et al.* 2002, Halloran *et al.* 2005, Otto *et al.* 2003, Taylor and Barrett 2003). Under the action of AP force, the tibial components translate in the posterior direction initially, and then slightly in the anterior, the posterior translation reaching a peak value at about 0.6 second of the gait cycle. After 0.6 second of the gait cycle, the tibial components translate in the anterior direction. The IE rotation of the tibial trays followed the same trend with the applied IE torque on them. Due to the different implant geometries and differences in the loading and boundary conditions, the translation and rotation values were not exactly the same as

results from other researchers' work. Compared with Halloran's research work, the maximum posterior translation of tibial components was higher (5 mm in Halloran's research and 5.89 mm here); the maximum internal rotation of the tibial tray in the fixed-bearing implant, on the other hand, was lower (4.6° in Halloran's research and 3.9° in this research).

5.3.2 Contact stress distribution in tibial bearing component

A gait cycle was simulated in the finite element models described in 5.2.2. The motion of the tibial tray obtained from the dynamic model was applied on the tibial tray; the axial force and flexion angle in Figure 5-2 were applied on the femoral component as well. The contact pressure distributions during the gait cycle were obtained after solving the finite element models.

The maximum contact pressures on the superior surface of the fixed- and mobile-bearing implant were almost the same, 18.62 MPa in the fixed-bearing implant and 18.54 MPa in the mobile-bearing implant (Figure 5-7).

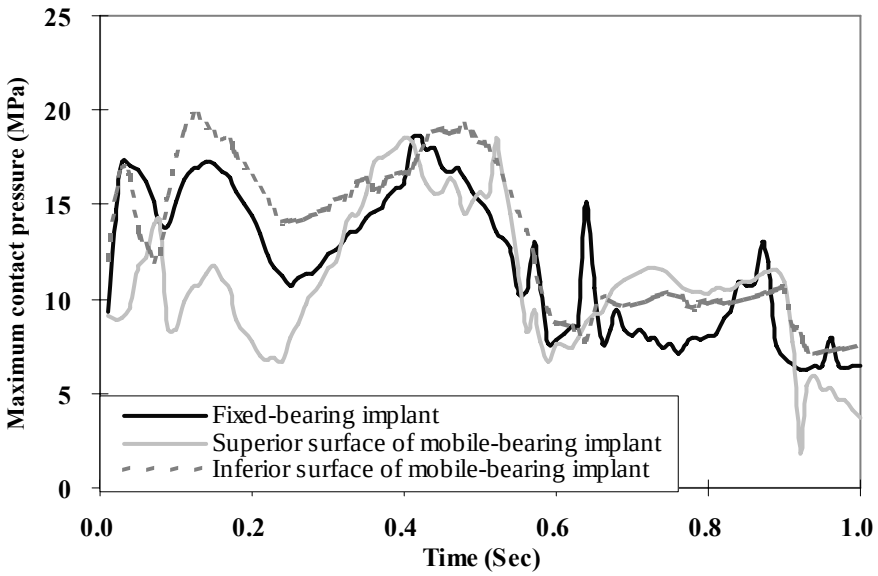

Figure 5-7 Maximum tibio-femoral contact pressure in fixed- and mobile-bearing implant during gait cycle

It was also noted that the maximum contact pressure on the inferior surface of the mobile-bearing implant was 19.72 MPa, slightly higher than that of the

superior surface. In both implants, the first three peaks of contact pressure correspond to three peaks of vertical load. The remaining peaks in the contact pressure plot were the results of unconformity contact due to relative movement between the femoral component and the tibial components. The first three peaks occurred at 0.03, 0.15 and 0.41 second respectively in the fixed-bearing implant and the inferior surface of the mobile-bearing implant; however, they occurred at 0.08, 0.15 and 0.41 second respectively on the superior surface of the mobile-bearing implant. The first two peak values of contact pressure on the superior surface of the mobile-bearing implant were relatively smaller than those in the fixed-bearing implant; the third peak value on the superior surface of the mobile-bearing implant was close to that on the fixed-bearing implant. The two relatively smaller contact pressure in the superior surface of the mobile-bearing implant were caused by the large contact area at the early stage of gait, as can be seen in Figure 5-8, where the large contact area in the mobile-bearing implant is shown. In the mobile-bearing implant, the self-adjustment of the tibial bearing component was constantly happening during the whole gait cycle. One effect of the self-adjustment was the lag of the first peak of contact pressure on the superior surface compared to the phase of the vertical load. After the first two peaks of contact pressure, the torque on the tibial tray increased and the tibial bearing component tended to rotate following the rotation of the tibial tray; this resulted in slip and non-conformal contact between the femoral component and the tibial bearing component. Because the mobile-bearing implant is not fully conformed, small contact area and high contact pressure between the femoral component and the tibial bearing component were produced at this stage. After this stage, the femoral component and the tibial bearing component conformed more and so contact pressure decreased.

Figure 5-8 shows the tibio-femoral contact area in the fixed- and mobile-bearing implants. The contact areas in the mobile-bearing implant were approximately twice those in the fixed-bearing implant. Slightly more contact area was found on the medial condyle because of the vertical force being offset medially.

Figure 5-9 shows the contact pressure distribution in the fixed-bearing implant at 0.03, 0.15 and 0.41 second respectively. Figure 5-10 and Figure 5-11 show the contact pressure distribution in the mobile-bearing implant at 0.08, 0.15 and 0.41 second respectively. Comparing the contact pressure distribution in the fixed- and mobile-bearing implants, the contact in the fixed-bearing implant is concentrated on a small area; a larger contact area is shown in the mobile-bearing implant, although only a very small area was subject to high contact pressures. This was due to the process of self-adjustment of conformity during rotation of the tibial bearing components. In Figure 5-10 b, the smaller area of stress concentration was due to inaccurate CAD femoral component geometry. On the inferior surface of the mobile-bearing implant, high contact pressure appeared in the insertion area. This was the result of the insert of the tibial bearing component being in contact with the tibial tray when the movement and force were transferred between them.

It was also noticed that the tibial bearing component in the fixed-bearing implant is thicker than that in the mobile-bearing implant. The influence of the thickness of the tibial bearing component on the contact pressure will be further discussed in section 5.5.

In Figure 5-7, the maximum contact pressure on the inferior contact surface of the tibial bearing component is 19.72 MPa. This high contact pressure will cause wear of the inferior surface of the tibial bearing component in the mobile-bearing implant.

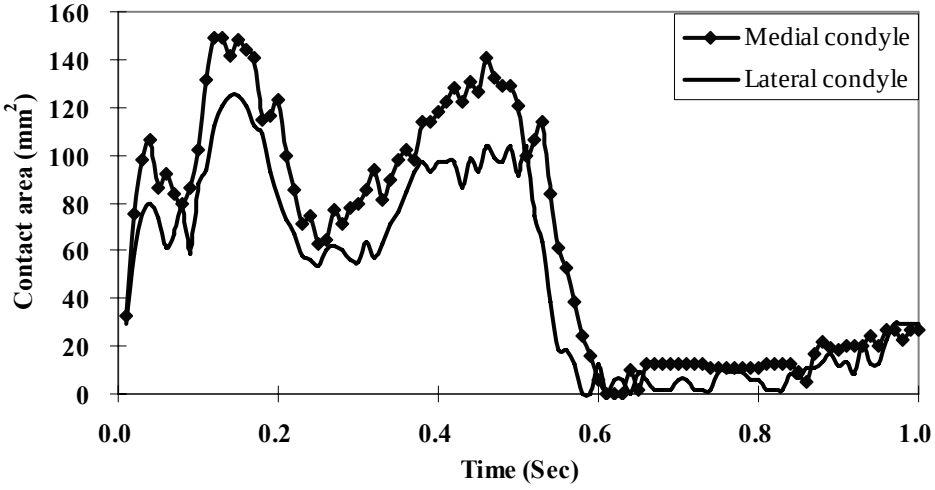

(a)

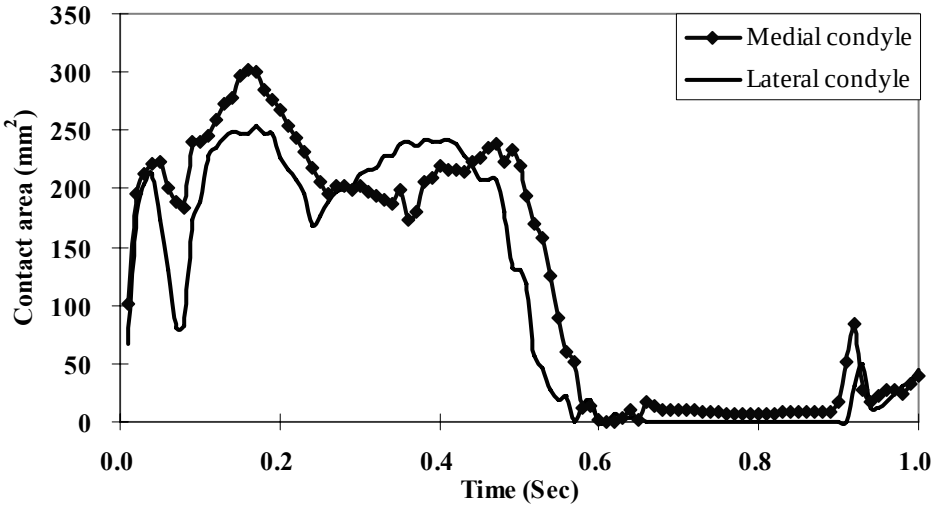

(b)

Figure 5-8 Tibio-femoral contact area in (a) fixed-bearing implant and (b) mobile-bearing implant during gait cycle

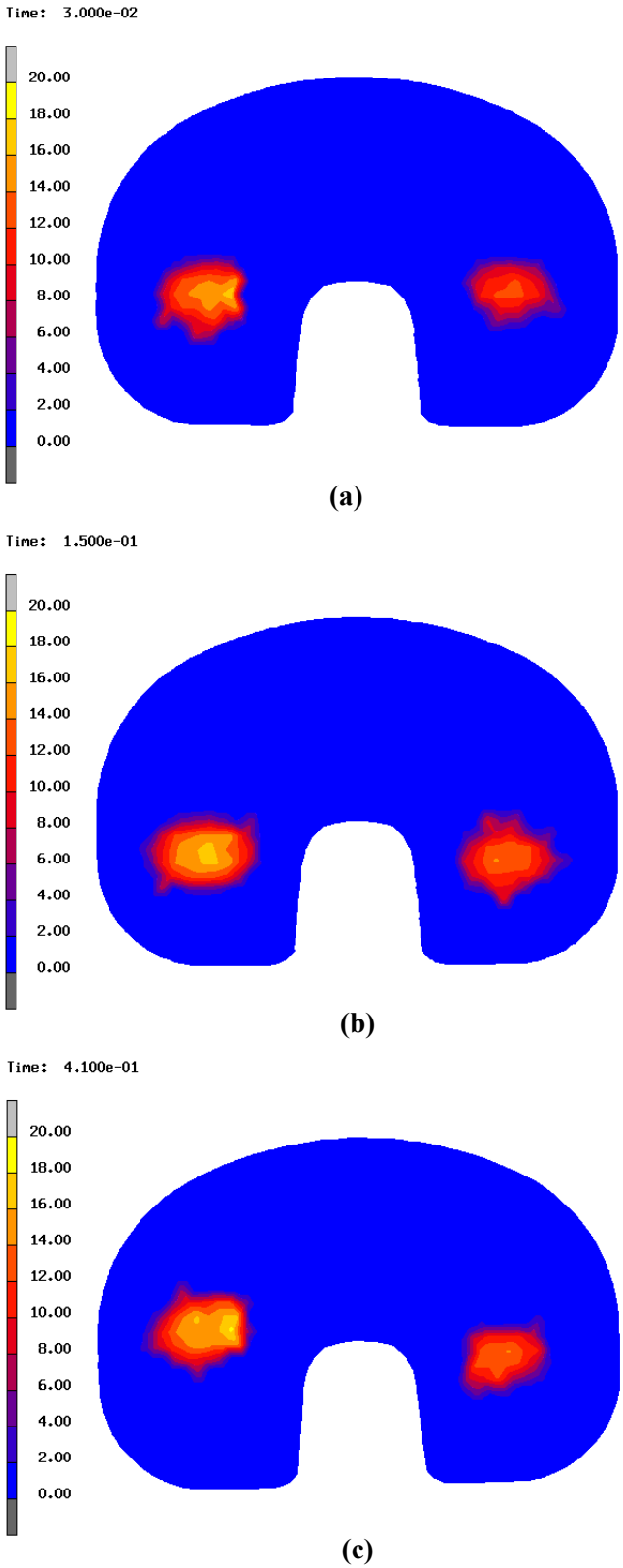

Figure 5-9 Contact pressure distribution in fixed-bearing implant at: (a) 0.03 second, (b) 0.15 second and (c) 0.41 second

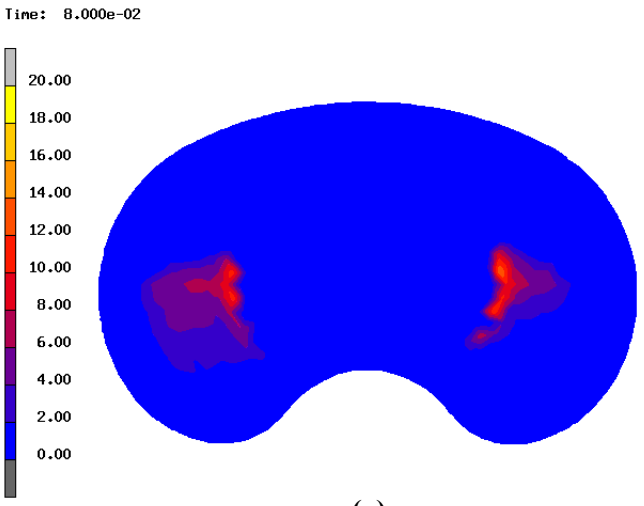

(a)

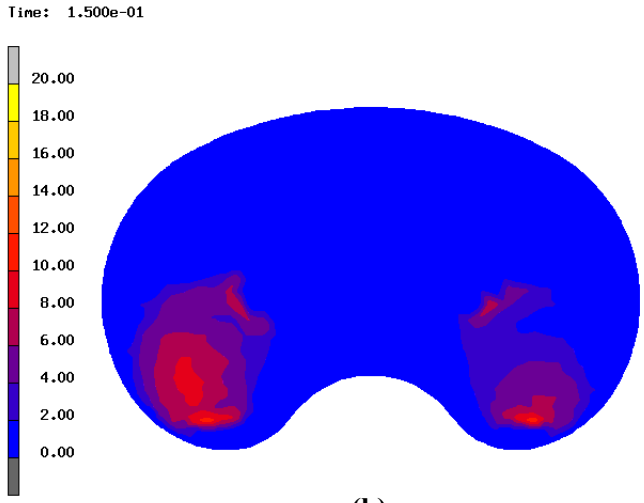

(b)

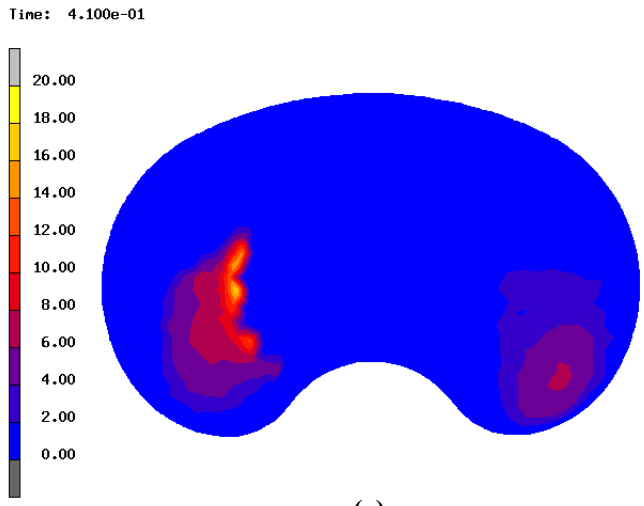

(c)

Figure 5-10 Contact pressure distribution at superior surface of mobile-bearing implant at: (a) 0.08 second, (b) 0.15 second and (c) 0.41 second

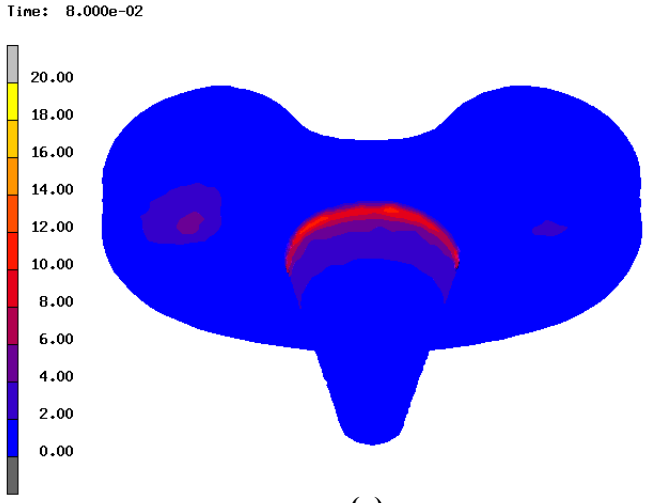

(a)

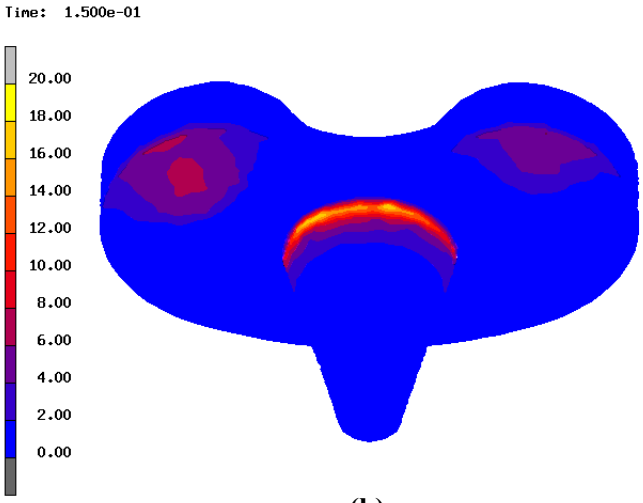

(b)

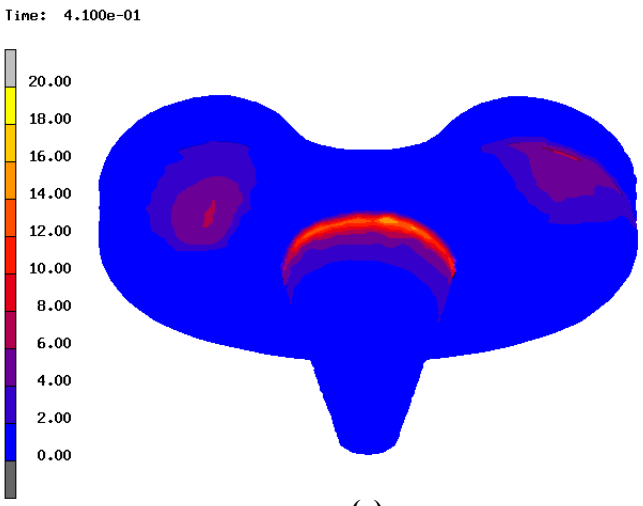

(c)

Figure 5-11 Contact pressure distribution at inferior surface of mobile-bearing implant at: (a) 0.08 second, (b) 0.15 second and (c) 0.41 second

5.4 Influence of malalignment on performance of different implant

To simulate the situation of varus/valgus malalignment, the axial load was offset by 5 mm and 10 mm from the centre towards the medial/lateral side respectively (Haider *et al.* 2001). As a result of load offset, the medial:lateral loading ratio was 60:40 when the axial force was offset medially by 5 mm, and 72.5:27.5 when the axial force was offset medially by 10 mm.

5.4.1 Influence of malalignment on motion

Figure 5-12 shows AP translation in the fixed- and mobile-bearing implant in different conditions of malalignment. No obvious difference of AP translation was found in different conditions of malalignment.

Figure 5-13 shows IE rotation in the fixed- and mobile-bearing implant in different conditions of malalignment. In the fixed-bearing implant, the maximum value of rotation of the tibial components was almost the same in different conditions of malalignment. In the mobile-bearing implant, smaller IE rotation of the tibial tray was found in condition of varus. Compared to light varus (normal knee condition), excessive valgus increased the rotation of the tibial tray by 48.2% from 5.58° to 8.27°. As a consequence, the increase in rotation of the tibial tray will add the burden on the ligaments. It was also noted that the direction of rotation of the tibial bearing components is sometimes opposite in conditions of varus and valgus during swing phase.

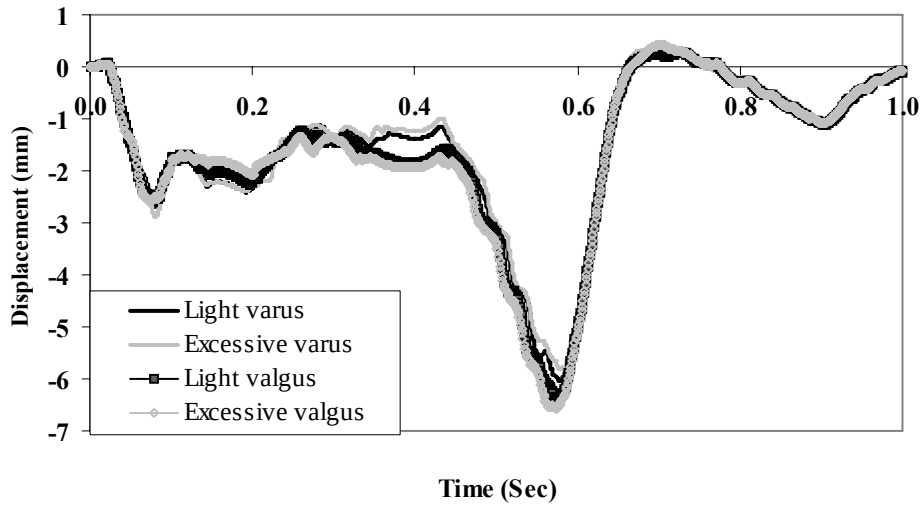

(a)

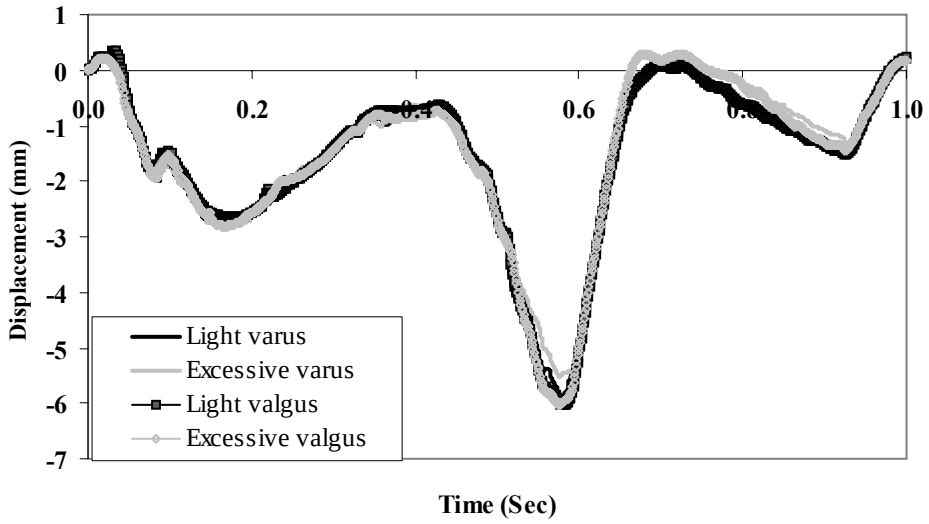

(b)

Figure 5-12 Anterior(+)/Posterior(-) displacement of tibial components in (a) fixed-bearing implant and (b) mobile-bearing implant in different conditions of alignment

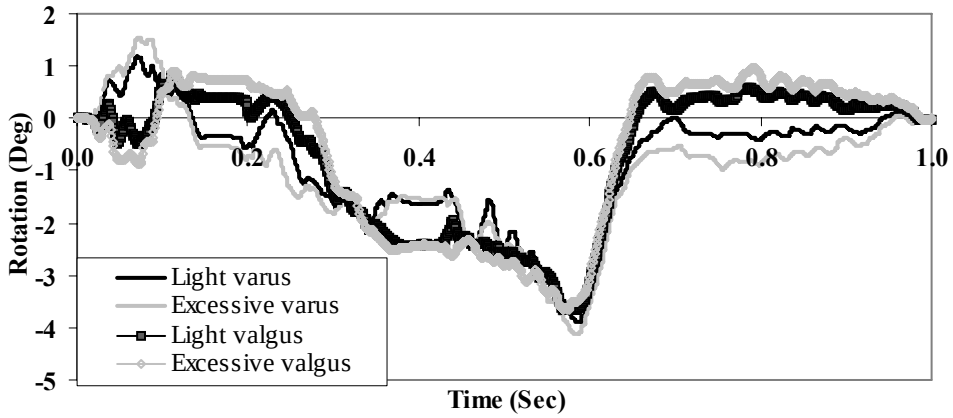

(a)

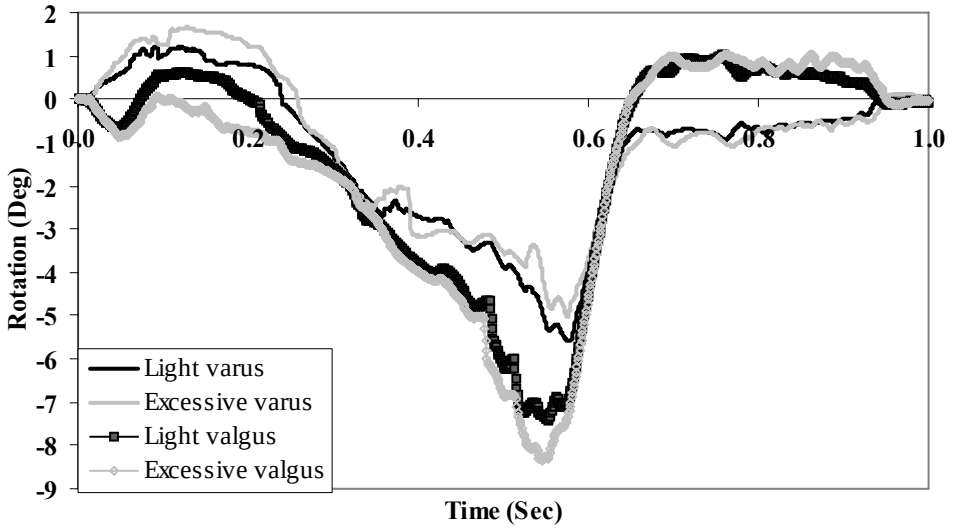

(b)

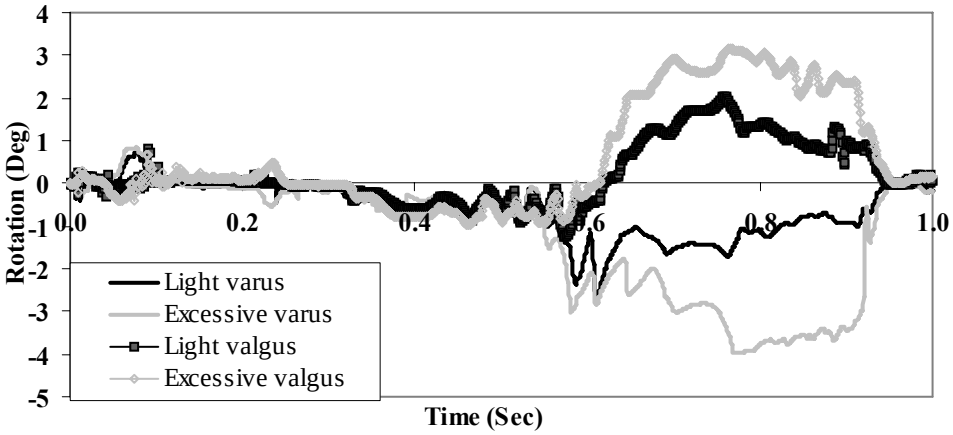

(c)

Figure 5-13 Internal(-)/External(+) rotation of (a) tibial components of fixed-bearing implant, (b) tibial tray of mobile-bearing implant and (c) tibial bearing component of mobile-bearing implant in different conditions of alignment

5.4.2 Influence of malalignment on stress distribution

The maximum tibio-femoral contact pressure in the fixed- and mobile-bearing implant were compared in different conditions of malalignment (Figure 5-14).

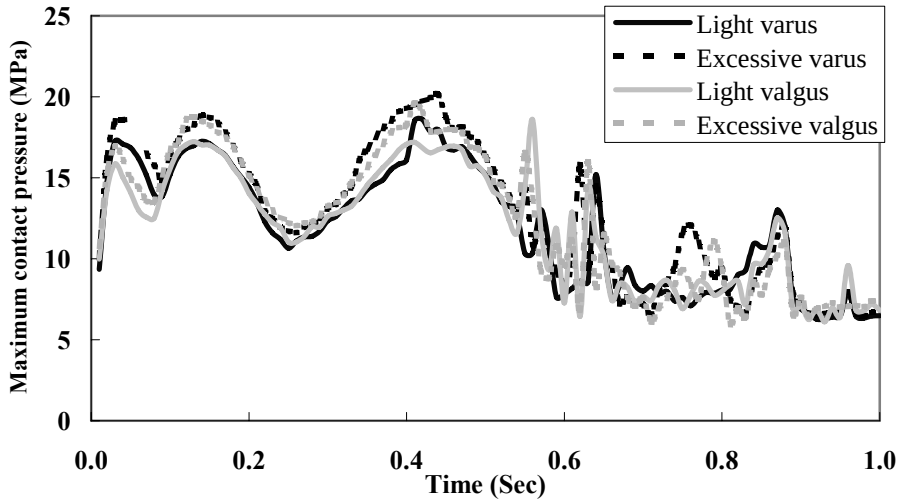

(a)

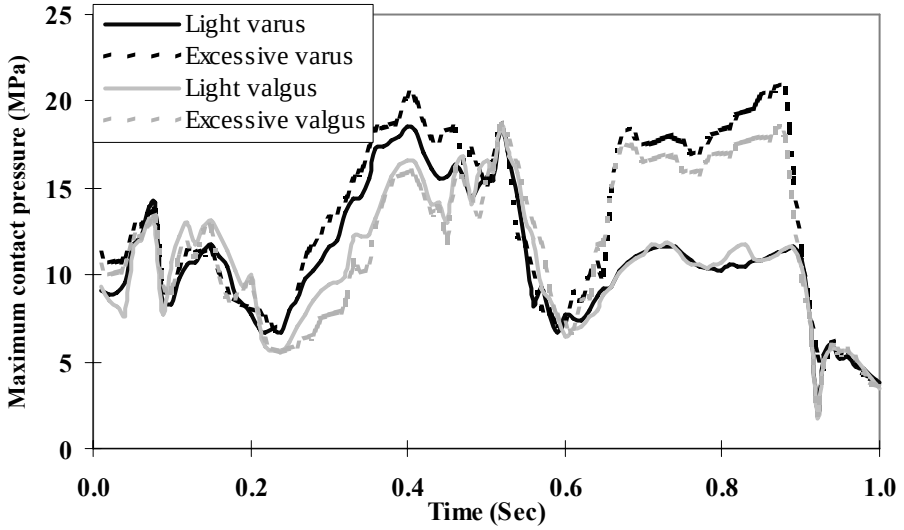

(b)

Figure 5-14 Tibio-femoral contact pressure in (a) fixed-bearing implant and (b) mobile-bearing implant in different conditions of alignment

From all fixed-bearing implant results, only slightly higher contact pressures were found in condition of excessive varus and valgus. This means that the fixed-bearing implant was not very sensitive to varus/valgus malalignment, due

to the lower conformity and thicker tibial bearing component in the fixed-bearing implant. In the mobile-bearing implant, on the other hand, excessive varus/valgus increased the contact pressure during the swing phase (after 60% gait cycle). This increase was related to the rotation of the tibial bearing component (Figure 5-13 c). Excessive varus/valgus increased the IE rotation and contact pressure in the tibial bearing component.

Figure 5-15 and Figure 5-16 show the contact areas on the medial and lateral condyles in fixed- and mobile-bearing implants in different conditions of malalignment. In the fixed-bearing implant, a larger contact area was noted on the medial side in condition of varus and on the lateral side in condition of valgus, the difference between the two sides increasing in conditions of excessive malalignment. However, in the mobile-bearing implant, the maximum contact area is approximately 300 mm^2 in all conditions, and the smaller contact area decreased slightly in excessive malalignment (Figure 5-16 c and d). This characteristic is attributed to the high conformity design of the mobile-bearing implant.

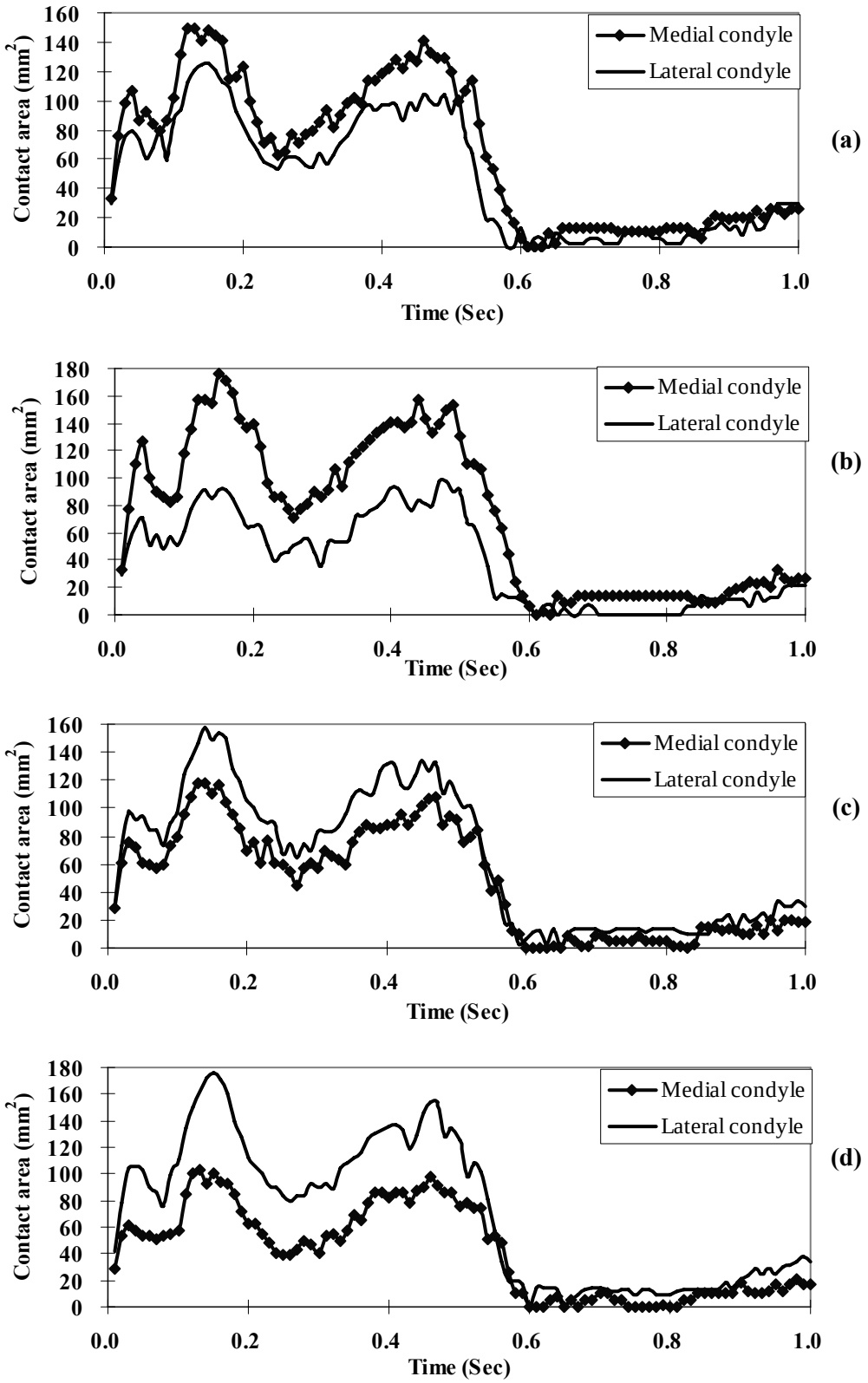

Figure 5-15 Tibio-femoral contact area in fixed-bearing implant in condition of: (a) light varus, (b) excessive varus, (c) light valgus and (d) excessive valgus

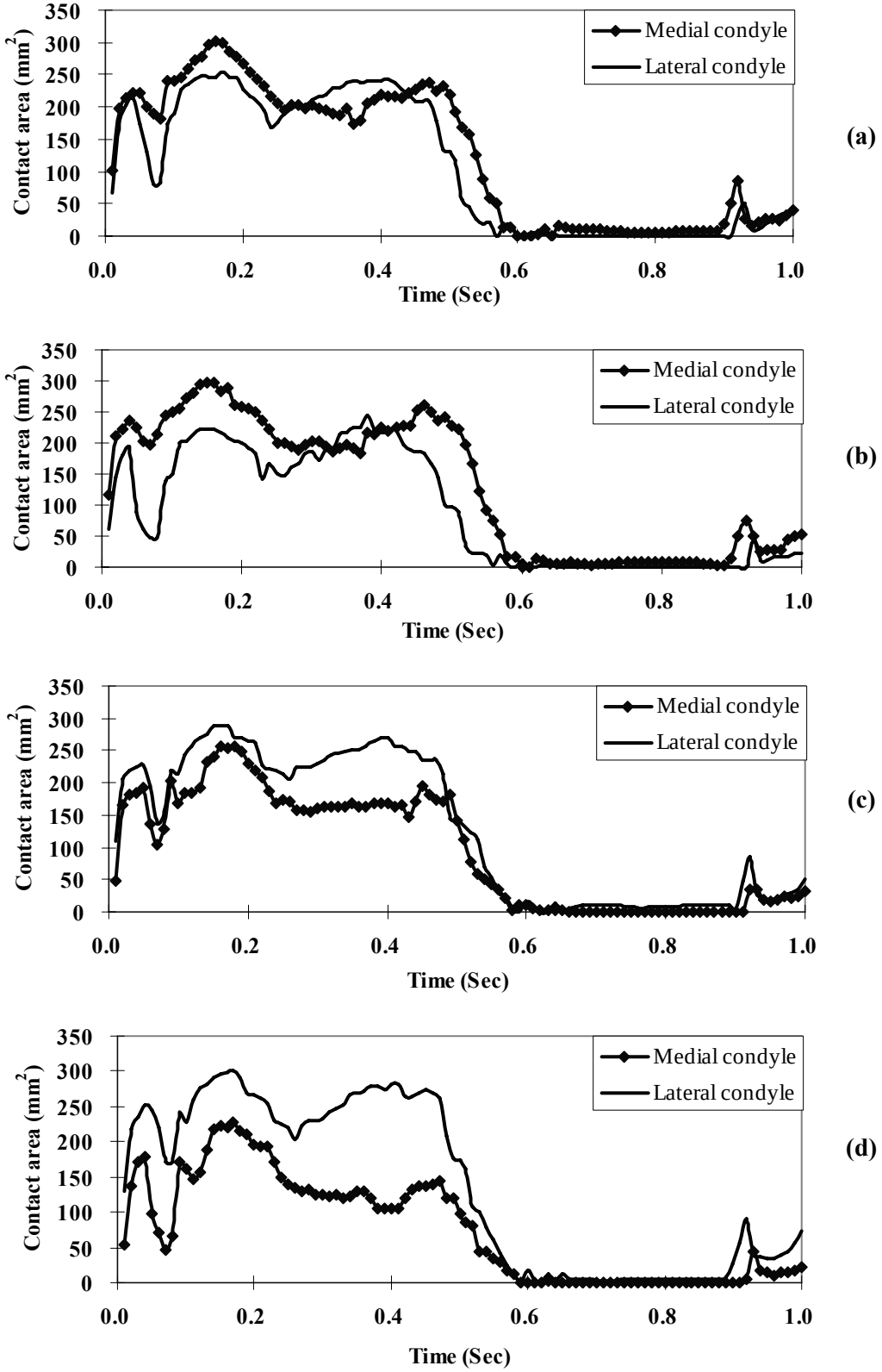

Figure 5-16 Tibio-femoral contact area in mobile-bearing implant in condition of: (a) light varus, (b) excessive varus, (c) light valgus and (d) excessive valgus

5.5 Influence of thickness of tibial bearing component on stress distribution

In sections 5.2 to 5.4, the fixed- and mobile-bearing implants were investigated using PFC Sigma system implant geometry. The thicknesses of the tibial bearing component in the fixed- and mobile-bearing implants were 6.8 mm and 12.3 mm respectively. In this section, the influence of the thickness of the tibial bearing component on the stress distribution in knee implants will be investigated using thicknesses of 6.8, 9.6 and 12.3 mm respectively. Figure 5-17 shows the contact pressures in knee implants with different thickness of tibial bearing component. In the fixed-bearing implant (Figure 5-17 a), the highest contact pressures were found when the thickness of the tibial bearing component was 6.8 mm; the highest contact pressures for 9.6 mm and 12.3 mm thick components were, however, very similar. This suggests that a 9.6 mm thick tibial bearing component would have similar strength to a 12.3 mm one; the 9.6 mm thick tibial bearing component has the advantage that less bone would need to be removed when it was fitted. In Figure 5-17 a, peaks of maximum contact pressure at 0.64 and 0.85 second of gait cycle in 9.6 mm and 12.3 mm design were due to local element mesh and the stress was concentrated on one node.

In the mobile-bearing implant, the contact pressures on the superior surface were almost the same for all different thicknesses of tibial bearing component (Figure 5-17 b). The lowest maximum contact pressure on the inferior surface occurred with a 6.8 mm thickness. This suggested that the tibial bearing component of 6.8 mm thickness had the better performance.

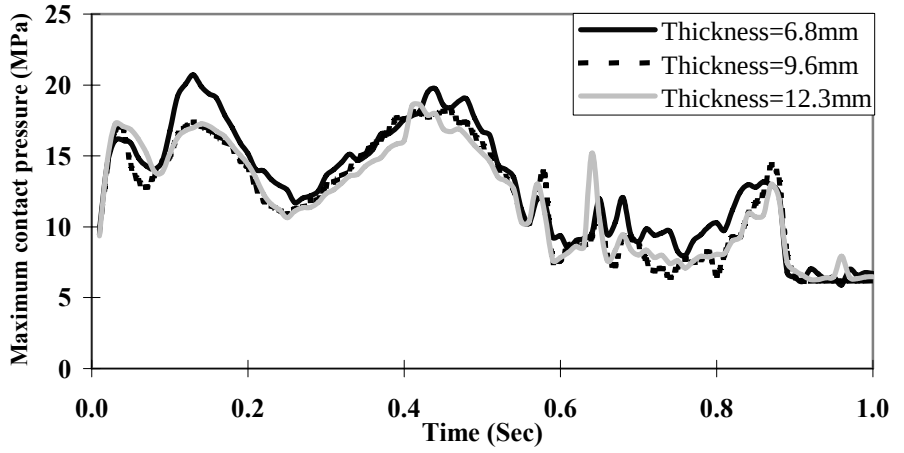

(a)

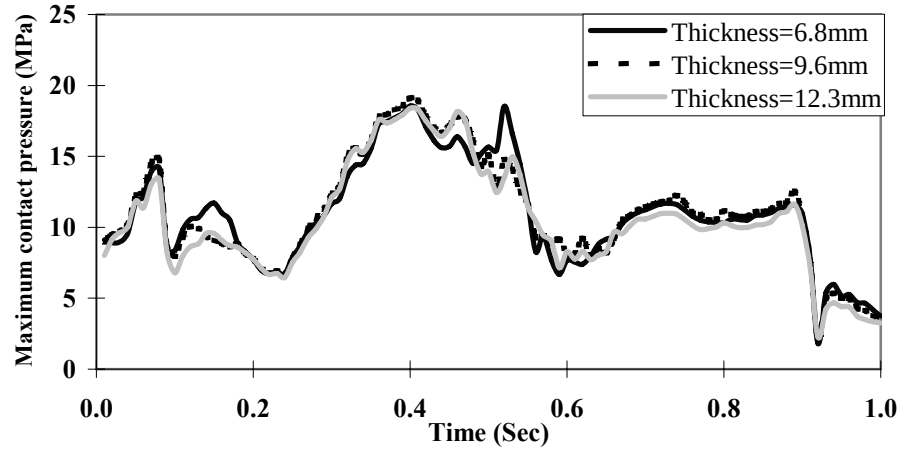

(b)

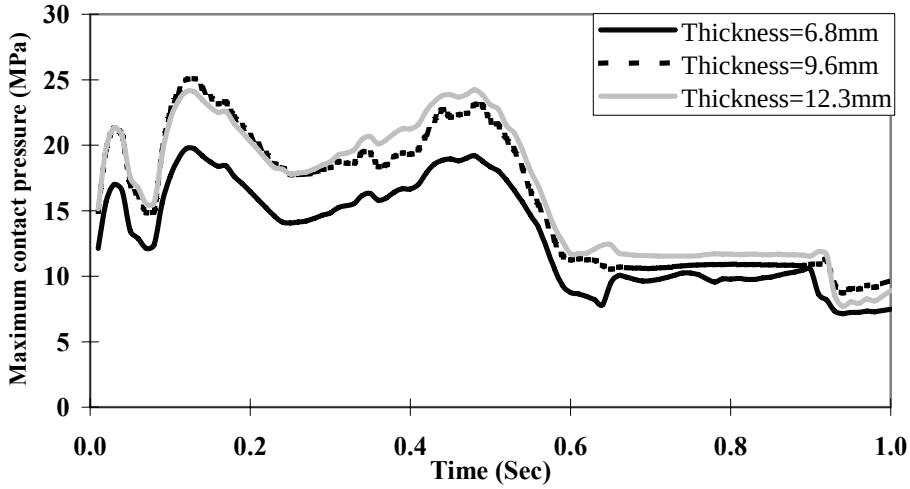

(c)

Figure 5-17 Influence of thickness of tibial bearing component on contact pressure on: (a) superior surface of fixed-bearing implant, (b) superior surface of mobile-bearing implant and (c) inferior surface of mobile-bearing implant

5.6 Discussion

This chapter compared the dynamic structural performance of fixed- and mobile-bearing implant.

In the dynamic analysis of total knee replacement, the tibio-femoral contact points were more scattered on the superior contact surface of the mobile-bearing implant compared to those of the fixed-bearing implant. The more scattered contact points in the mobile-bearing implant are the result of higher conformity in the contact area of tibio-femoral joint. The larger tibial tray IE rotation found in the mobile-bearing prosthesis will place greater functional demands on the ligaments. However, the relative motion between the superior and inferior contact surfaces in the mobile-bearing implant were found to be smaller than in the fixed-bearing implant. The lower friction distance will benefit the wear of the polyethylene.

Previous investigations on fixed-bearing total knee replacements concluded that polyethylene contact stress is inversely proportional to the contact area for a given load (Bartel *et al.* 1986). More conforming tibial components increase contact area and thus reduce contact stress. Sathasivam and Walker (1998) suggested that increased frontal plane conformity reduces subsurface stresses and potential for delamination. Clinical studies of retrievals also reported more severe types of wear in less conforming designs (Engh *et al.* 1992). However, fixed-bearing implants with increased conformity transfer excessive stress to the implant-bone interface and have been associated with loosening of the tibial component (Bryan and Rand, 1982, D'Lima *et al.* 2000). Mobile-bearing implants theoretically can increase conformity without transferring excessive stress to the implant-bone interface. From the results of this chapter, the maximum contact pressures in the fixed- and mobile-bearing implant were very close. Compared with the fixed-bearing implant, a larger contact area is shown in the mobile-bearing implant with a very small area subject to high contact pressures. This was due to the process of self-adjustment of conformity during rotation of the tibial bearing components. On the inferior surface of the mobile-

bearing implant, high contact pressure appeared in the insertion area, possibly due to stress concentration when the movement and forces were transferred between the tibial bearing component and the tibial tray. It is interesting to note that the contact pressure on the superior surface of the mobile-bearing implant was only two thirds that on the fixed-bearing implant during most of the stance phase of the gait cycle. Because most contact occurred during the stance phase with less relative rotation at the femoral component and tibial bearing component interface as shown in Figure 5-6, this should result in less wear on the superior surface of the mobile bearing implant. This may explains the findings by McEwen et al. (2005) and Jones et al. (1999); both papers reported that the mobile-bearing knee implant produced less wear than the fixed-bearing implant.

5.6.1 Influence of malalignment on performance of different implant

The influence of varus/valgus malalignment on motion and stress distribution in two kinds of knee implant were investigated. Varus/valgus malalignment influenced the rotation of the tibial components in the mobile-bearing implant significantly, the maximum rotation of the tibial tray increasing by 48.2% in condition of excessive valgus compared with light varus. The valgus condition will increase the demand on the ligaments. Also excessive varus/valgus increased the rotation of the tibial bearing component and resulted in higher contact pressure in the polyethylene during the swing phase. As for contact area, varus/valgus malalignment increased the difference in contact areas between the medial and lateral condyles in fixed-bearing implant, whereas, the maximum contact areas were approximately the same in the mobile-bearing implant because of its higher conformity.

5.6.2 Influence of thickness of tibial bearing component on stress distribution

The relationship between contact pressure and polyethylene tibial bearing component thickness in TKR was discussed in a few papers (Bartel *et al.* 1986,

Bei *et al.* 2004, El-Deen *et al.* 2006, Jin *et al.* 1995a, Petty *et al.* 1999). Early studies (Bartel *et al.* 1986) using static finite element and elasticity analyses with simplified knee implant geometry demonstrated that increasing the thickness of the polyethylene component would result in reduction in contact pressure and increase in contact area. Bartel *et al.* (1986) suggested a minimum polyethylene thickness of 6 mm to 8mm in a knee implant to reduce wear related problems. Plante-Bordeneuve and Freeman (1993) agreed that the polyethylene should be at least 6 mm thick. Jin *et al.* (1995a) used a general elastic elliptical contact theory for total knee replacement, considering the conditions of bonded and unbonded interface between the UHMWPE tibial bearing component and tibial tray. They concluded that the UHMWPE layer thickness can be optimized to minimize the contact stresses within the tibial bearing component. In another paper, Jin *et al.* (1995b) stated that the effect of the UHMWPE thickness is relatively small provided a sufficiently large value is chosen, and the conformity in the knee joint has a relatively large effect on the contact stress prediction. Bei *et al.* (2004) utilized multi-body dynamic analyses under in vivo functional conditions to quantify the relationship between contact pressures and tibial bearing component thickness. They found that contact pressures were good predictors of wear volume when the pressures varied by changing the applied load profile. El-Deen's static testing showed minimal increase in the lengths of contact imprints with increasing polyethylene component thickness (El-Deen *et al.* 2006). This increase was not statistically significant for polyethylene thickness of 10 mm compared with 12.5 and 15 mm. Petty *et al.* (1999) also stated that the contact pressure increased with the increase of thickness of the polyethylene component and became less sensitive to further increases in thickness.

The results in this chapter were consistent with conclusions from other people's research (Bei *et al.* 2004, El-Deen *et al.* 2006, Jin *et al.* 1995, Petty *et al.* 1999). Take the contact pressure at 0.15 second of gait cycle as an example, the contact pressures calculated in this chapter were compared with Jin's theoretical prediction (Jin *et al.* 1995a). At 0.15 second of gait cycle, the vertical load

reached its maximum value, 2570 N, the flexion angle was 16°, and the IE rotation of the tibial bearing component in both fixed- and mobile-bearing implant were almost 0°. In this case, the contact status was very close to the theoretical model's calculation requirements. Several factors were considered differently in the theoretical model and the FE model. In the theoretical model the UHMWPE was assumed to be a linear elastic material, ideal vertical load was applied and friction was neglected. In the FE model the UHMWPE was modelled as a non-linear material, AP motion occurred at 0.15 second of the gait cycle and friction was considered. The FE predicted maximum contact pressures were, however, in very good agreement with theoretical results in the fixed- and mobile-bearing implant. In fixed-bearing implant, the theoretical prediction of maximum contact pressure was 18.94 MPa for 6.8 mm thick design, 15.95 MPa for 9.6 mm and 12.3 mm design; the maximum contact pressure in the FE model was 19.39 MPa for 6.8 mm design, 17.11 MPa for 9.6 mm and 12.3 mm design. In the mobile-bearing implant, the theoretical prediction of maximum contact pressure was 12.82 MPa for 6.8 mm thick design, 11.2 MPa for 9.6 mm and 12.3 mm design; the maximum contact pressure in the FE model was 11.71 MPa for 6.8 mm design, 9.12 MPa for 9.6 mm and 12.3 mm design. It is also note that the maximum contact pressure in the mobile-bearing implant was less than that in the fixed-bearing implant in all thickness designs, which is consistent with the findings of Jin et al. (1995a), because the interface between tibial bearing component and tibial tray was bonded in fixed-bearing implant and unbonded in mobile-bearing implant.

Although the same trend was found in the relationship between maximum contact pressure and UHMWPE thickness (Jin *et al.* 1995a, Bei *et al.* 2004), the FE model in this thesis gives more accurate contact pressure values with reference to published experimental data (Godest *et al.* 2002, Halloran *et al.* 2005). For example, Bei *et al.* (2004), who used a linear elastic UHMWPE model, find the maximum contact pressure in the 6.8 mm thick fixed-bearing implant at 0.15 second of gait cycle was 35 MPa compared to 19.39 MPa in this

paper and 17.5 MPa in Halloran's paper. The maximum contact pressure was about 75% higher in the linear UHMWPE model than in the non-linear model.

Under the effect of gait cycle load, the fixed- and mobile-bearing implants reacted differently with increase of UHMPWE thickness. It can be seen from Figure 5-17 that the peak contact pressures occurred at different phases of the gait cycle. In the fixed-bearing implant, the contact pressure decreased when the thickness of the tibial bearing component increased from 6.8 mm to 9.6 mm; however, no further decrease of contact pressure was found when the thickness was increased to 12.3 mm. In the mobile-bearing implant, different trends were found on the variation of contact pressure with the change of thickness of tibial bearing component. As the thickness of the tibial bearing component increased, the contact pressures on the superior surface remained almost the same; the contact pressures on the inferior surface, however, increased with an increase in thickness to 9.6 mm and 12.3 mm. The different reaction to the increase of UHMWPE thickness in the mobile-bearing implant could be explained by the self-adjustment of the mobile-bearing implant due to the additional motion between the tibial bearing component and tibial tray.

Comparing the maximum contact pressure during gait cycle in the fixed- and mobile-bearing implant with different UHMWPE thickness designs, the 9.6 mm thick design in the fixed-bearing implant and the 6.8 mm thick design in the mobile-bearing implant are suggested because lower maximum contact pressure and less bone to be removed. However, the selection of thickness of tibial bearing component during TKR operation also depends on the bone and ligament status of the patient. Comparing to the 9.6 mm and 12.3 mm thick design of the fixed-bearing implant, Figure 5-17 a shows that higher maximum contact pressure in the 6.8 mm design were mainly occurred during 0.08 and 0.26 second of the gait cycle, the maximum contact pressure were close in three thickness designs during the rest of gait cycle. As stated by Jin *et al.* (1995b), the effect of UHMWPE thickness on contact pressure was small provided a sufficient value was chose, tibio-femoral conformity can be changed to reduce the contact pressure. The 3 MPa higher contact pressure in the 6.8 mm thick

design during early stance phase can be reduced by slightly increasing tibio-femoral conformity.

5.7 Conclusions

This research provides a new method for conducting structural analysis of the total knee replacement during the gait cycle. The research used MSC/ADAMS to obtain the movement of the total knee implant and MSC/MARC to generate the contact area and pressure in the implant components. The models were successfully completed, and results were obtained which were in agreement with other researchers' findings.

This research only studied the pressure and movement in the total knee replacement; the wear of the implant is not within the scope of this research. In the mobile-bearing implant, more contact area was found on the superior surface of the tibial bearing component. It is interesting to note that the maximum contact pressures on the tibial bearing components in the fixed- and mobile-bearing implant were nearly the same. However, the contact pressure on the superior surface of the mobile-bearing implant was only two thirds that on the fixed-bearing implant during most of the stance phase of the gait cycle, with most contact occurring during the stance phase and less movement between the femoral component and tibial bearing component, this should result in less wear on the superior surface of the mobile-bearing implant.

In this chapter, after comparing the maximum contact pressure with different thicknesses of tibial bearing component, it can be concluded that the thickest tibial bearing component was not the best. In the mobile-bearing implant, a tibial bearing component of 6.8 mm thickness resulted in less contact pressure on the inferior surface. In the fixed-bearing implant, there was no obvious decrease in contact pressure when the thickness of the tibial bearing component was increased from 9.6 mm to 12.3 mm. Based on the research in this chapter, the design with a 9.6 mm tibial bearing component was best for the fixed-bearing implant, and 6.8 mm for the mobile-bearing implant.

Chapter 6

Dynamic analysis of implanted knee joint with bone

6.1 Introduction

Aseptic loosening of prosthetic components has remained one major cause of failure after TKR (Ferhring and Mcavoy 1996, Vince 2003). At revision of femoral components, inadequate bone stock is often apparent and radiological studies have also shown distal femoral bone resorption, particularly behind the anterior flange (Mintzer *et al.* 1990). Animal experiments have also indicated that considerable bone remodelling may take place in the distal femur (Bobyn *et al.* 1982). Mintzer *et al*. (1990) found roentgenographically stress shielding in the anterior distal femur in 68% of patients with TKR. The bone loss was found to be independent of fixation mode (cemented/uncemented) and implant design. Petersen *et al.* (1995) reported changes in bone mineral density (BMD) in the distal femur following uncemented porous-coated total knee arthroplasty. They found stress shielding anteriorly in the distal femur occurred in all patients examined 2 years after surgery. Van Lenthe *et al.* (1997) used a three-dimensional finite-element model of an average male femur with cemented femoral knee component to investigate gradual changes in bone density after TKR. The long-term bone loss under the femoral knee component resembled clinical findings which confirms the hypothesis that stress shielding can cause distal femoral bone loss.

The short- and long-term behaviour of a total knee joint replacement is dependent on obtaining the optimal stress distribution within the bone-implant construct. The stress distribution within the prosthetic components, the bone-implant interfaces and the supporting bone is ultimately dependent on the kinematics of the replaced knee. In other words, joint kinematics and contact mechanics influence the success of current total knee replacement devices.

Computer models present an effective way of evaluating these characteristics during the design phase and provide indication of expected clinical performance.

A number of computational models have been developed to study natural and prosthetic knee mechanics. Moeinzadeh and his co-authors created a two-dimensional dynamic model of the knee, including ligament resistance and specified a force and moment on the femur (Moeinzadeh *et al.* 1983). Blankevoort and Huiskes (1996) and Mommersteeg *et al.* (1996) developed and experimentally verified a three-dimensional knee model with its surrounding soft tissue. In order to produce a more realistic model, Sathasivam and Walker (1997) developed a rigid body analysis of TKR that reproduced motions found using the Stanmore knee simulator. Piazza and Delp (2001) created a rigid body, dynamic model of a TKR performing a step-up task with both patterns of muscle activity and the kinematics of the hip used as inputs to the simulation. The model included both tibio-femoral and patello-femoral articulations and predicted the flexion-extension pattern of the step-up activity. In their paper, Godest *et al.* (2002) used an explicit finite element approach to simulate both the kinematics and the internal stresses in knee implants during a gait cycle. Halloran *et al.* (2005) developed an explicit FE TKR model that incorporated tibio-femoral and patello-femoral articulations.

In all of these investigators' dynamic models, attention was paid to tibio-femoral contact mechanics (Blankevoort and Huiskes 1996, Mommersteeg *et al.* 1996, Sathasivam and Walker 1997). Only Godest *et al*. (2002) used a dynamic model to study the stress in the polyethylene bearing.

Halloran *et al*. (2005) included bone and ligament in their models. They used softened contact technology to simulate tibio-femoral contact, but bone structures were modelled as rigid bodies. In van Lenthe's research (van Lenthe *et al.* 1997), the distal femur was modelled as a flexible body using finite element analysis. However, only three load cases of a normal daily loading cycle were applied. The stress distribution in the distal femur during daily activities has not yet been investigated.

In this chapter, a dynamic model of an implanted knee joint was developed to simulate the motion of the knee joint after TKR. The stress distribution in the distal femur during a gait cycle was also simulated.

6.2 Description of the model

6.2.1 Dynamic model

A knee joint model with cemented total knee prosthesis was developed in MSC/ADAMS software (Figure 6-1). This model consists of anatomically correct bone models of the femur, tibia, fibula and patella. The ligaments have been added in their anatomically correct location and the knee prosthesis has been inserted with care to ensure satisfactory alignment. The distal part of the femur has been modelled as a flexible body, which was imported from MSC/MARC software. A modal neutral file representing the flexible component was generated in MARC and then integrated into the ADAMS model. In the modal neutral file, multipoint constraints were defined between nodes on the flexible component and interface nodes which link to the rigid body. Through interface nodes, the flexible component can be connected to the rest of ADAMS model. The stress distribution in the distal femur was then investigated using both software packages. Having completed the design of an appropriate model, the changes in stress at specific nodes during the gait cycle could be plotted. Two pairs of surface contacts were defined: the contact between the femoral and tibial implants and the contact between the femoral and patella implants. Springs were used to simulate the ligaments, which are positioned at average insertion points. The stiffness of the posterior cruciate ligament, the medial collateral ligaments, the lateral collateral ligaments and the patella tendon were taken as 150 N/mm, 72 N/mm, 61 N/mm and 200 N/mm respectively (Beillas *et al.* 2004). The geometries of the lower limb bone structure were obtained from the International Society of Biomechanics web resources (ANON. 2002).

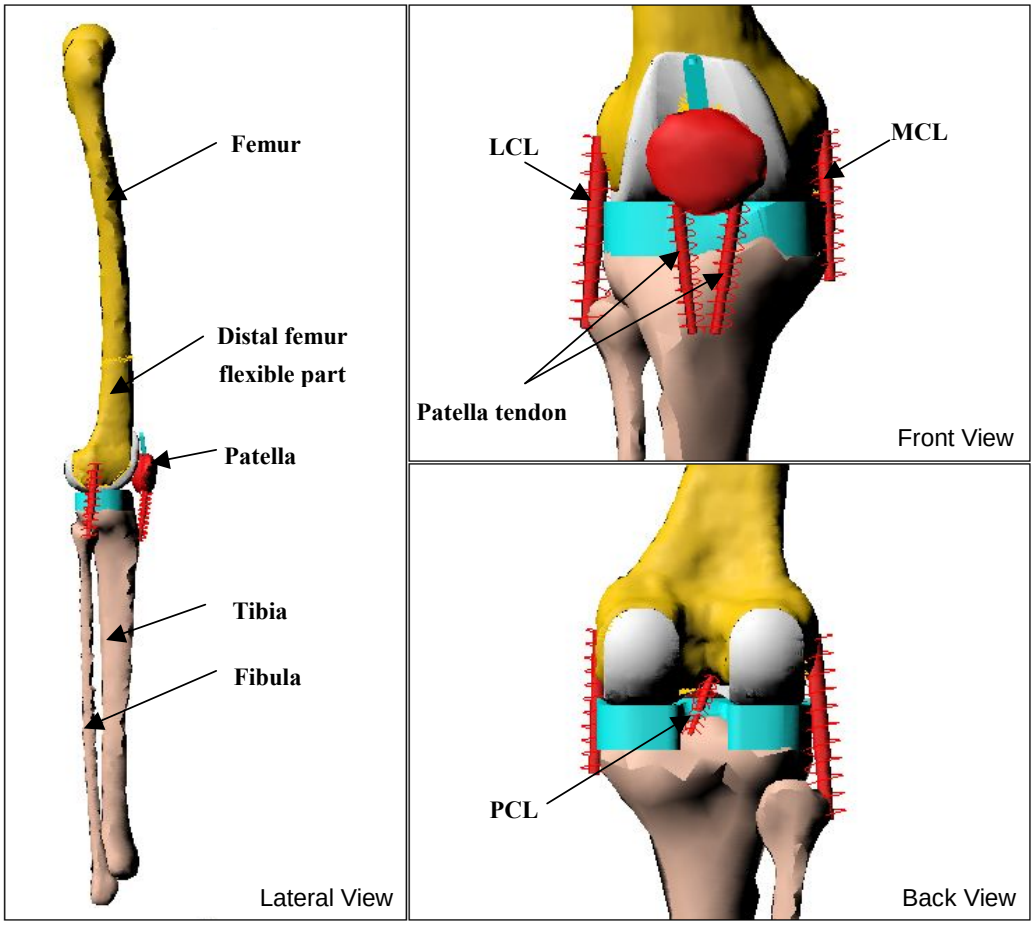

Figure 6-1 Dynamic model of knee joint after total knee replacement

Boundary conditions are applied to reproduce the Purdue knee simulator environments. The Purdue simulator applies a vertical load and a flexion angle at a simulated hip and controls the horizontal anterior-posterior and medial-lateral ankle translation. Rotation of the ankle in all directions is allowed. A quadriceps force balances the vertical load through the patella ligament. The inputs to this model include: vertical axial load on hip, quadriceps force, tibio-femoral anterior-posterior translation, anterior-posterior and medial-lateral ankle translation. We used the load data in Figure 6-2 which was adopted from published work (Bergmann *et al.* 2001, Halloran *et al.* 2005, Winter 1990).

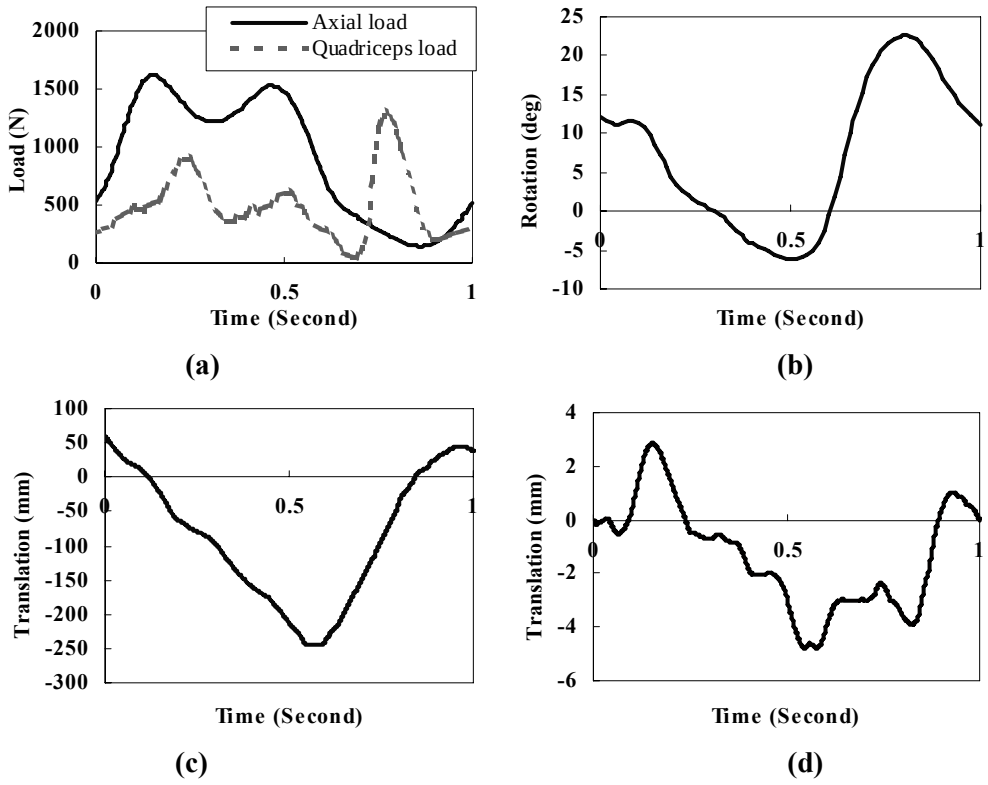

Figure 6-2 Load applied on dynamic model of knee joint: (a) Axial load and quadriceps load, (b) hip flexion, (c) ankle anterior(+)/posterior(-) translation and (d) ankle lateral(+)/medial(-) translation.

6.2.2 Finite element model

The finite element model of the distal femur was developed in MSC/MARC software (Figure 6-3). The FE model was imported into the dynamic model as outlined in the previous section. The load transferred to the distal femur during the dynamic simulation was exported to the FE model making it possible for the stress distribution at any given time to be calculated using finite element analysis.

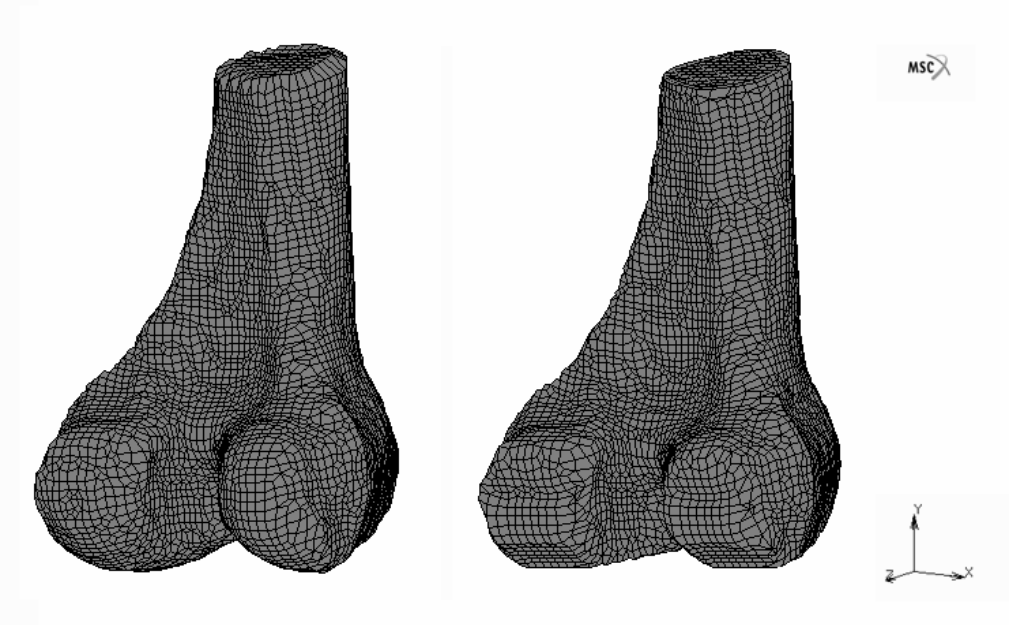

Figure 6-3 3D finite element model of intact distal femur and cut distal femur

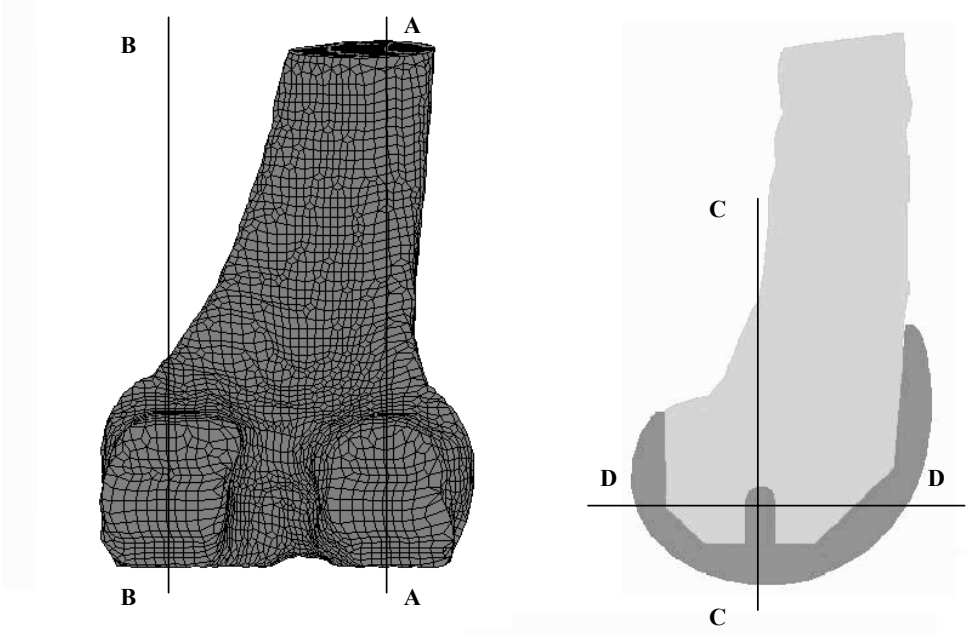

Figure 6-4 Definition of different cross sections. A-A: Sagittal cross section cutting through centre of lateral peg, B-B: Sagittal cross section cutting through centre of medial peg, C-C: Frontal cross section cutting through centre of peg, D-D: Transverse cross section cutting through centre of peg

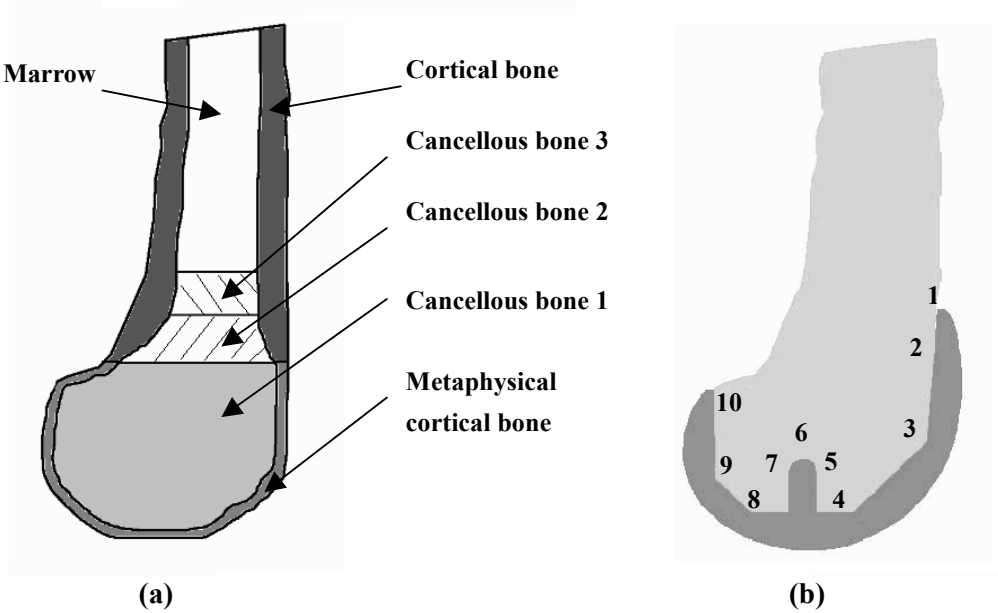

Figure 6-5 Bone structure. (a) Material distribution on cross section A-A of intact distal femur, (b) Distal femoral zones defined adjacent to the prosthesis for stress study.

Figure 6-4 defined four sections of distal femur. Cross sections A-A and B-B are lateral and medial sagittal sections cutting through the centre of the femoral peg. Section C-C and section D-D are frontal and transverse section cutting through the centre of the femoral peg.

For the FE model of the distal femur, the material properties of the cancellous bone and cortical bone shown in Figure 6-5 are listed in Table 6-1. In the FE model, the material properties of the distal femur were divided into several areas according to the CT density distribution (Figure 6-5). The Young's modulus (E) of each area was calculated from the average density (ρ) of that area (van Lenthe *et al*. 1997):

$$E=3790\rho^3 \text{ MPa} \qquad \textbf{(6-1)}$$

The apparent density ρ was calculated from the CT density value. Van Lenthe *et al.* (1997) stated that there was high linear correlation between the CT value and apparent density. The maximum apparent density in the FE model was normalised at 1.73 g/cm^3. Poisson's ratio for all bone elements was assumed to be 0.3. Cement material was assigned to the elements attached to the

cut surface of the distal femur. The material properties of cement are also listed in Table 6-1. Figure 6-5a shows the material distribution on the cross section A-A. Figure 6-5b defines the different zones of the distal femur adjacent to the prosthesis for stress study. At the lateral side, zone 1 to zone 10 are defined as L1 to L10; at the medial side, zone 3 to zone 10 are defined as M3 to M10. M1 and M2 do not exist because of asymmetry of the bone.

A finite element model of the intact bone, which was cut to replicate the postoperative bone, was developed in MSC/MARC. The same loads in the implanted knee model were applied to the intact bone and the stress distributions in the implanted bone and intact bone were compared.

Table 6-1 Material properties of different parts of distal femur (Au *et al.* 2005, Galik 2002)

Material	Elastic modulus E (MPa)	Poisson's ratio ν	Density ρ (g/cm^3)
Cortical bone	17962	0.3	1.73
Metaphyseal cortical bone	7500	0.3	1.25
Cancellous bone 1	1091	0.3	0.66
Cancellous bone 2	400	0.3	0.3
Cancellous bone 3	100	0.3	0.2
Bone cement (PMMA)	2100	0.4	1.19

6.3 Results

6.3.1 Variation of stress in distal femur during gait cycle

Using gait analysis data, a gait cycle was simulated with the dynamic model in MSC/ADAMS. The simulations were performed over 1 second with a frequency of 1 Hz, i.e. one gait cycle. The maximum time step was 0.001 second during the simulation. Figure 6-6 shows the variation of tibio-femoral contact force. The tibio-femoral contact force curve shows two characteristic peak values during the gait cycle. The hip axial force referenced from Bergmann's (2001) research was 2.38 times body weight (700 N), resulting in a peak value in knee

contact force of 2.9 times body weight. This is in the range of Taylor's test results (Taylor *et al.* 2004) where the average tibio-femoral contact force was 3.1 times body weight with a range from 2.75 to 3.79 times body weight. As stated in Chapter 5, during normal gait, except for the occurrence of a brief valgus moment after initial contact, the knee joint is subjected to an external varus moment throughout the stance phase. Figure 6-6 also shows high contact force on the medial side during the stance phase corresponding to the varus moment on the knee joint. Figure 6-7 shows the patello-femoral motion in the model. It is consistent with Halloran's results (Halloran *et al.* 2005), the peak values of patello-femoral motion occurring during the swing phase. The predicted peak value of inferior-superior motion was 29 mm which is slightly higher than Halloran's experimental results of 25 mm; however, the peak value of anterior-posterior motion of 13 mm is the same as Halloran's result. The slightly different value of the peak patello-femoral motion found with this model and Halloran's may be caused by a slight difference in geometry between the modelled knee joints. Figure 6-8 shows the variation of von Mises stress at different zones of the femur of an implanted knee during a gait cycle. Figure 6-8a and Figure 6-8b are the stress variation at zones on the lateral sagittal section A-A; Figure 6-8c shows the stress variation at zones on the medial sagittal section B-B. Because cortical bone is defined in zone 1, the stress in zone 1 is much higher than in other zones. Figure 6-8 shows lowest stress levels in zones 4 and 8 of both sides, which are the most distal corners of the connection between femur and prosthesis.

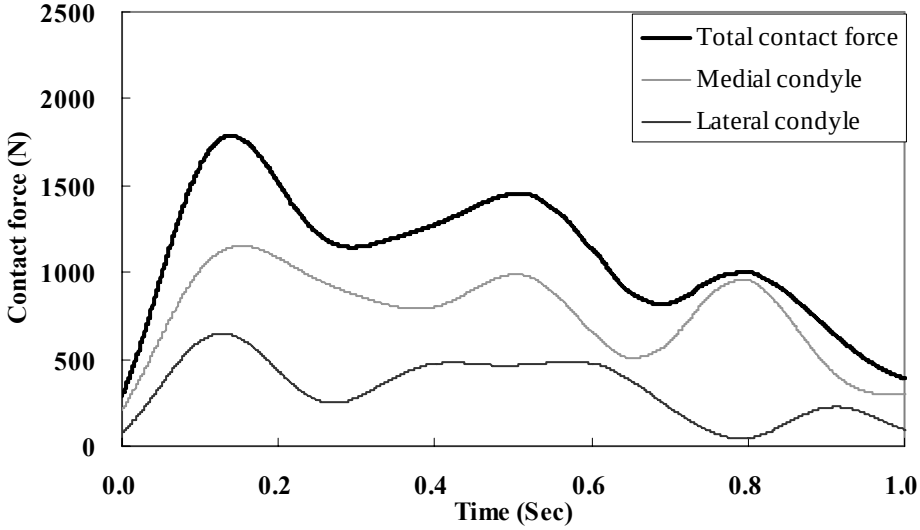

Figure 6-6 Tibio-femoral contact force resulting from dynamic model of implanted knee joint

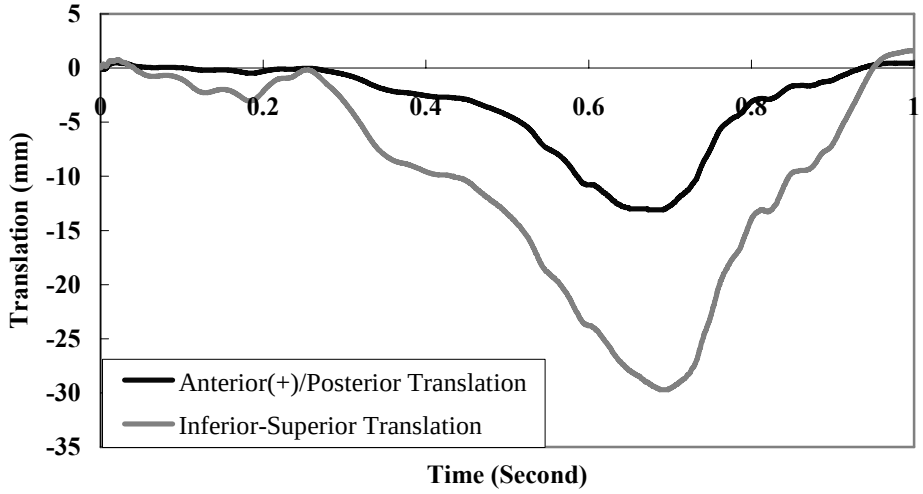

Figure 6-7 Patello-femoral translation resulting from dynamic model of implanted knee joint

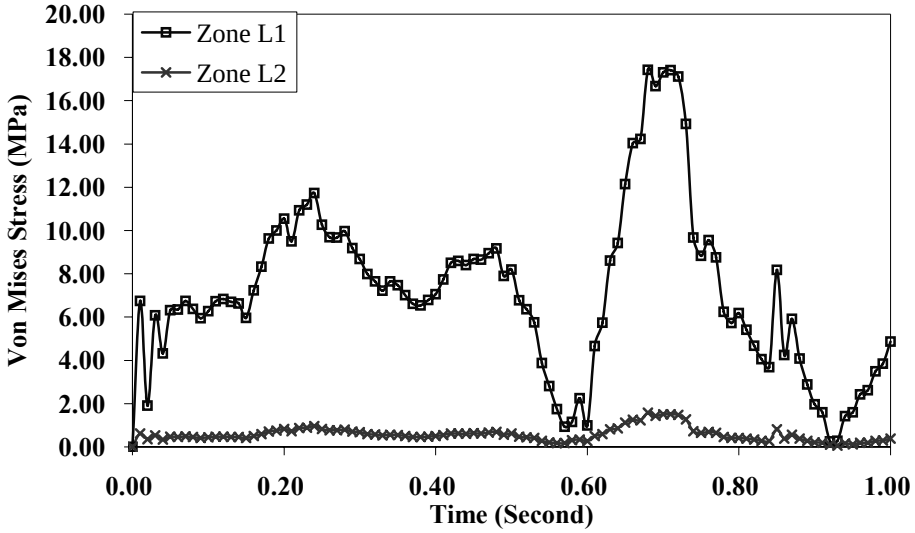
Zone L1
Zone L2
Von Mises Stress (MPa)
20.00
18.00
16.00
14.00
12.00
10.00
8.00
6.00
4.00
2.00
0.00
0.00
0.20
0.40
0.60
0.80
1.00
Time (Second)

(a)

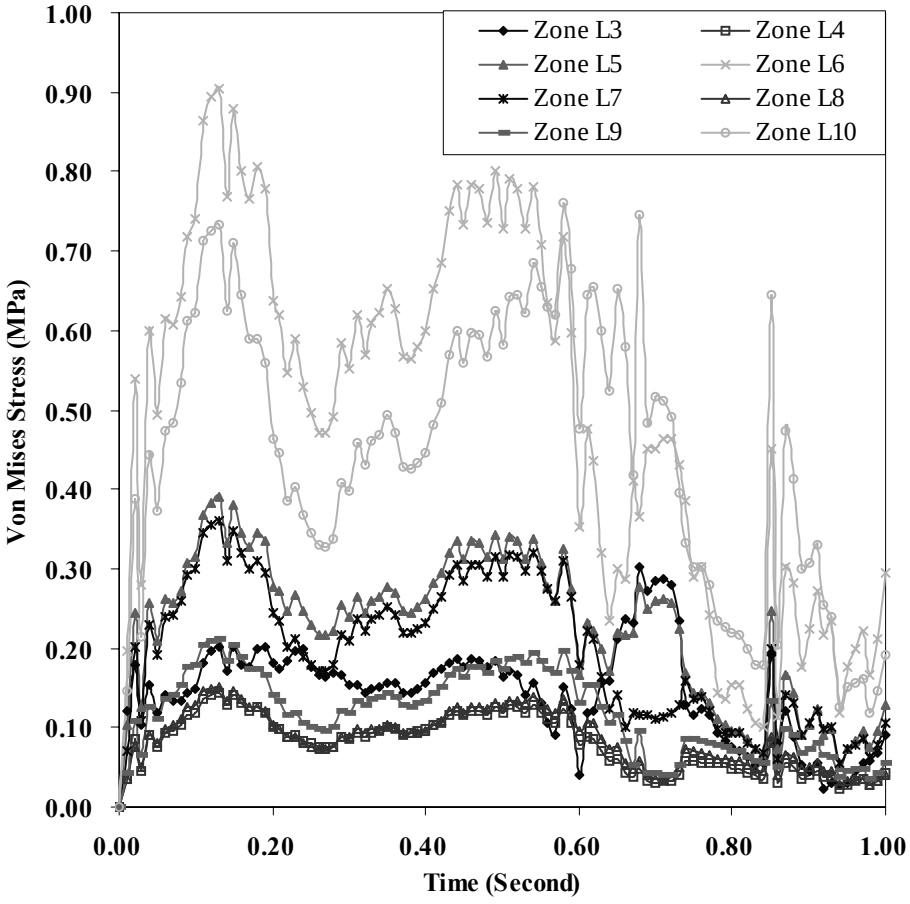
Zone L3
Zone L4
Zone L5
Zone L6
Zone L7
Zone L8
Zone L9
Zone L10
Von Mises Stress (MPa)
1.00
0.90
0.80
0.70
0.60
0.50
0.40
0.30
0.20
0.10
0.00
0.00
0.20
0.40
0.60
0.80
1.00
Time (Second)

(b)

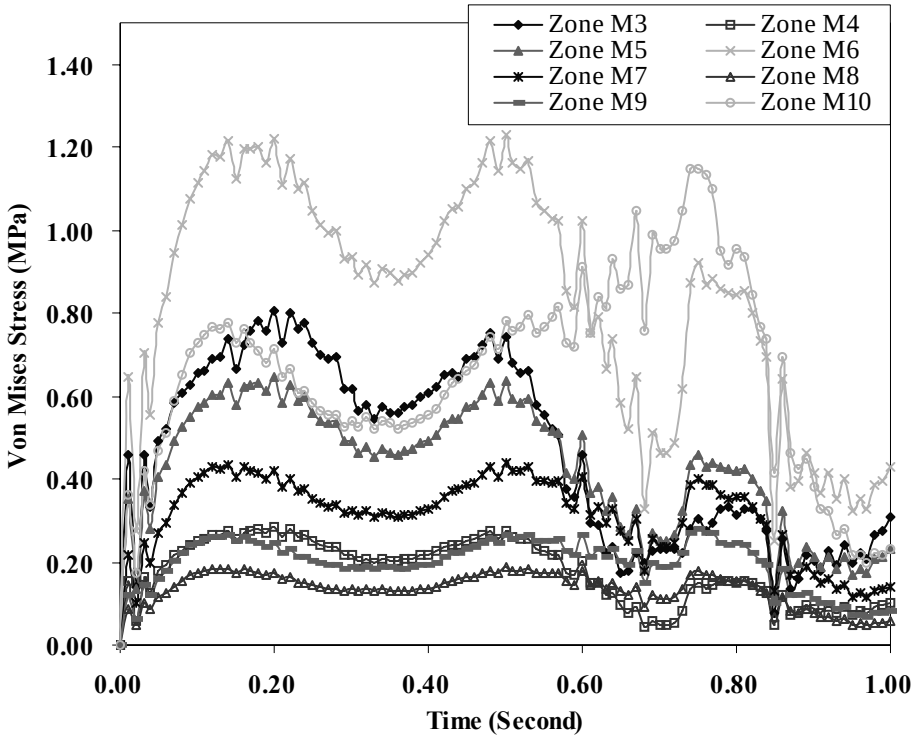

(c)

Figure 6-8 Variation of von Mises stress at different zones in the implanted femur during gait cycle: (a) and (b) lateral side, (c) medial side

6.3.2 Stress distribution in distal femur

At zones L1 and L2, high stress levels appear at around 0.7 second. High stress levels appear at around 0.15 and 0.5 second at zones L3 to L10 and M3 to M10. The loads on the flexible distal femur at the times of 0.15, 0.5 and 0.7 second were exported to MSC/MARC. The stress distributions in the distal femur on four sections, which are defined in Figure 6-4, are displayed in Figure 6-9 to Figure 6-12.

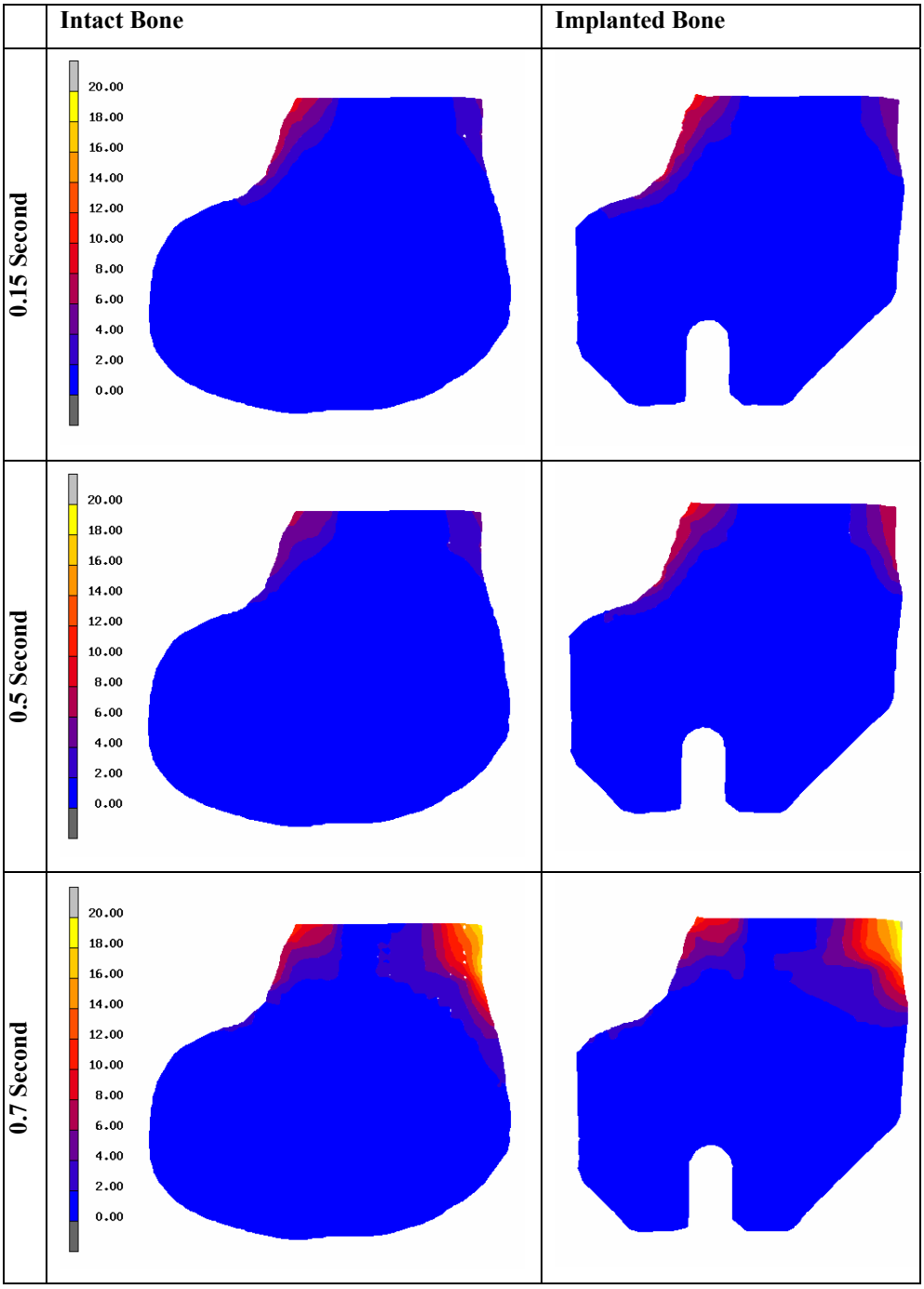

Figure 6-9 Von Mises stress (MPa) distribution in intact bone and implanted bone on lateral sagittal section A-A at different stages of gait cycle

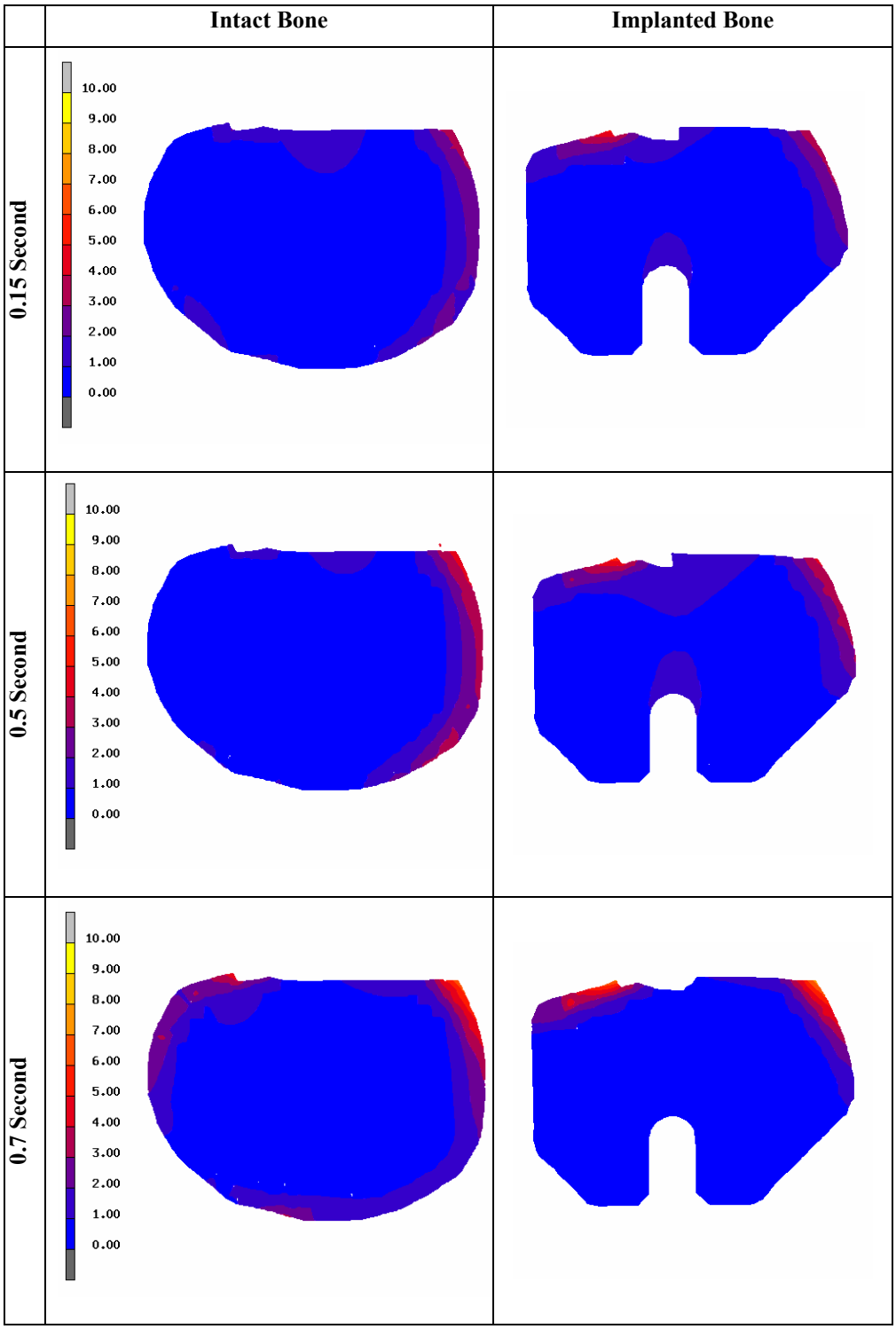

Figure 6-10 Von Mises stress (MPa) distribution in intact bone and implanted bone on medial sagittal section B-B at different stages of gait cycle

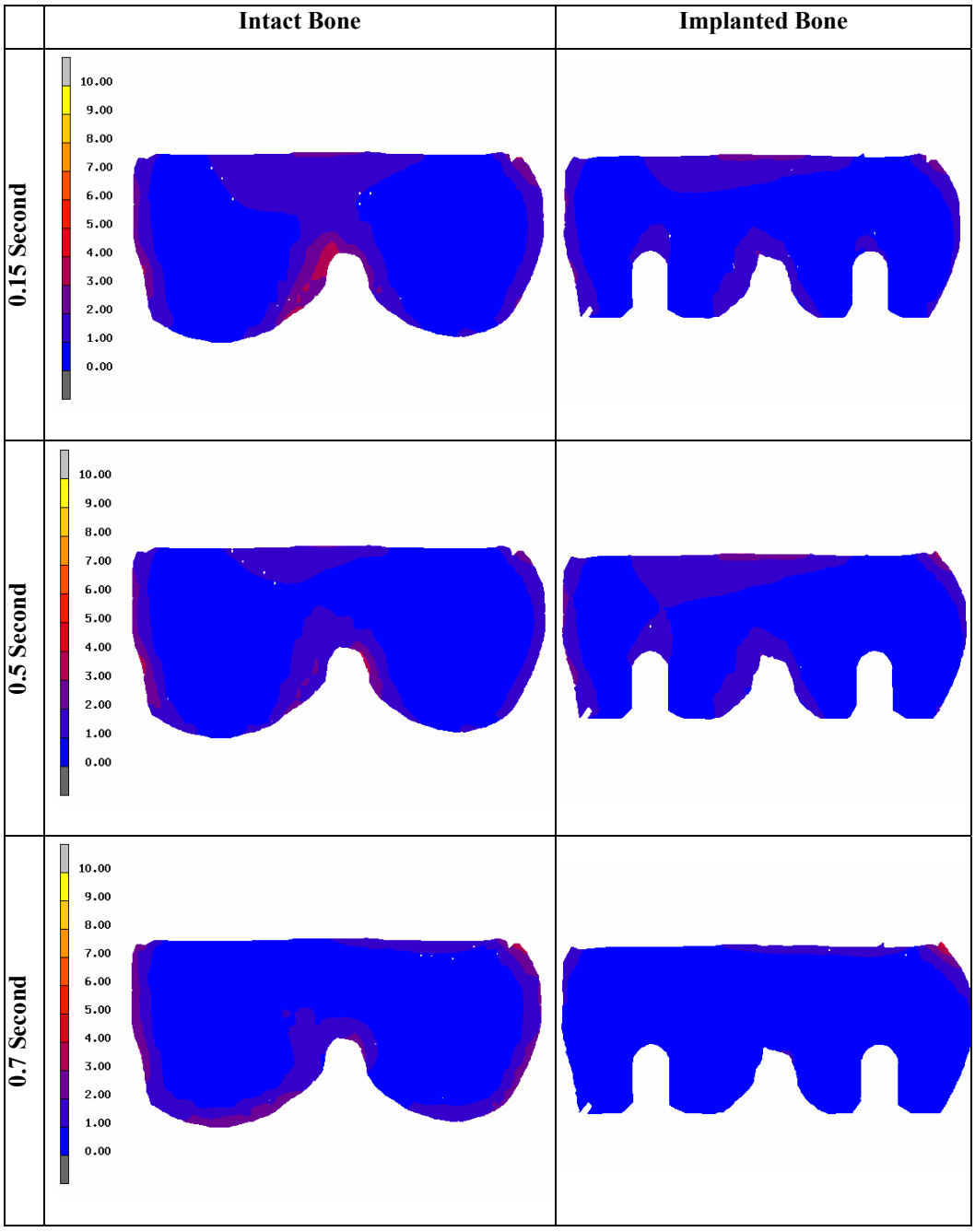

Figure 6-11 Von Mises stress (MPa) distribution in intact bone and implanted bone on frontal section C-C at different stages of gait cycle

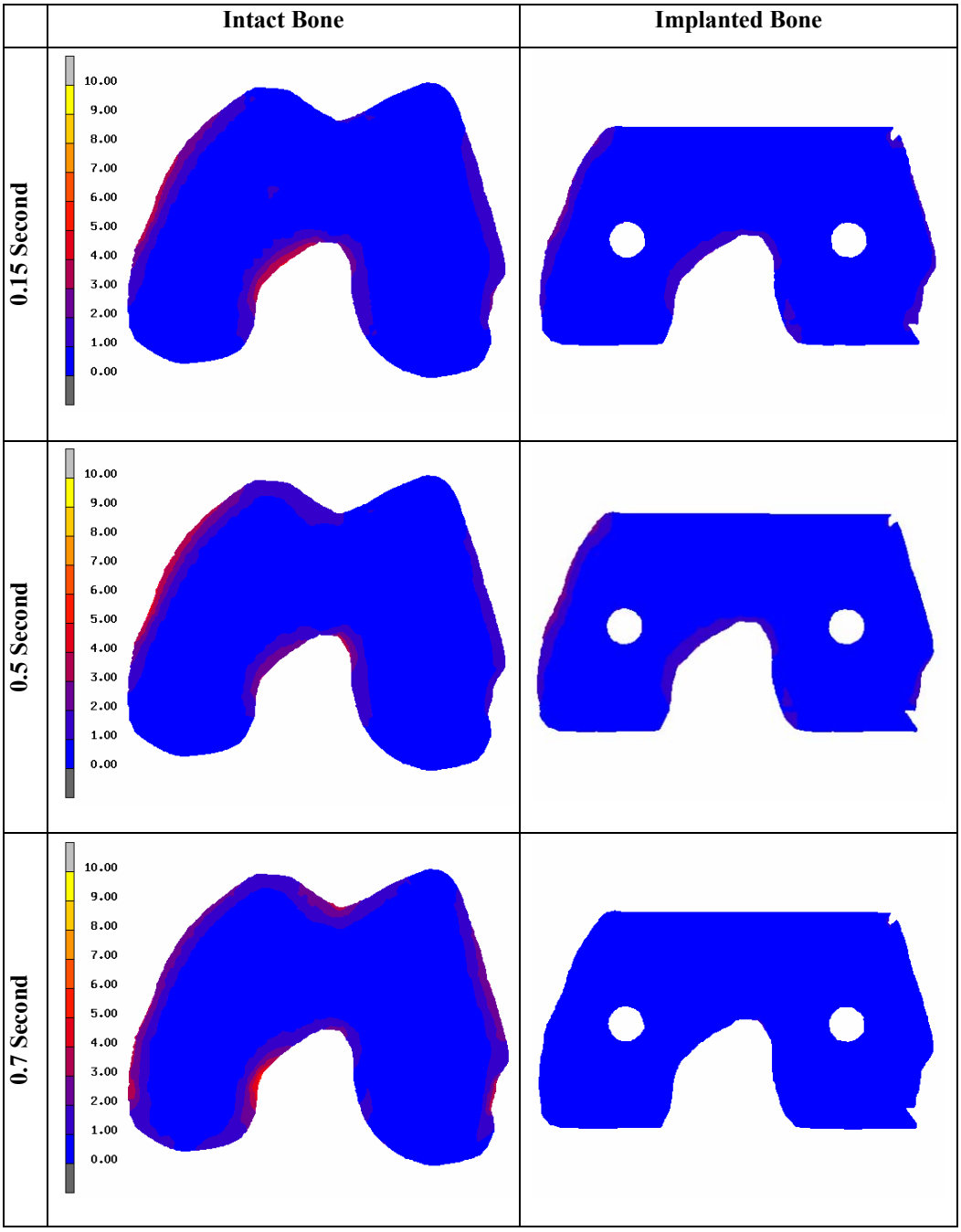

Figure 6-12 Von Mises stress (MPa) distribution in intact bone and implanted bone on transverse section D-D at different stages of gait cycle

Figure 6-9 is the stress distribution on the sagittal section through the lateral peg centre (A-A). Figure 6-9 demonstrates high gradients of stress values at zone L1 to zone L2. Figure 6-10 to Figure 6-12 are the stress distributions on the sagittal, frontal and transverse sections through the medial peg centre (B-B, C-C and D-D). Lower stresses appear at zones L/M4 and L/M8; however, the stresses at

zones L1 and L2 are higher in the implanted distal femur. Figure 6-10 and Figure 6-11 show a decrease in stress at the distal end of the femur after total knee replacement in all investigated load cases. It is also observed from Figure 6-10 and Figure 6-11 that the stresses in the distal femur next to the peg are relatively higher than those in the surrounding bone. Figure 6-12 shows higher stress at the centre of the anterior distal region adjacent to the patellar surface at 0.5 second and 0.7 second.

Figure 6-13 shows a comparison of the values of von Mises stress at different zones (defined in Figure 6-5) of the lateral and medial side at three stages of the gait cycle. Figure 6-13 presents the same information as Figure 6-9 and Figure 6-10 in chart format. This gives numerical values of the difference between stresses at different areas in intact and implanted distal femur. Figure 6-14 presents the strain energy density at different zones of lateral and medial side at three stages of a gait cycle. It shows the same shape as the previous figure on stress distribution. To predict the bone remodelling around the prosthesis, the rate of bone mass change in each zone of the distal femur after TKR were calculated (Figure 6-15). The strain energy densities at all the zones at 0.15, 0.5 and 0.7 second of the gait cycle are used to calculate the rate of bone mass change. The same density was used for the three load stages during the gait cycle. The site specific bone remodelling theory stated in section 2.4.3.2 was used. In equation (2-4), dead zone threshold s was 0.75, free surface A in unit volum cancellous bone (mm^3) was 32.5 mm^2, constant τ was 2.5 $g^2mm^{-2}J^{-1}$. Figure 6-15 shows the rate of bone mass change per unit volume (mm^3) at zone 2 to zone 10 in the distal femur after TKR. The strain energy density increased at zone 1. However, the bone density at zone 1 reached the upper bound of bone density, 1.73 g/cm^3, therefore bone remodelling did not happen at zone 1. The zone 1 was not displayed in Figure 6-15. It's found that bone density at zones L/M4, L/M8 and L/M9 decreased.

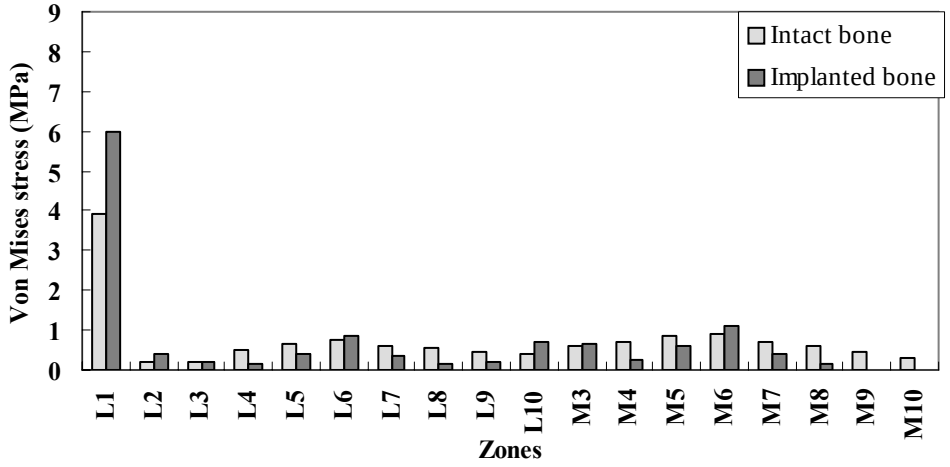

(a)

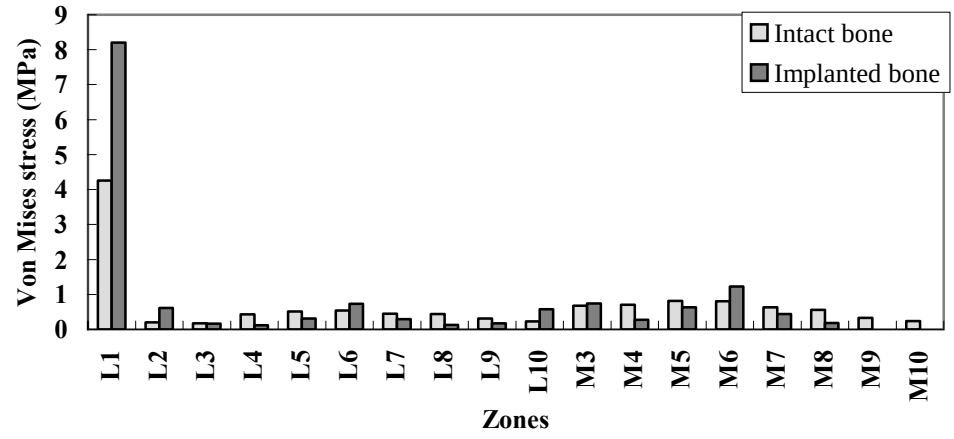

(b)

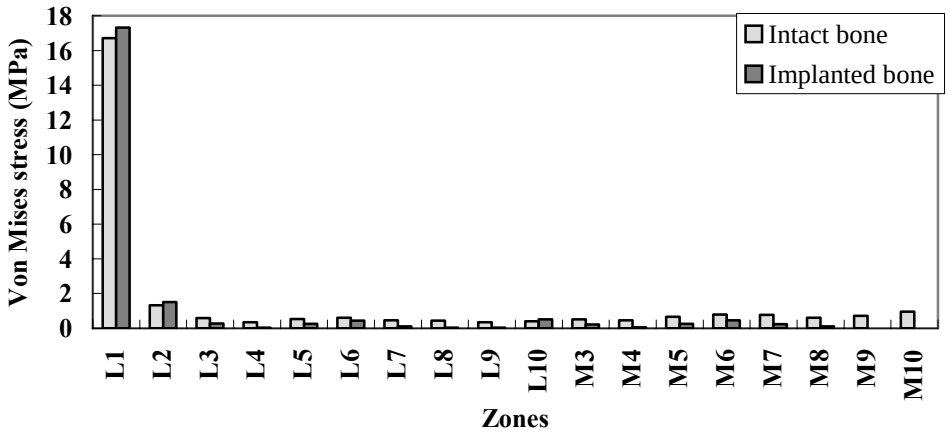

(c)

Figure 6-13 Von Mises stress on lateral and medial side of intact femur and implanted femur at: (a) 0.15 second, (b) 0.5 second and (c) 0.7 second of gait cycle

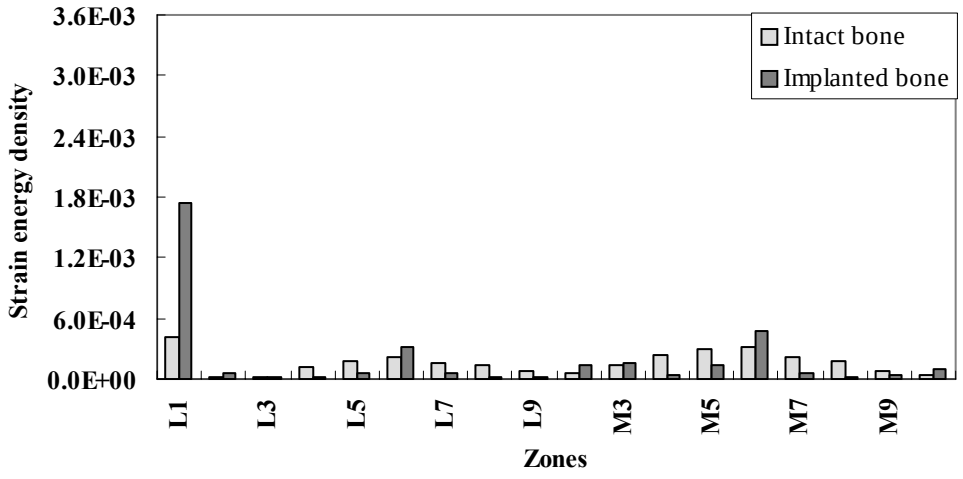

(a)

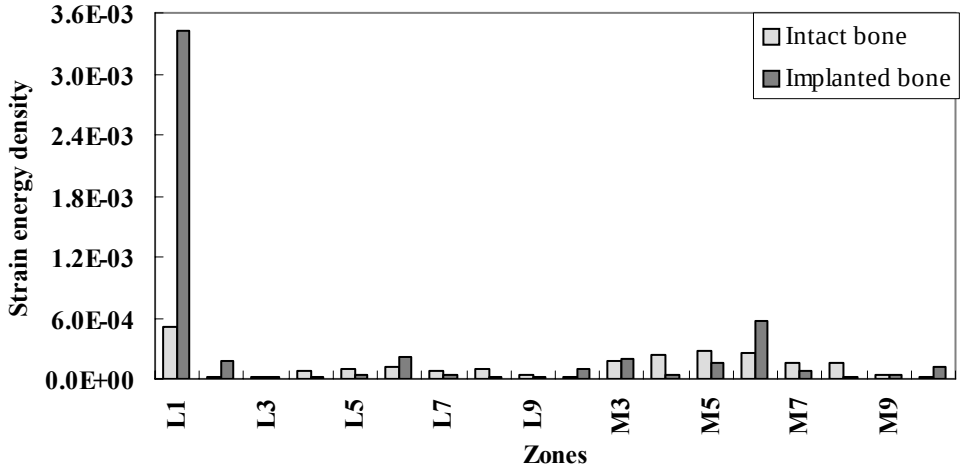

(b)

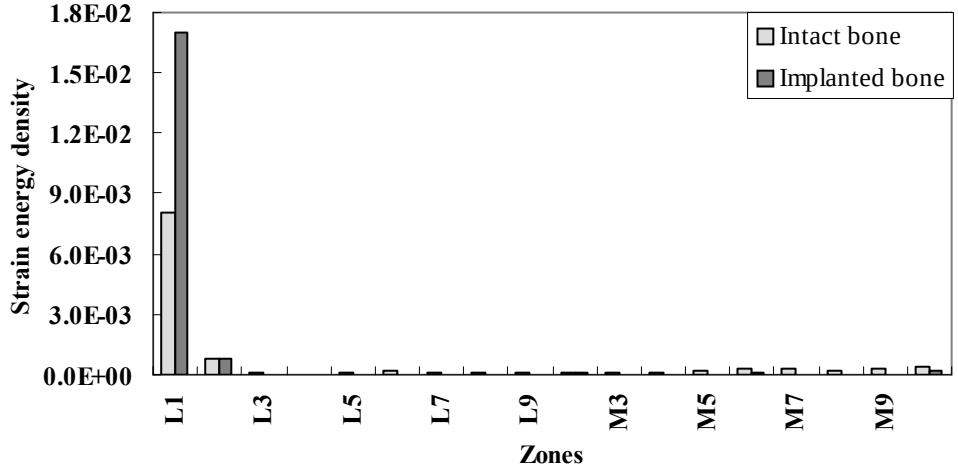

(c)

Figure 6-14 Strain energy density (10^{-3}J·mm^{-3}) on lateral and medial side of intact and implanted femur at: (a) 0.15 second, (b) 0.5 second and (c) 0.75 second of gait

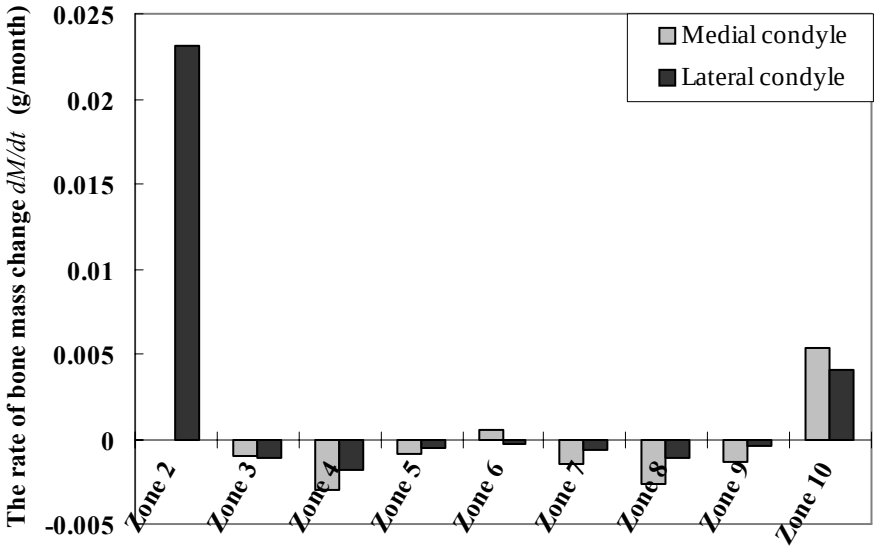

Figure 6-15 The rate of bone mass change per unit volume (mm^3) in distal femur after TKR

6.4 Influence of malalignment on tibio-femoral contact force

In order to investigate the influence of the varus/valgus malalignment on tibio-femoral contact force and stress distribution in the distal femur after TKR, the tibia and fibula were rotated 5° towards the medial/lateral.

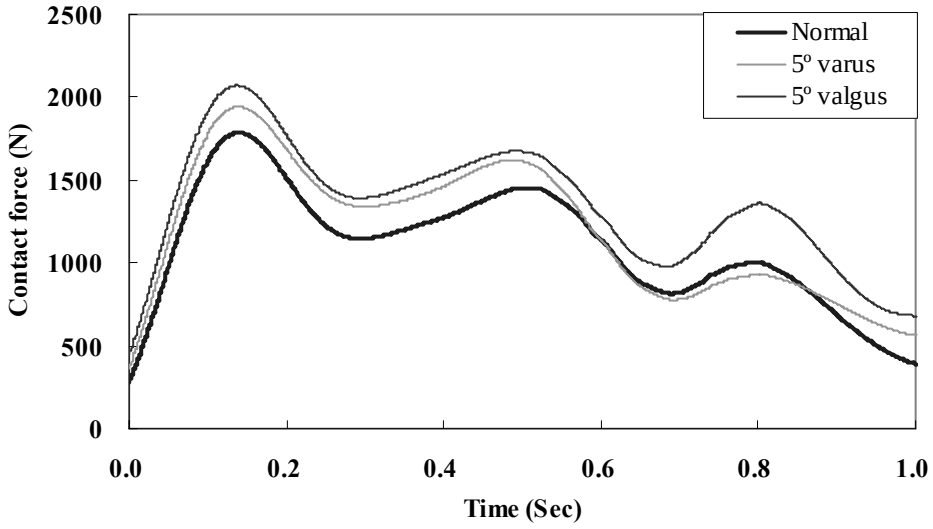

Figure 6-16 Tibio-femoral contact force during a gait cycle in different conditions of alignment

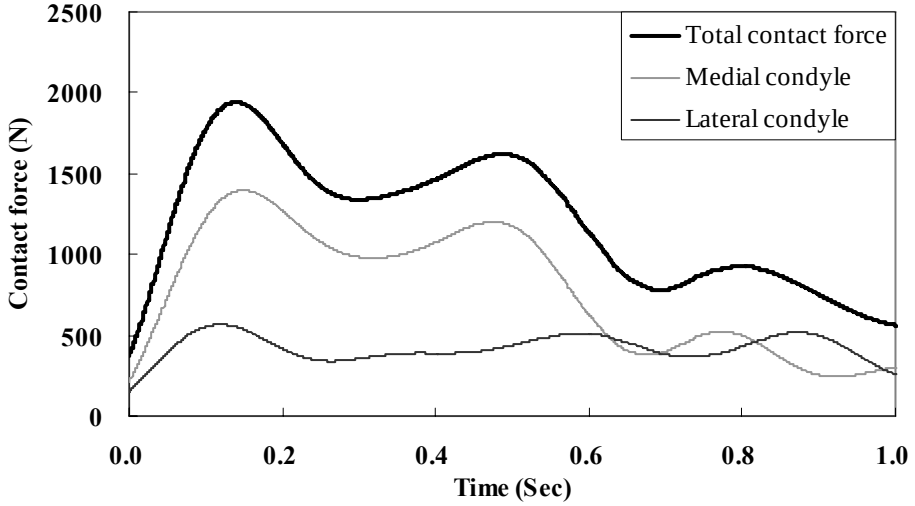

(a)

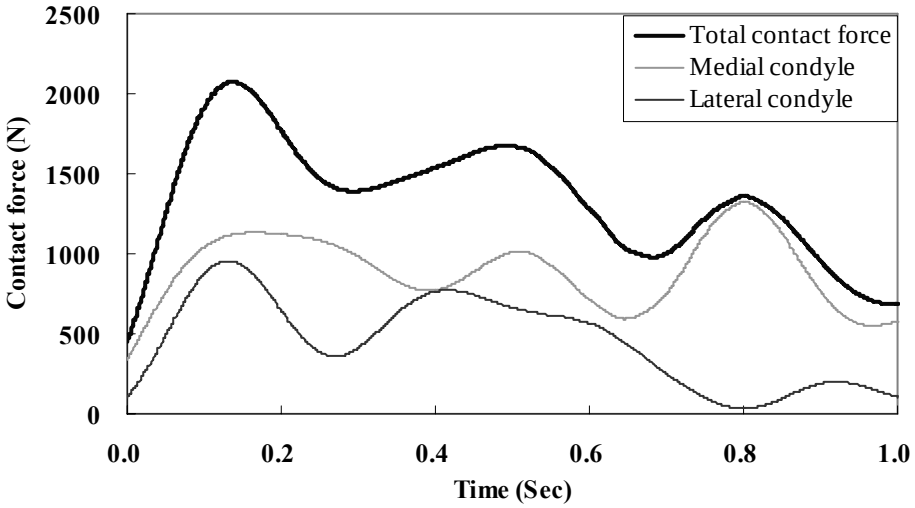

(b)

Figure 6-17 Tibio-femoral contact force in condition of: (a) 5 degree varus and (b) 5 degree valgus

Figure 6-16 shows the total tibio-femoral contact force in different conditions of alignment. Apart from a short section in the swing phase of the gait cycle where varus malalignment gives a marginally lower contact force than for normal alignment, varus/valgus malalignment increases the tibio-femoral contact force in the joint. Figure 6-17 shows the contact force on the medial and lateral condyles during a gait cycle for varus and valgus malalignment. In varus malalignment, the varus moment on the knee joint increases, and the contact force on the medial side increases during the stance phase (Figure 6-17a). In

valgus malalignment, the varus moment in the knee joint decreases, and the difference in contact force between the medial and lateral sides decreases during the stance phase (Figure 6-17b). During the swing phase, the vertical force decreases (Figure 6-2a) and the quadriceps force has a major effect on the tibio-femoral contact force resulting in a bigger contact force on the medial side. The large contact force on the medial side in condition of valgus malalignment indicates the abnormal performance of the quadriceps force due to malalignment.

6.5 Influence of malalignment on stress and strain distribution in distal femur

The stress and strain distributions in the distal femur in different conditions of malalignment are compared in Figure 6-18 and Figure 6-19 at various stages of the gait cycle. Considering zones L3 to L10 and M3 to M10, Figure 6-18 and Figure 6-19 demonstrate high stress/strain on the medial side of the distal femur in condition of varus, and high stress/strain on the lateral side in condition of valgus at 0.15 second and 0.5 second (stance phase) respectively. At 0.7 second of gait cycle, the stress/strain on the medial side of the distal femur in condition of valgus are higher than that in condition of varus. At zones L3/M3 to L10/M10, the stress/strain distributions on the medial/lateral side are consistent with the tibio-femoral contact distribution. At zones L1 and L2, the stress and strain are higher in condition of varus compare to the condition of valgus.

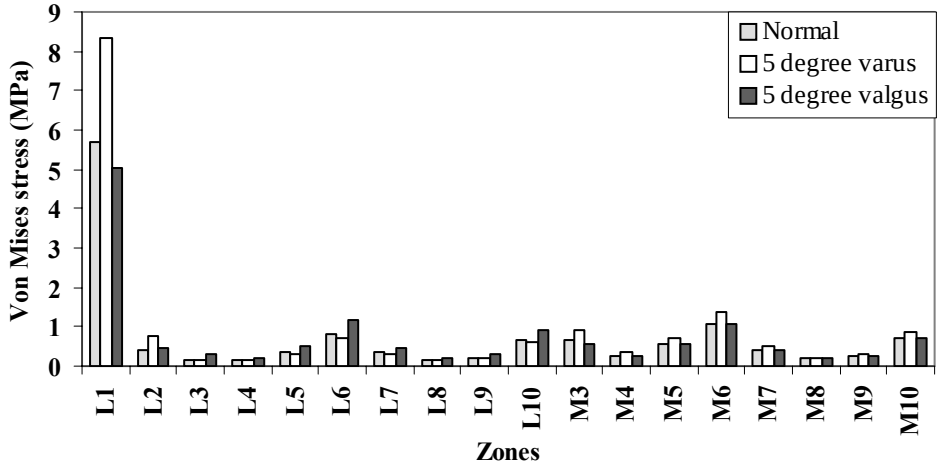

(a)

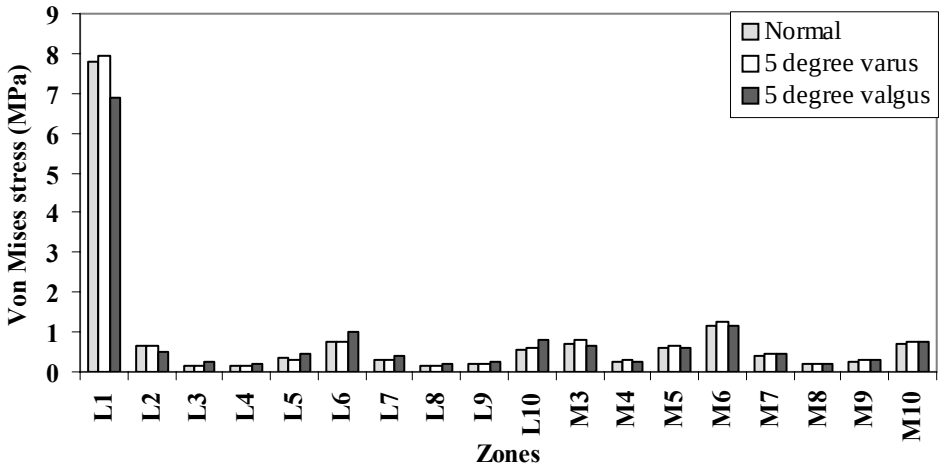

(b)

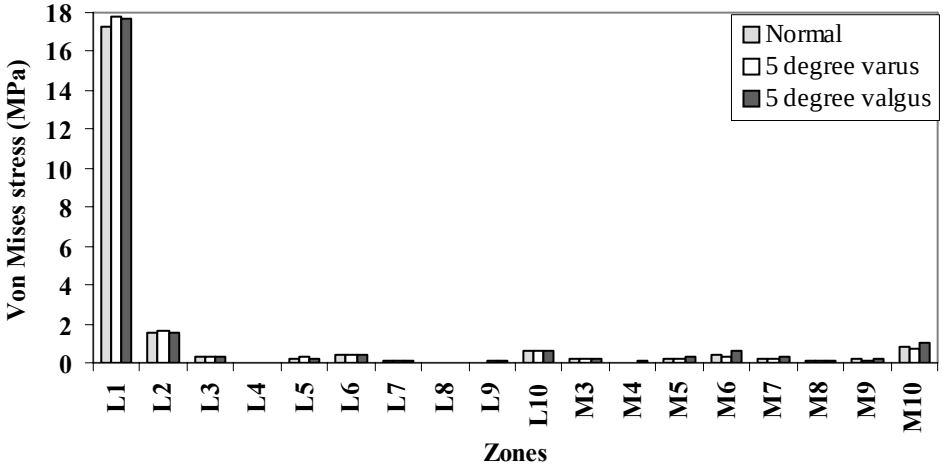

(c)

Figure 6-18 Stress distribution in distal femur in different conditions of alignment at: (a) 0.15 second, (b) 0.5 second and (c) 0.7 second of gait cycle

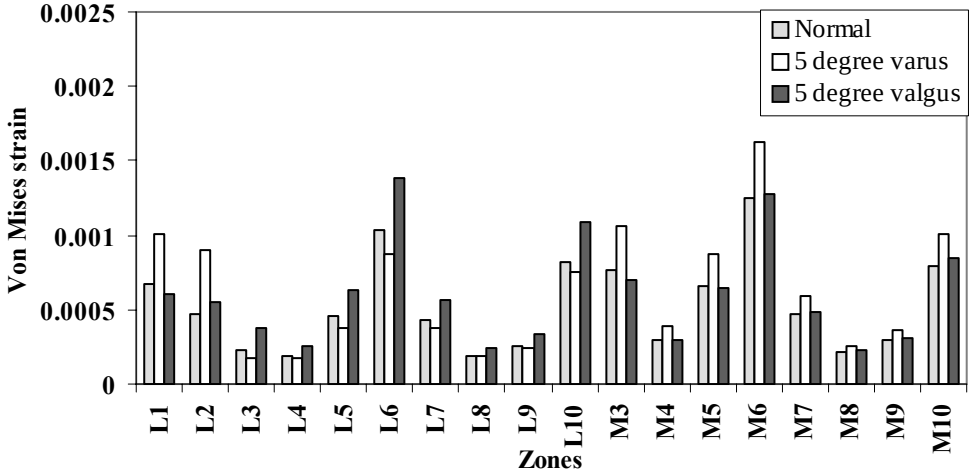

(a)

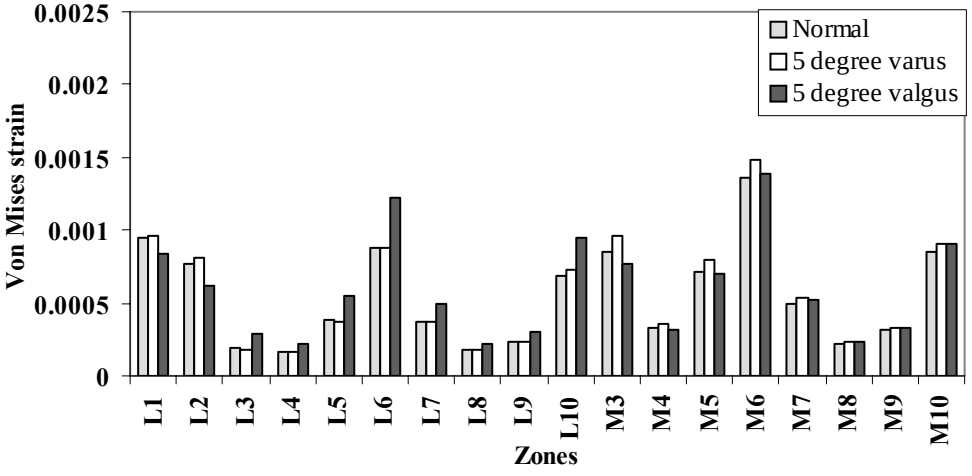

(b)

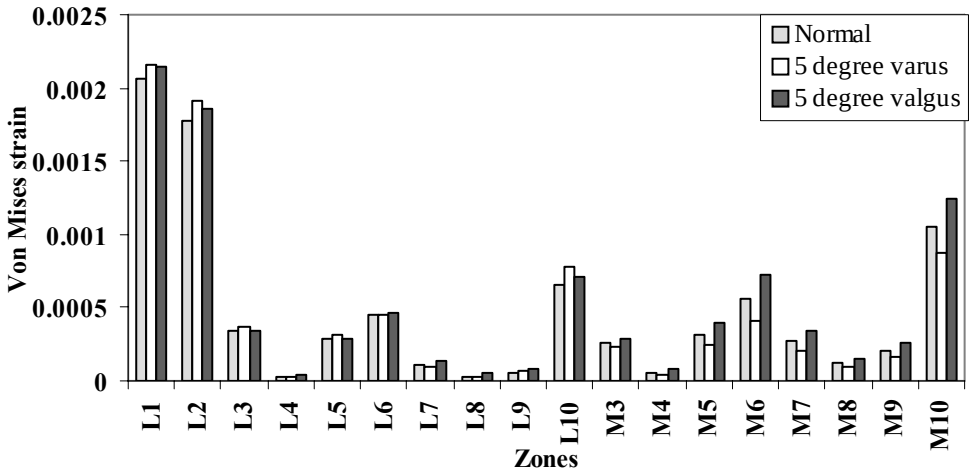

(c)

Figure 6-19 Strain distribution in distal femur in different conditions of alignment at: (a) 0.15 second, (b) 0.5 second and (c) 0.7 second of gait cycle

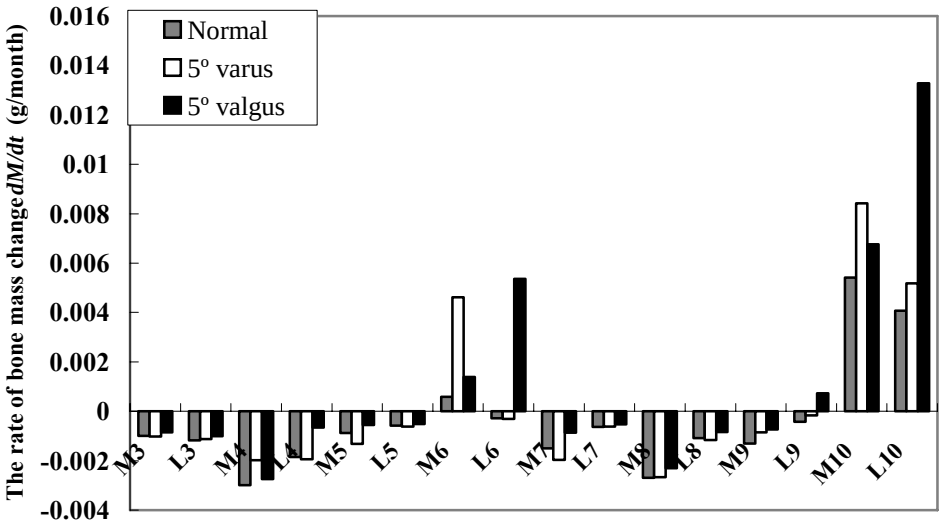

Figure 6-20 The rate of bone mass change per unit volum (mm^3) in distal femur in different conditions of knee alignment

Figure 6-20 shows the rate of bone mass change at different zones of the distal femur in the different conditions of knee alignment, the bone loss at the distal end of the femur occurs in all conditions. In comparison with normal condition, the following results have been obtained:

- In condition of varus, more bone formation appears at zone M6 and M10.
- In condition of valgus, the bone density increases at zones L6 and L10.
- In condition of valgus, bone loss at zones L3, L4, L5, L7, L8 and L9 is less than for normal alignment and varus malalignment. This characteristic would result in less bone loss at the lateral condyle.

6.6 Discussion

After total knee replacement, with load transfers from knee prosthesis to bone in knee motion, the high stiffness of the knee prosthesis will alter the load distribution at the implant bone interface in the knee joint. The change in the load distribution increases stresses in some regions and reduces them in others. If these changes are large enough they can lead to adaptive bone remodelling.

Bone loss in the distal anterior femur can lead to loosening of the component and cause difficulties during a revision knee arthroplasty. It has been reported that loosening of the femoral component may result from condylar osteoporosis (Petersen *et al.* 1995, Spittlehouse *et al.* 1999, Soininvaara *et al.* 2004). Other studies have demonstrated stress shielding and bone loss in the anterior distal femur (Cameron and Cameron 1987, Mintzer *et al.* 1990, Petersen *et al.* 1995). In this research we have demonstrated an increase in stress in zone L1 of the distal femur. The stress values decrease in zones L/M4 and L/M8, which supports the argument that there is significant stress shielding in the distal femur. High gradients of stress values were found at zone L1 to zone L2. High gradients of stress at the anterior distal femur will result in a higher gradient of bone density distribution and increased stress shielding in the anterior distal femur. The mechanical strength of the bone is related to its density, and bone loss in the anterior distal femur has been cited as a risk factor for supra-condylar fractures of the femur following TKR (Kraay *et al.* 1992). The finite element model of the distal femur in this research has shown that there is a concentration of stress in the anterior distal femur at the margin of the prosthesis (Figure 6-9) and this is immediately adjacent to a relatively low stress region after TKR. The maximum stress and strain in this model, however, were below the yield stress and strain of bone. From the above analysis, we can predict that in vivo movement like walking upstairs and downstairs will result in higher stress and strain at zone L1; this could help to explain one of the mechanisms behind post-operative supra-condylar fracture.

The pegs used on the femoral component are intended as an aid to the correct placement of the component but they also help to transfer the load to the disphyseal part of the bone and improve stability (van Lenthe *et al.* 2002). It has been found that the pegs can influence the stress distribution in the surrounding bone. In the region over and around the femoral pegs, Petersen *et al* (Petersen *et al.* 1995) found an increase in BMD of 22% after 2 years. In this chapter, it can be seen that higher stress and strain energy density occurs above and around the pegs. Figure 6-15 shows increase of bone density at zone M6 and decrease of

bone density at zone L6. Lower stresses were found around the base of the pegs; there may be some contribution to stress shielding resulting from the stiffness of the pegs. Decrease of bone density were found at both side of the distal end of the femur. More research on the influence of peg geometry on stress distribution may reveal an ideal size of peg to optimise stress distribution in the distal femur. The influence of femoral component peg geometry on stress distribution in the distal femur will be discussed in Chapter 7.

The influence of varus/valgus malalignment on tibio-femoral contact force and stress/strain distribution in the distal femur was also investigated. The difference in contact force on the medial and lateral condyles decreased in condition of valgus malalignment during the stance phase. The strain distribution in the distal femur is related to the tibio-femoral contact force. Although the strain energy density distribution varied in different conditions of malalignment, bone loss was predicted in all situations. However, less bone loss was predicted at the lateral condyle for the valgus malalignment condition.

6.7 Conclusions

In this chapter, a dynamic model of a knee joint has been developed with MSC/ADAMS and MSC/MARC software. In this model, the distal femur has been modelled as a flexible body and the stress distribution in the distal femur during daily activities has been analysed. Using this dynamic model, a gait cycle load of normal walking has been successfully simulated.

There was a decrease in the stress in the distal margin of the bone adjacent to the implant which proves that there was stress shielding in the distal femur. The potential loss of bone density in the distal femur was predicted from the rate of bone mass change $\frac{dM}{dt}$. The bone loss in the distal femur will ultimately lead to femoral component loosening.

Higher stresses were identified around the femoral component pegs. This potentially helps to maintain bone density. Bone density increased at this area of

medial side. The design of the femoral component pegs also needs to be considered in order to reduce stress shielding around the bottom of the pegs and improve bone density increase around the pegs. More research on the influence of peg geometry on stress distribution in the distal femur will be considered in the next chapter.

Varus/valgus malalignment will redistribute the tibio-femoral contact force and stress/strain distribution in the distal femur. The difference in contact force between the medial and lateral condyles decreased during the stance phase with valgus malalignment. In all alignment conditions, bone loss would then occur at the distal end of the femur.

Because the stress distribution in the distal femur in this dynamic model was consistent with other investigators' research findings, the dynamic model in this paper could be used to analyse the stress distribution in the distal femur with different dynamic load conditions and thus optimise implant designs.

Chapter 7

The influence of femoral component peg geometry on stress distribution in distal femur

7.1 Introduction

As discussed in the last chapter, stress shielding occurred in the distal femur. Higher stress was found above the femoral component peg and lower stress was found at the distal end of the femur. It is obvious that the shape of the peg will influence the stress distribution in the distal femur. To reduce the stress shielding in the distal femur, the shape of the peg of the femoral component was studied.

The pegs used in the femoral component are intended as an aid to the correct placement of the component but they also help to transfer the load to the diaphyseal part of the bone and improve stability (van Lenthe *et al.* 2002). In van Lenthe's research, bone remodelling in the distal femur was simulated with different types of knee prostheses implanted. The computer simulation model showed that revision stemmed femoral knee prostheses tend to cause more bone resorption in most distal regions due to higher stress shielding. Van Rietbergen *et al.* (2001) investigated stress shielding around ABG hip prostheses. Nyman *et al.* (2003) investigated the ability of an interlocking screw fixation technique to minimize bone loss related to stress shielding in the tibia. In other investigators' research, the stress shielding in bones with revision knee prostheses were analysed (van Rietbergen *et al.* 2001, Nyman *et al.* 2003); the design of peg geometry in the primary implant was not investigated. This chapter reports on the investigation of several femoral component designs with different peg shapes.

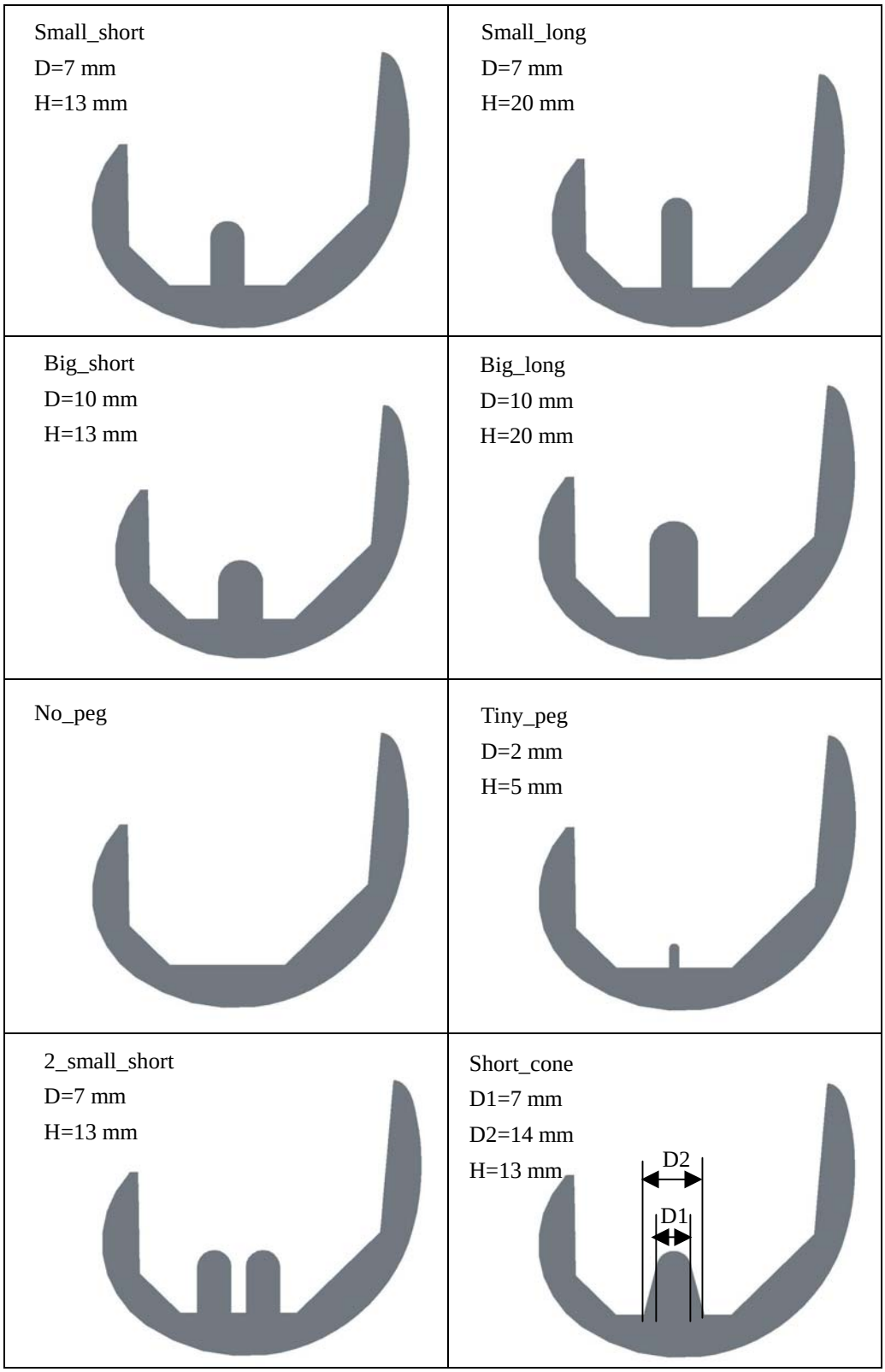

Figure 7-1 Different designs of femoral component with varying peg shape

7.2 Model introduction

Figure 7-1 shows various designs of femoral component with different peg shapes. These femoral components were used in the dynamic model explained in Chapter 6 and stress distributions in the distal femur with different implants were obtained.

7.3 Results

To compare the bone remodelling situations with different prostheses, the rate of bone mass change $\frac{dM}{dt}$ were calculated. The strain energy density at all zones at 0.15, 0.5 and 0.7 second of the gait cycle were used to calculate the rate of bone mass change. The bone at zone L1 was defined as cortical with a density of 1.73 g/cm^3, which is the upper bound bone density for bone remodelling; no bone remodelling would occur at zone L1 according to the results in Chapter 6. Therefore, in Figure 7-2, the rate of bone mass change $\frac{dM}{dt}$ per unit volume (mm^3) at zones L2 to L10 only were compared for different designs of femoral component peg. To ensure the $\frac{dM}{dt}$ was compared at the same positions in different designs, zones 5, 5l, 7 and 7l were defined. Zone 5 and 7 are the zones around the peg and 13 mm (the height of the short peg) above the root of peg; zone 5l and 7l are the zones around the peg and 20 mm (the height of long peg) above the root of the peg.

Figure 7-2 shows the rate of bone mass change $\frac{dM}{dt}$ for different peg designs. In the no_peg and tiny_peg designs, it was noticed that there was less bone loss at the zone 4 and zone 8 comparing to the small_short design. However, the bone loss at the zone 6 is higher than that in other designs. In the no_peg and tiny_peg designs, the stabilization function of the peg was removed but there was no significant improvement on bone loss in the distal end of the femur. Therefore, the no_peg and tiny_peg designs are not recommended.

Compare to other designs, the big_long design results in the most serious bone loss at the distal femur zones 3, 4, 5, 7 and 8 and less bone formation at the zone 2. Although bone formation was found at the zone 6, the stress shielding was severe in this design and more bone was removed. Therefore, the big_long design is not suggested.

It can be seen in Figure 7-2, the 2_small_short design results in more bone loss at the zone 4 and zone 5 comparing to the small_short design and did not improve bone formation at the zone 6. Similar bone remodelling distribution was found in the small_short, short_cone and big_short designs, it was noticed that the big_short design slightly resulted in more bone loss at the zone 5 and zone 7. Compare to the small_short design, more bone was removed and more bone loss happened at the distal end in the short_cone, big_short and 2_small_short design. Therefore, these three designs are not recommended.

Comparing to the small_short design, slightly more bone loss occurred at the zones 3, 4, 5, 7, 8 in the small_long design; however, significant bone formation was predicted at the zone 2 and zone 6. The high density at the zones 2, 6 and 10 will increase the stability of the femoral component. This significant bone formation will compensate the bone loss at the distal end. Therefore, the small_long peg is the best of the designs based on that there are more bone formation around the peg and hence the increase of the component stability.

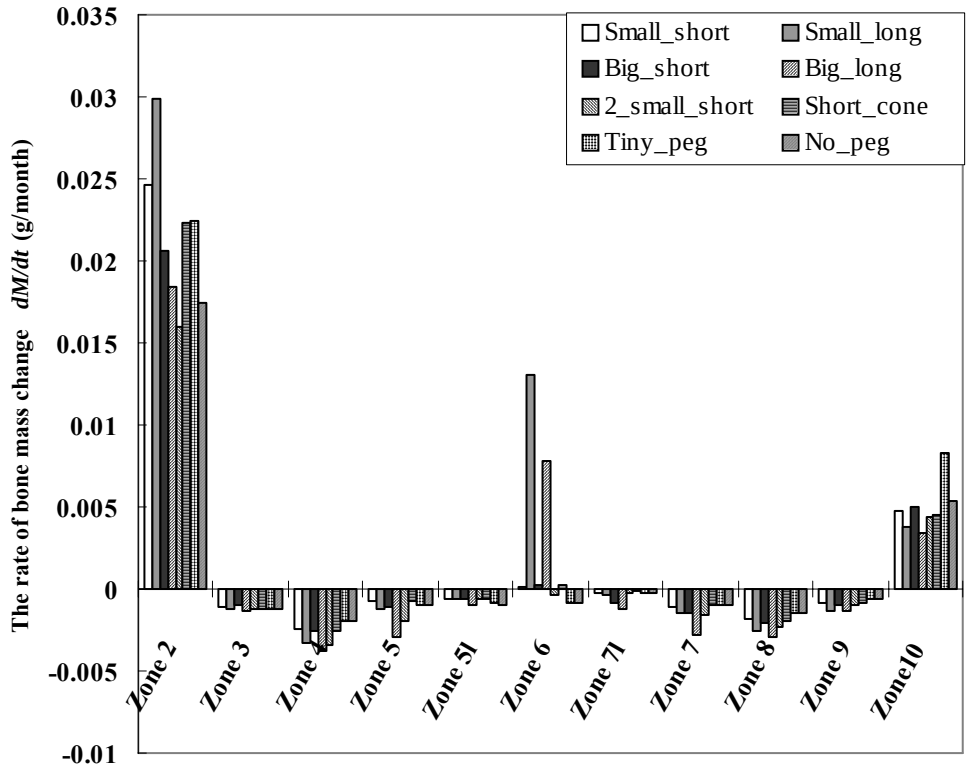

Figure 7-2 Comparison of the rate of bone mass change per unit volume (mm^3) at different zones of distal femur with different peg designs of femoral component

7.4 Discussion and conclusions

In this chapter, different designs of femoral component peg were studied in the dynamic model of the implanted knee joint. The influence of geometry of the femoral component peg on stress distribution in the distal femur was investigated. Stress shielding at the distal end of the femur appeared in all designs. Based on the investigated designs, the stress shielding at the distal end of the femur could not be improved efficiently.

Bone formation appeared at zone 6 in the big_long design; however, too much bone was removed and serious stress shielding also occurred. The big_long design is not recommended, based on the results in this chapter.

In the small_long design, the rate of bone formation was much higher at zone L6 compared to the intact bone. The increase in bone density will help stabilize the

femoral component of the knee prosthesis. Based on the results for all the variations of peg sizes, the small_long design is probably the best.

Obviously, the performance of different peg designs needs to be tested in experimental and clinical trials.

Chapter 8

The influence of body weight on stress distribution in distal femur and UHMWPE

8.1 Introduction to obesity

According to a report of the World Health Organization, obesity has reached epidemic proportions globally, with more than 1 billion adults overweight and at least 300 million of them clinically obese. Obesity significantly increases the risk of developing numerous medical conditions including hypertension, stroke, respiratory disease, diabetes, gout, osteoarthritis, certain cancers and various musculoskeletal disorders, particularly of the lower limbs and feet. Longitudinal data have shown that obesity is a powerful risk factor for the development of knee osteoarthritis, with one twin study finding a 9–13% increased risk for the onset of the disease with every kilogram increase in body weight.

In the clinic, overweight and obesity is commonly assessed by using body mass index (BMI), defined as the weight in kilograms divided by the square of the height in metres (kg/m^2). This is a measure well suited for the purpose of determination of adiposity because it correlates closely with body mass but only poorly with height and it avoids the misleading conclusion of obesity based solely on weight without consideration of height. A BMI over 25 kg/m^2 is defined as overweight, and a BMI of over 30 kg/m^2 as obese. A BMI greater than 40 kg/m^2 is defined as morbid obesity (Namba *et al.* 2005).

8.2 Obesity and TKR failure

The effect of obesity on the outcome of total knee arthroplasty has been reported to be variable. Several reports have implicated excessive weight as a negative predictor of success of TKR (Harrison *et al.* 2004, Healy *et al.* 1995, Namba *et al.* 2005). Other authors have reported less significant differences in TKR outcomes between obese and non-obese patients (Deshmukh *et al.* 2002, Foran *et al.* 2004, Griffin *et al.* 1998, Mont *et al.* 1996).

Namba *et al.* (2005) reported 6.7 times higher risks for infection in obese TKR patients. Healy *et al.* (1995) associated increased body weight with a higher incidence of patello-femoral complications. Harrison *et al.* (2004) compared the clinical outcomes in overweight women with those of a group of normal-weight women 4 to 11 years after TKR. They found that overweight women have poorer outcomes related to quality of life and satisfaction with surgery than normal-weight women.

By analysing outcome 1-year after TKR, Deshmukh *et al.* (2002) found that body weight did not influence adversely the outcome of TKR in the short-term. Mont *et al.* (1996) found no significant differences in cementless TKR outcomes in obese and non-obese patients at a mean follow-up of approximately 7 years. Griffin *et al.* (1998) reported similar overall TKR results between obese and non-obese patients at a mean follow-up of 10.6 years, but did find an increase in minor, non-progressive, radiolucent lines in the obese patients. Foran *et al.* (2004) reported 15 years long-term follow-up of TKR; although not statistically significant, there was trend for obesity to influence the rate of aseptic loosening.

8.3 Kinematics of obese gait

Walking is a fundamental movement pattern, the most common mode of physical activity. However, walking is an extremely complex biomechanical process, involving interplay between muscular and inertial forces. The quality of gait is associated with the structural and functional constraints imposed by the locomotor system, the ability to implement an effective motion strategy and the individual's metabolic efficiency. One of the potential challenges to the normal pattern of walking in the overweight and obese is the need to carry excessive body weight over the long term.

Gait analyses on obese individuals have identified kinematic adaptations including slower velocity, shorter step length, increased double support time, decreased knee range of motion and larger ground reaction forces in obese compared to lean individuals (McGraw and McClenaghan 2000). Spyropoulos *et al.* (1991) compared the movement of the hip, knee and ankle in obese and

normal-weight men while the subjects walked over level ground at their preferred speed. Obese adults were found to adopt a slower walking velocity than non-obese subjects during testing. DeVita and Hortobagyi (2003) tested the effects of obesity on lower extremity joint kinetics and energetics during walking by analysing motion of obese healthy adults and lean adults. They found obese participants used altered gait biomechanics and had less knee torque and power at their self-selected walking speed; however, they had equal knee torque and power while walking at the same speed as lean individuals. Although gait analysis of obese individuals has been conducted by other researchers, no detailed description could be obtained. Therefore, gait analysis of obese TKR patient still needs to be investigated more thoroughly in future. To study the effect of overweight on knee and knee replacement implants, we have to assume that the gait cycle of obese individuals is similar to that of normal people but with larger hip reaction forces and quadriceps forces.

8.4 Method

To investigate the influence of body weight on stress distribution in the distal femur, the conditions of 1.5 and 2 times normal weight were simulated by apply 1.5 and 2 times vertical load and quadriceps load in the dynamic model developed in Chapter 6. Stress distributions in the distal femur for different body weight can then be compared.

To investigate the influence of overweight on the contact pressure in the tibial bearing component, a 1.5 times vertical load was applied in the FE model described in Chapter 5. Fixed- and mobile-bearing implant with three different thicknesses of tibial bearing component (6.8 mm, 9.6 mm and 12.3 mm) were then compared for normal and overweight gait loads.

8.5 Results

8.5.1 Influence of body weight on stress distribution in distal femur

The stress distributions in the distal femur were simulated for 1, 1.5 and 2 times normal weight with the dynamic model developed in Chapter 6.

Figure 8-1 shows the von Mises stress levels at different zones for normal weight, 1.5 and 2 times normal weight. Figure 8-2 shows the strain at different zones in the three conditions. Figure 8-1 and Figure 8-2 indicate increase of stress and strain levels in all zones in conditions of overweight. Stresses and strains at 0.15 and 0.5 second (stance phase) increased in proportion to weight as vertical force was the major force during this period. The increase of stress and strain at 0.7 second was not proportional to body weight. It can therefore be concluded that the increase of stress and strain for overweight subjects is directly related to the vertical load on the knee joint. In the present investigation of walking gait cycle, the increase of stress and strain in conditions of overweight will not result in failure of the distal femur, because the maximum stress and strain were less than the yielding stress of the bone structure.

Figure 8-3 shows the rate of bone mass change at different locations for different body weights. Comparing to normal weight, serious stress shielding was found in condition of overweight, much more bone loss were found in the distal end of the femur. Bone formation was found at zone 6 in condition of normal weight; however, bone loss was found at zone 6 in condition of overweight. Bone formation was found at zone 2 and zone 10. Less bone formation was found at zone 2 in condition of overweight comparing to normal weight.

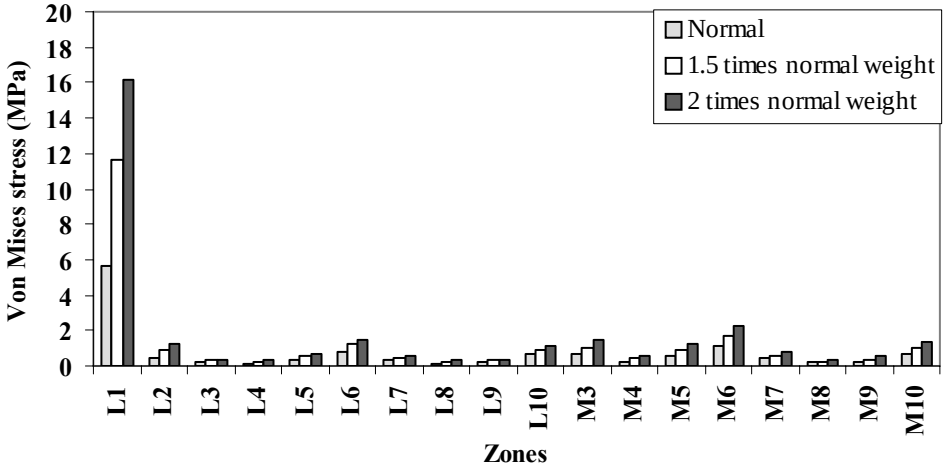

(a)

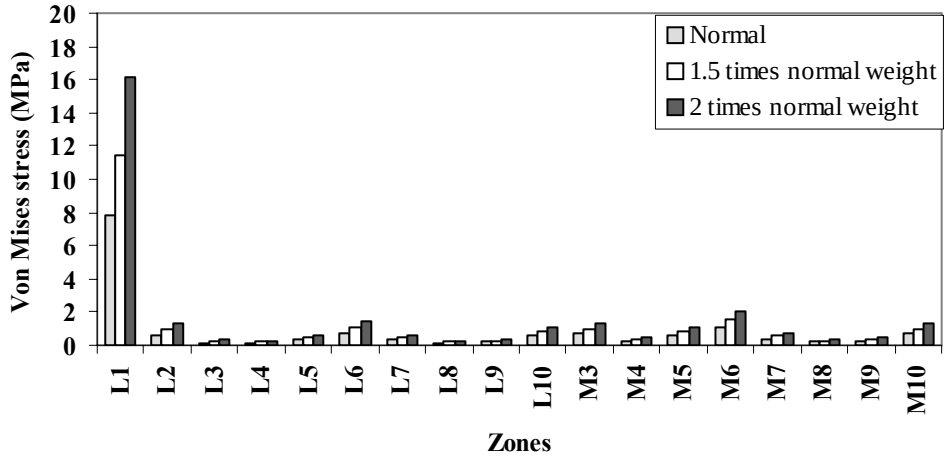

(b)

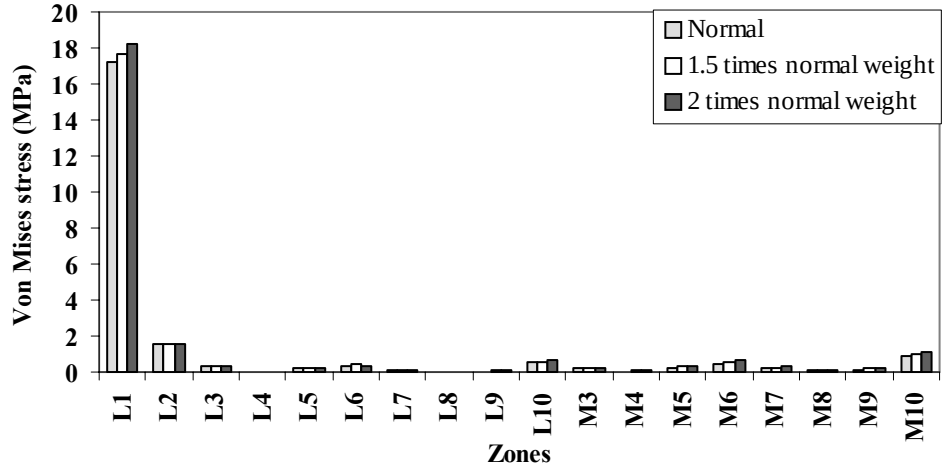

(c)

Figure 8-1 Comparison of stress distribution in distal femur after TKR with different body weight at: (a) 0.15 second, (b) 0.5 second and (c) 0.7 second of gait cycle

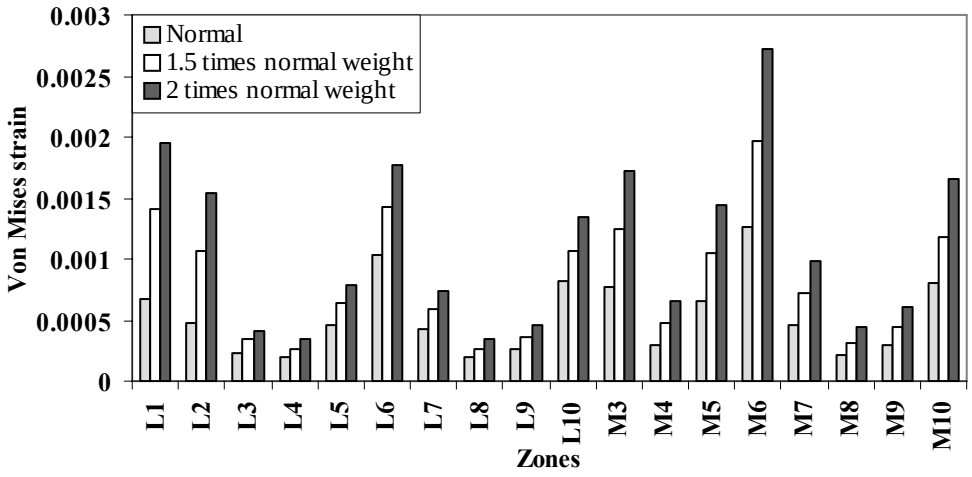

(a)

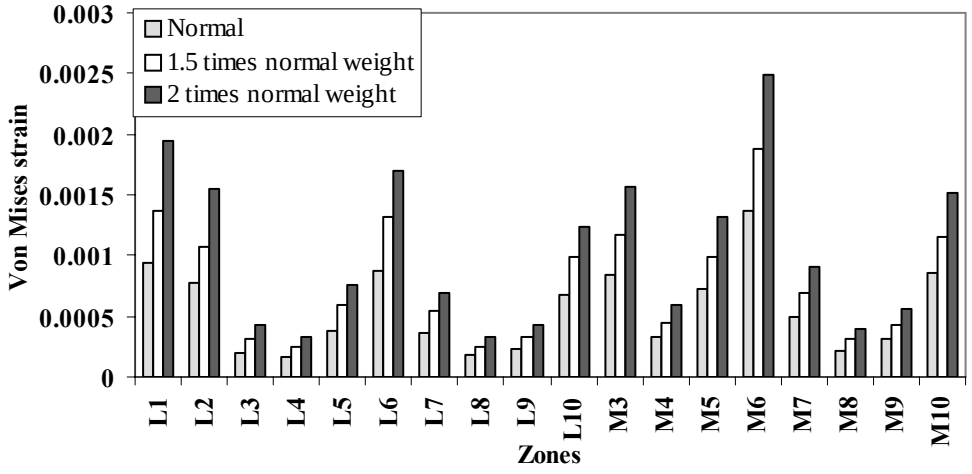

(b)

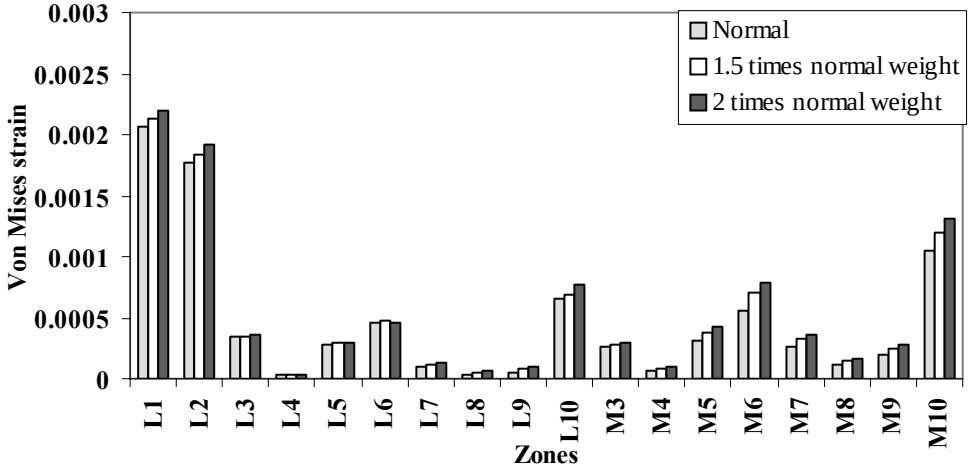

(c)

Figure 8-2 Comparison of strain distribution in distal femur after TKR with different body weight at: (a) 0.15 second, (b) 0.5 second and (c) 0.7 second of gait cycle

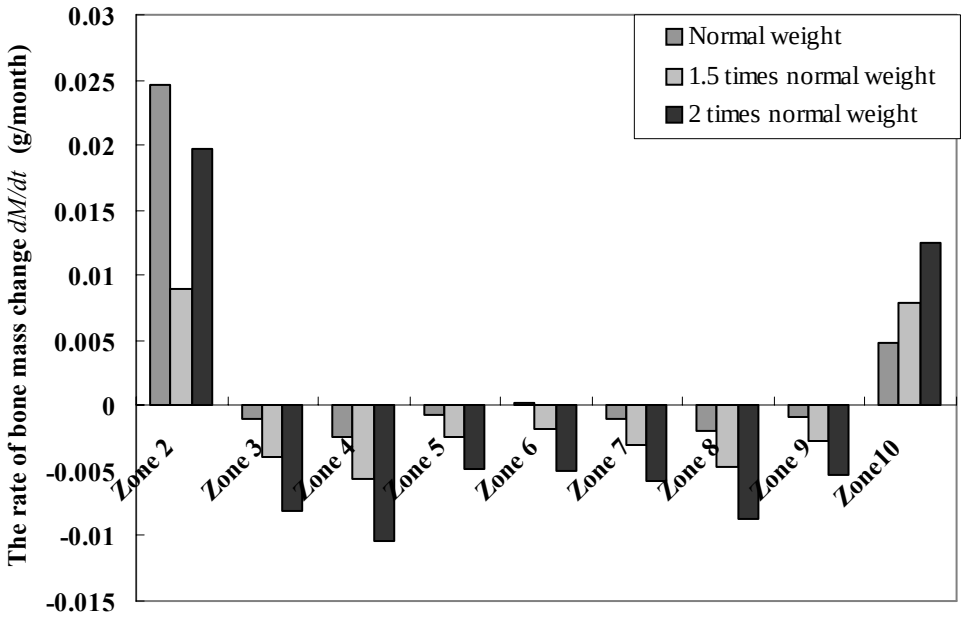

Figure 8-3 The rate of bone mass change per unit volume (mm^3) in distal femur after TKR with different body weight

8.5.2 Influence of body weight on tibio-femoral contact force

Tibio-femoral contact forces during the gait cycle with different body weight were obtained from dynamic simulation of a gait cycle using the model developed in Chapter 6. Figure 8-4 shows the tibio-femoral contact force during a gait cycle for different body weights. Contact forces increased by around 43% and 87% during the stance phase in line with the increase in body weight. This increased force will increase the risk of wear of the tibial bearing component and loosening between the tibial tray and the proximal tibia.

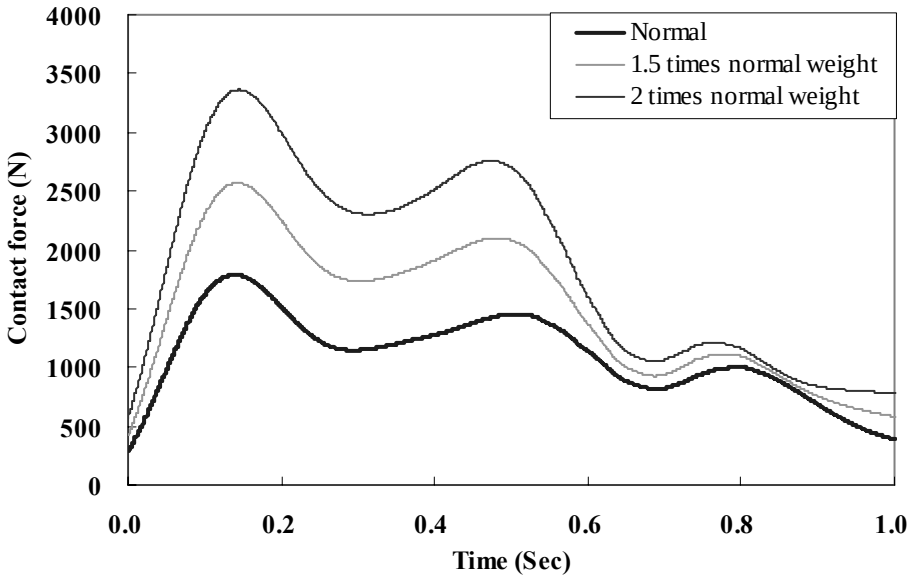

Figure 8-4 Tibio-femoral contact force during gait cycle with different body weight

8.5.3 Influence of body weight on tibio-femoral contact pressure

To investigate the influence of body weight on contact pressure in knee implants, normal weight and overweight were simulated with the FE model developed in Chapter 5. An increased vertical load (1.5 times) was applied to simulate overweight. Figure 8-5 shows the contact pressure in a fixed-bearing implant with different thickness designs for normal weight and overweight. Figure 8-6 and Figure 8-7 compare the contact pressure in a mobile-bearing implant with different thickness designs for normal weight and overweight.

In Figure 8-5, Figure 8-6 and Figure 8-7, the influence of the thickness of the tibial bearing component on the contact pressure distribution in the fixed- and mobile-bearing implant was not changed in the overweight condition. In the fixed-bearing implant, contact pressures in the 9.6 and 12.3 mm thickness design were lower than 6.8 mm design in both normal weight and overweight conditions. In the mobile-bearing implant, the increase in thickness of the tibial bearing component did not decrease the contact pressures on the superior surface of the tibial bearing component in the knee implant, but it increased the contact pressure on the inferior surface of mobile-bearing implant in all body weight conditions.

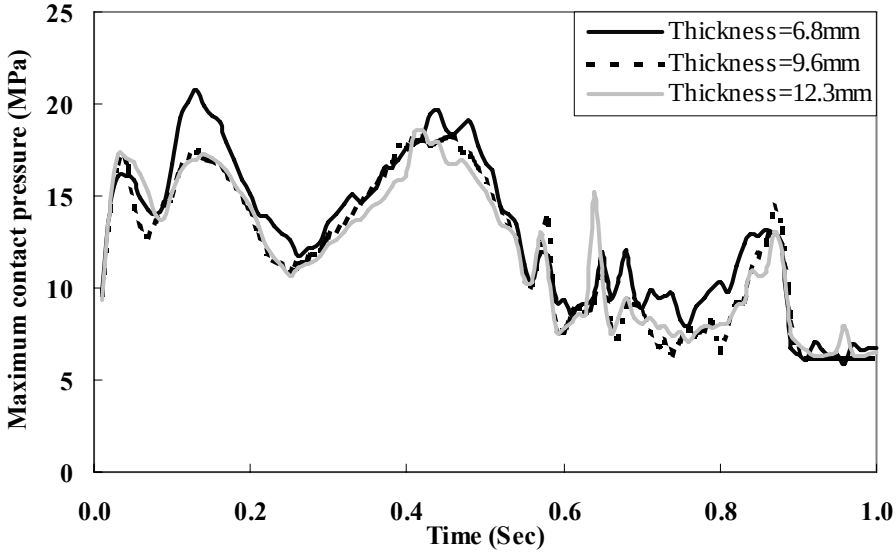

(a)

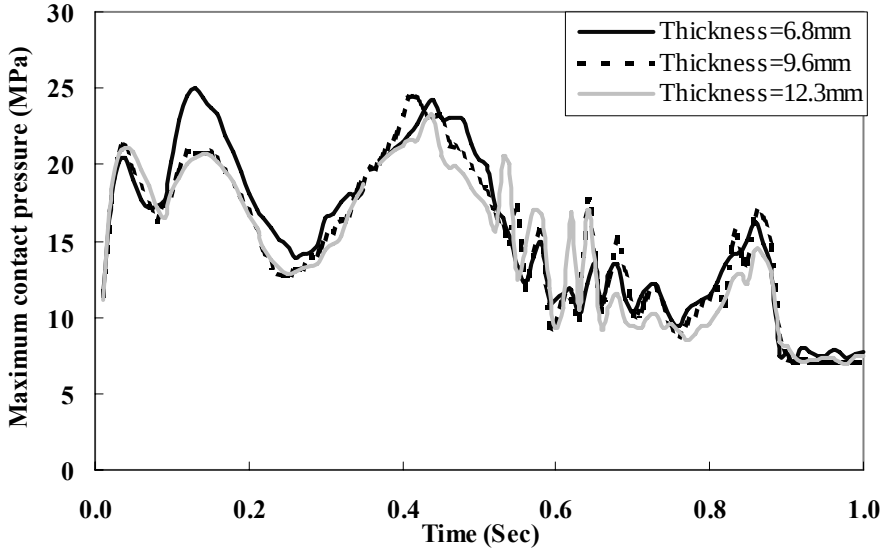

(b)

Figure 8-5 Comparison of maximum contact pressure in fixed-bearing implant in condition of: (a) normal weight and (b) overweight

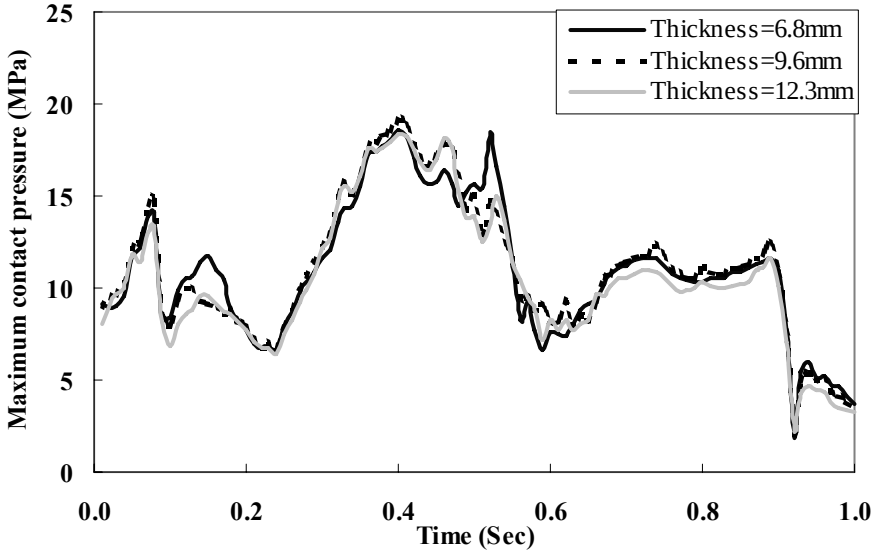

(a)

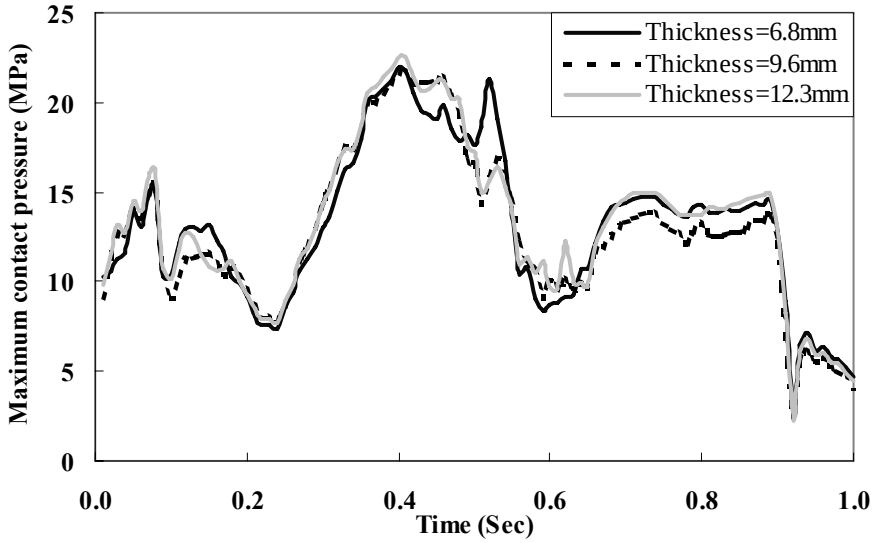

(b)

Figure 8-6 Comparison of maximum contact pressure on superior surface of mobile-bearing implant in condition of (a) normal weight and (b) overweight

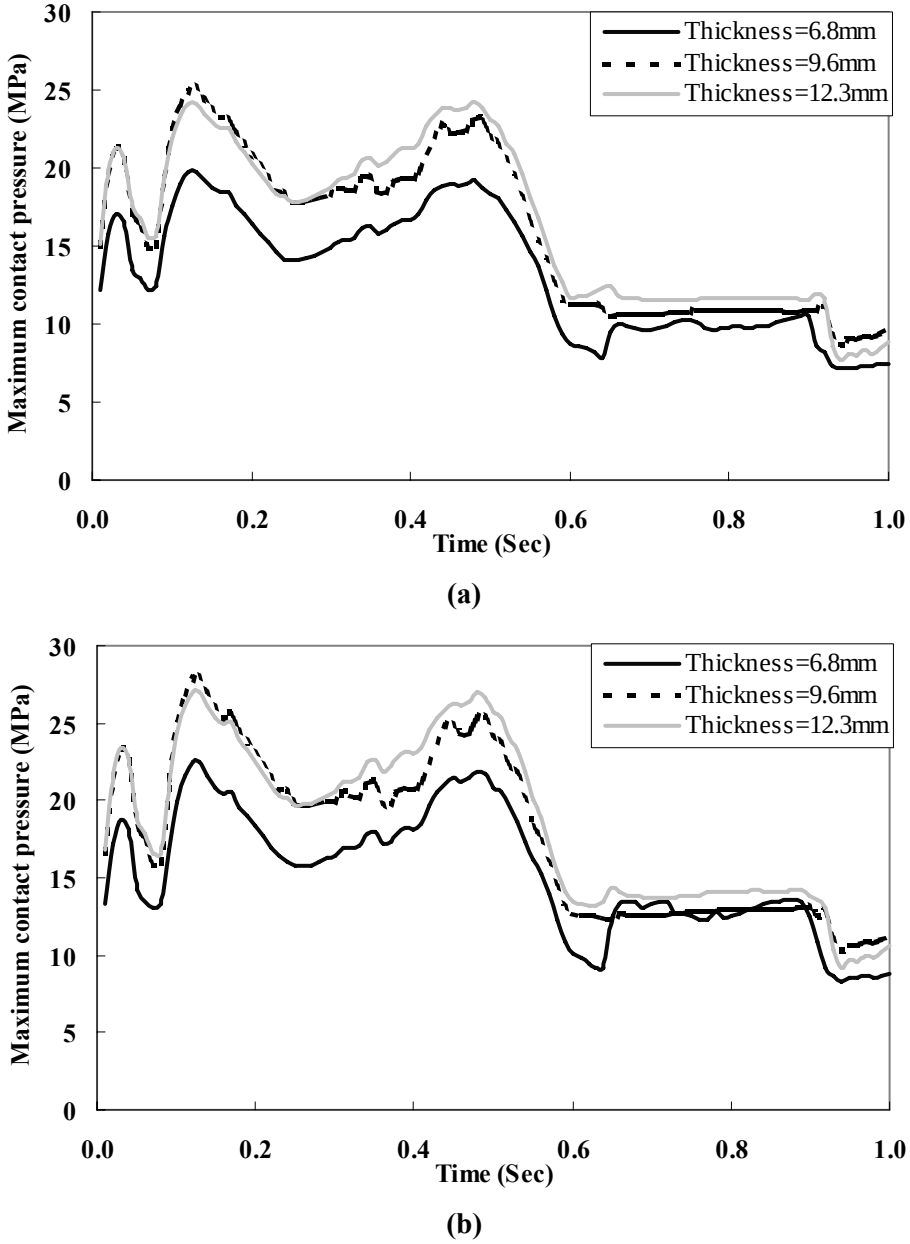

Figure 8-7 Comparison of maximum contact pressure on inferior surface of mobile-bearing implant in condition of (a) normal weight and (b) overweight

According to the conclusion in Chapter 5, the fixed-bearing implant with a 9.6 mm tibial bearing component and the mobile-bearing implant with a 6.8 mm component were better than the other designs. These two designs were compared for the normal weight and overweight conditions. In the fixed-bearing implant with the 9.6 mm thick tibial bearing component, the maximum contact pressures were 18.15 MPa and 24.41 MPa for the normal weight and overweight

conditions respectively. In the mobile-bearing implant with a 6.8 mm thick tibial bearing component, the maximum contact pressures were 18.54 MPa and 21.94 MPa on the superior surface, and 19.72 MPa and 22.51 MPa on the inferior surface for normal weight and overweight, respectively. The increase of maximum contact pressure was 6.26 MPa in the fixed-bearing implant, and 3.4 MPa and 2.79 MPa on the superior and inferior contact surfaces of the mobile-bearing implant, respectively. Thus, lower maximum contact pressure and less increase in maximum contact pressure were found in the mobile-bearing implant than the fixed one. It therefore seems that the mobile-bearing implant performs better in the overweight condition.

8.6 Discussion and Conclusions

In this chapter, the stress distributions in the distal femur and the tibial bearing component for normal weight and overweight were investigated; the influence of body weight and thickness of the tibial bearing component on the contact pressure in the fixed- and mobile-bearing implants were compared using an assumed gait load cycle.

8.6.1 Stress distribution in distal femur

In dynamic analysis of the implanted knee joint, the stresses in the distal femur were found to increase with body weight; the stresses increased proportionally during the stance phase. However, the bone structure in the distal femur will not fracture according to the present investigation during the walking gait cycle. Serious stress shielding was found in condition of overweight.

More bone loss was found at the distal end of femur by the increase of body weight, and the stress in distal femur increased with body weight. According to Taylor and Tanner's research (1997), any implant is initially supported on a necrotic layer of cancellous bone with mechanical properties similar to living bone, but no ability to repair. At first there will be accelerated failure of this dead cancellous bone. They suggested that the risk of cancellous bone failure, and therefore of migration, is proportional to the magnitude of the stresses in

cancellous bone. This indicates that the risk of femoral component migration will increase with body weight.

8.6.2 Contact pressure distribution on contact surfaces

Contact pressure distributions in the fixed- and mobile-bearing implant were compared. Maximum contact pressures in the mobile-bearing implant were almost the same as in the fixed-bearing implant for normal weight. However, in condition of overweight, the maximum contact pressures in the fixed-bearing implant were higher than those in the mobile-bearing implant. Smaller increases in maximum contact pressures were found in the mobile-bearing implant with the increase of body weight. It could be possible to conclude that the mobile-bearing implant is less affected by the increase in body weight and performs better than the fixed-bearing implant in the overweight condition. However, wear on both the superior and inferior contact surfaces in the mobile-bearing implant needs to be further considered.

8.6.3 Influence of thickness of UHMWPE on contact pressure in tibial components

In this chapter, it was found that the tibio-femoral contact force increased proportionally with body weight. The increase in the tibio-femoral contact force resulted in an increase in the contact pressure on the tibial bearing component for all thicknesses of tibial bearing component. The influence of the thickness of the tibial bearing component on the contact pressure distribution in fixed- and mobile-bearing implants was not changed in condition of overweight compared to normal weight; the conclusions reached in Chapter 5 about tibial bearing thickness still apply for the overweight condition.

Chapter 9

Discussion and conclusions

The main reasons for TKR failure are: early wear of the ultra high molecular weight polyethylene (UHMWPE), aseptic loosening, tibial femoral instability, patellar instability, and fatigue failure of the tibial tray (Villa *et al.* 2004). Polyethylene wear and aseptic loosening are the most common reasons for TKR revision.

Early wear of UHMWPE is related to the extension of contact area and to the magnitude of contact pressure. The contact pressure and area depend on the degree of conformity and operative techniques, including mechanical alignment and fixation of the components. Wear can also lead to malalignment or instability of the knee joint. Limb alignment and the shape of the articulating surfaces strongly influence the bone-implant interface stress and the stress distribution in the implanted bones. It has been found that aseptic loosening usually results from malalignment (Vince 2003). Also long-term bone remodelling in the surrounding knee components controlled by mechanical stress will increase the degree of malalignment. Above all, malalignment is the main reason for polyethylene wear and aseptic loosening, but malalignment is also the result of polyethylene wear and aseptic loosening and this leads to further wear and loosening.

The long-term performance of a total knee replacement is dependent on the kinematics of the knee joint. Retrieval studies have shown that the wear in total knee replacements is highly variable and this is attributable to the diverse kinematic and stress conditions that occur in vivo. Gait load is an important factor influencing TKR performance.

Longitudinal data have shown that obesity is a powerful risk factor for the development of knee osteoarthritis. With the global increase in obese TKR patients, the effect of obesity on the outcome of TKR needs to be studied.

This research mainly investigated the influence of gait cycle, malalignment and body weight on a total knee replacement including fixed- and mobile-bearing implant. Variations in the design of total knee replacements such as peg size and tibial tray thickness have also been studied.

9.1 Comparison between fixed- and mobile-bearing implant

In this research, the performance of fixed- and mobile-bearing implant during a walking gait cycle in different conditions of alignment were investigated. In Chapter 4, the same geometric parameters such as sagittal radii and frontal radii of tibial and femoral components were used for both fixed- and mobile-bearing implant. From comparative analysis of the two types of implants under vertical loading, it was found that the maximum contact pressure in the fixed-bearing implant increased significantly from normal alignment to malalignment. The maximum increase of the maximum contact pressure is 10.3 MPa (61%) from normal alignment to 5º varus alignment at 60º flexion. The mobile-bearing implant performed better in reducing the influence of varus and malrotation.

In the fixed-bearing implant, malalignment causes stress increase in both the tibial bearing component and the tibial tray. More increase in von Mises stress is found in the tibial tray of the fixed-bearing implant; the stresses are transferred to the tibial tray in condition of malalignment because of the fixation of the tibial bearing component and the tibial tray in the fixed-bearing implant. However, malalignment has less influence on the tibial tray of mobile-bearing implant.

The mobile-bearing implant performs better in conditions of malalignment especially in malrotation: lower maximum stress in the tibial bearing implant can reduce the possibility of failure of the polyethylene; lower maximum stress in the tibial tray can also reduce the possibility of failure of the tibia tray and loosening.

In Chapter 5, the dynamic performance of fixed- and mobile-bearing implant were compared. The fixed- and mobile-bearing implant models are slightly

different from those in Chapter 4; the models in Chapter 5 are of PFC Sigma system implants, where the conformity of the mobile-bearing implant is higher than that of the fixed-bearing implant. In dynamic analysis of the total knee replacement, the tibio-femoral contact points are more scattered on the superior contact surface of the mobile-bearing implant, whereas the contact points on the contact surface of the fixed-bearing implant are more concentrated. The more scattered contact points in the mobile-bearing implant are a result of the higher conformity and higher contact area in the tibio-femoral joint. The greater rotational movements found in the mobile-bearing prosthesis will place different demands on the bearing surface and at the same time will place greater functional demands on the ligaments.

Comparing the contact pressure distribution in the fixed- and mobile-bearing implant during a gait cycle, the maximum contact pressures are almost the same. However, the contact pressure on the superior surface of the mobile-bearing implant was only two thirds of that on the fixed-bearing implant during most of the stance phase of the gait cycle, this should result in less wear on the superior surface of the mobile-bearing implant.

Compared with a fixed-bearing implant of the same conformity, it can be concluded that the mobile-bearing implant performs better at three stages of the gait cycle in different conditions of malalignment. From the results of the dynamic simulation of a gait cycle in Chapter 5, the maximum contact pressure on the superior surface of mobile-bearing implant were much less than that of the fixed-bearing implant during most of the stance phase of the gait, and less movement between the femoral component and tibial bearing component. This should result in less wear on the superior surface of the mobile-bearing implant. The higher contact pressure at the inferior surface of the mobile-bearing implant was the result of the insert of the tibial bearing component being in contact with the tibial tray when the movement and force were transferred between them. However, the unidirectional friction distance was small during gait cycle. The contact pressure on the flat area of the inferior contact surface in mobile-bearing implant were less that on the superior contact surface in mobile-bearing

implant, less wear will take place on inferior surface of mobile-bearing implant compare to the superior contact surface.

Contact pressure is related to the thickness of the UHMWPE tibial bearing component. In the fixed-bearing implant, contact pressure decreases when the thickness of the tibial bearing component changes from 6.8 mm to 9.6 mm; no further decrease is found when the thickness changes from 9.6 mm to 12.3 mm. In order to achieve lower contact pressure and less bone resection, the 9.6 mm thick tibial bearing component is recommended for the fixed-bearing implant. In the mobile-bearing implant, contact pressures on the superior surface are not significantly decreased when the thickness of the tibial bearing component increases from 6.8 mm to 9.6 mm and 12.3 mm. The 6.8 mm thick tibial bearing component is recommended for the mobile-bearing implant.

In this research, it has been found that the tibio-femoral contact force increases proportionally with body weight. This increase in tibio-femoral contact force results in an increase in contact pressure on the tibial bearing component. The influence of thickness of the tibial bearing component on the contact pressure distribution in fixed- and mobile-bearing implant is not changed in the case of overweight.

The influence of body weight on contact pressure distributions in the fixed- and mobile-bearing implant are investigated in Chapter 8. Maximum contact pressures in the mobile-bearing implant are almost the same as those in the fixed-bearing implant in the normal weight condition. A smaller increase in maximum contact pressure is found in the mobile-bearing implant compared to the fixed-bearing implant with the increase in body weight. In condition of overweight, the maximum contact pressure in the mobile-bearing implant is less than that in the fixed-bearing implant. Therefore, less influence of body weight on the maximum contact pressure is found in the mobile-bearing implant.

In conclusion, fixed- and mobile-bearing implants demonstrate different performance of movement and contact pressure distribution on the tibio-femoral

contact surface. In the fixed-bearing implant, less rotation of the tibial tray is observed. It is found that the higher rotation of the tibial tray in the mobile-bearing implant, however the relative movement between the femoral component and the tibial bearing component, the tibial bearing component and the tibial tray are smaller than the relative motion between the femoral component and the tibial bearing component in the fixed-bearing implant. More contact areas are observed in the mobile-bearing implant, less wear will be take place in mobile-bearing implant due to maximum contact pressure on the superior surface of mobile-bearing implant were much less than that of the fixed-bearing implant during most of the stance phase of the gait. The thickness of the tibial bearing implant has different influence on fixed- and mobile-bearing implant. A 9.6 mm thick tibial bearing component is suggested for the fixed-bearing implant, whereas a 6.8 mm thick one is suggested for the mobile-bearing implant. Contact pressure increases in condition of varus/valgus malalignment in the dynamic models of both the fixed- and mobile-bearing implant. Less influence of body weight on maximum contact pressure is found in the mobile-bearing implant.

9.2 Stress distribution in distal femur

A dynamic model of the knee joint has been developed with MSC/ADAMS and MSC/MARC software. In this model, the distal femur is modelled as a flexible body and the stress distribution in the distal femur during daily activities has been analysed. Using this dynamic model, a gait cycle load of normal walking has been successfully simulated.

There is a decrease in stress in the distal margin of the bone adjacent to the implant; this proves that there is stress shielding in the distal femur. Higher stresses are identified around the femoral component pegs. The rate of bone mass change in different zones of the distal femur indicates bone loss at the distal end of the femur. Because the stress distribution in the distal femur in this dynamic model is consistent with other investigators' research findings, the dynamic model in this paper can be used to analyse stress distribution in the

distal femur with different dynamic load conditions and optimize implant designs.

Different designs of femoral component peg have been analysed using the dynamic model of the implanted knee joint. The influence of the geometry of the femoral component peg on stress distribution in the distal femur was investigated. Stress shielding occurs at the distal end of femur in all designs. Based on the investigated peg designs, the stress shielding at the distal end of femur can not be improved effectively. In the small_long peg design, the rate of bone mass change is much higher in the bone at the top of the peg compared to intact bone. This increase in bone density may help stabilize the femoral component of the knee prosthesis. Increase of bone density also appears in the bone at the top of the peg in the big_long peg design; however, more bone is removed and serious stress shielding is found in this design. The big_long peg design is not recommended. These conclusions are based on the numerical finite element models; performance of different designs needs to be further tested experimentally.

In dynamic analysis of implanted knee joints, the stresses and strains in the distal femur are found to increase with body weight, especially during the stance phase of the gait cycle. However, the bone structure in the distal femur will not fracture according to the present investigation during a walking gait cycle. Serious stress shielding appears in the case of overweight. More bone loss and higher stress at the distal end of femur in condition of overweight will result in a higher risk of migration of femoral component after total knee replacement.

Varus/valgus malalignment will redistribute the tibio-femoral contact force and stress/strain distribution in the distal femur. The difference in contact force between the medial and lateral condyles decreases in condition of valgus malalignment compared with normal and varus conditions during the stance phase. In all normal and malalignment conditions, bone loss will occur at the distal end of the femur.

In conclusion, finite element models of a total knee replacement have been successfully developed in this thesis; the numerical results have been validated against other research work and findings. This is the first time that stress analysis in a total knee replacement has been analysed during a gait cycle. The dynamic model of the implanted knee joint can be used to predict stress distribution in the distal femur with different load conditions such as obesity. This research provides a very important method for conducting detailed analysis of interactions between bone and implant, particularly the bone remodelling process around the implant since stress energy density at every stage of daily activity can be obtained.

Chapter 10

Future Work

Stress distribution in the distal femur after TKR can be investigated using the dynamic model of an implanted knee joint developed in this research. Future work should consider other daily activities and load cases to study bone remodelling in the distal femur.

In this research, the bone mass change rate was used as an indicator for the bone remodelling process. Future work should integrate the bone iterative remodelling programme with the FE model.

The stress distribution in the proximal tibia and the influence of peg design on it should be investigated in future using a similar approach to that employed in this thesis. Micromotion and aseptic loosening in an implanted knee should be simulated.

Future work on investigation of the influence of obesity on TKR in the dynamic model of the implanted knee joint, and comparison of the fixed-bearing and mobile-bearing implant in obese patients should use the gait cycle load obtained from obese TKR patients.

References

ABERNETHY, P. J., ROBINSON, C. M. and FOWLER, R. M. (1996) Fracture of the metal tibial tray after kinematic total knee replacement. A common cause of early aseptic failure. *Journal of Bone and Joint Surgery (British)*, **78**, pp. 220-225.

AKAMATSU, Y., KOSHIPO, T., SAITO, T. and WADA, J. (1997) Changes in osteosclerosis of osteoarthritic knee after high tibial osteotomy. *Clinical Orthopaedics and Related Research*, **334**, pp. 207-214.

ALTINTAS, F., SENER, N. and UGUTMEN, E. (1999a) Evaluation of a testing method for the fatigue performance of total knee tibial trays. *The Journal of Arthroplasty*, **14**, pp. 112-114.

ALTINTAS, F., SENER, N. and UGUTMEN, E. (1999b) Fracture of the tibial tray after total knee arthroplasty. *The Journal of Arthroplasty*, **14**(1), pp. 112-114.

ANON. (2002) *Virtual Animation of the Kinematics of the Human for Industrial, Educational and Research Purposes.* University of Brussels.

ARGENSON, J. N. and O'CONNOR, J. J. (1992) Polyethylene wear in meniscal knee replacement: A one to nine-year retrieval analysis of the Oxford knee. *Journal of Bone and Joint Surgery (British)*, **74**, pp. 228-232.

BARBOUR, P. S. M., BARTON, D. C. and FISHER, J. (1997) The influence of stress conditions on the wear of UHMWPE for total joint replacments. *Journal of Materials Sciences: Material in Medicine*, **8**, pp. 603-611.

BARTEL, D. L., BICKNELL, V. L. and WEIGHT, T. M. (1986) The effect of conformity, thickness, and material on stresses in ultra-high molecular weight components for total joint replacement. *Journal of Bone and Joint Surgery (Am)*, **68**, pp. 1041-1051.

BARTEL, D. L., RAWLINSON, J. J. and BURSTEIN, A. H. (1995) Stresses in polyethylene components of contemporary total knee replacements. *Clinical Orthopaedics and Related Research*, **317**, pp. 76-82.

BEI, Y., FREGLY, B. J., SAWYER, W. G., BANKS, S. A. and KIM, N. H. (2004) The relationship between contact pressure, insert thickness, and

mild wear in total knee replacements. *Computer Modeling in Engineering & Sciences*, **6**, pp. 145-152.

BEILLAS, P., PAPAIOANNOU, G., TASHMAN, S. and YANG, K. H. (2004) A new method to investigate in vivo knee behavior using a finite element model of the lower limb. *Journal of Biomechanics*, **37**(7), pp. 1019-1030.

BERGMANN, G., DEURETZBACHER, G., HELLER, M. O., GRAICHEN, F., ROHLMANN, A., STRAUSS, J. and DUDA, G. N. (2001) Hip contact forces and gait patterns from routine activities. *Journal of Biomechanics*, **34**, pp. 859-871.

BLANKEVOORT, L. and HUISKES, R. (1996) Validation of a three-dimensional model of the knee. *Journal of Biomechanics*, **29**(7), pp. 955-961.

BLUNN, G. W., JOSHI, A. B., MINNS, R. J., LIDGREN, L., LILLEY, P., RYD, L., ENGELBRECHT, E. and WALKER, P. S. (1997) Wear in retrieved condylar knee arthroplasties: A comparison of wear in different designs of 280 retrieved condylar knee prostheses. *The Journal of Arthroplasty*, **12**(3), pp. 281-290.

BOBYN, J. D., CAMERON, H. U. and ABDULLA, D. (1982) Biologic fixation and bone modeling with an unconstrained canine total knee prosthesis. *Clinical Orthopaedics and Related Research*, **166**, pp. 301-312.

BRYAN, R. S. and RAND, J. A. (1982) Revision total knee arthroplasty. *Clinical Orthopaedics*, **170**, pp. 116-122.

CALLAGHAN, J. J., O'ROURKE, M. R. and SALEH, K. J. (2004) Why knees fail: Lessons learned. *The Journal of Arthroplasty*, **19**(4, Supplement 1), pp. 31-34.

CAMERON, H. U. and CAMERON, G. (1987) Stress-relief osteoporosis of the anterior femoral condyles in total knee replacement. *Orthop Rev*, **16**, pp. 449-456.

CHATTERJI, U., ASHWORTH, M. J., SMITH, A. L., BREWSTER, N. and LEWIS, P. L. (2005) Retrieval study of tibial baseplate fracture after total knee arthroplasty. *The Journal of Arthroplasty*, **20**(1), pp. 101-107.

CHEN, F. and KRACKOW, K. A. (1994) Management of tibial defects in total knee arthroplasty. *Clinical Orthopaedics and Related Research*, **305**, pp. 249-257.

CHENG, C. K., HUANG, C. H., LIAU, J. J. and HUANG, C. H. (2003) The influence of surgical malalignment on the contact pressures of fixed and mobile bearing knee prostheses--a biomechanical study. *Clinical Biomechanics*, **18**(3), pp. 231-236.

CHOCKALINGAM, S. and SCOTT, G. (2000) The outcome of cemented vs. cementless fixation of a femoral component in total knee replacement (TKR) with the identification of radiological signs for the prediction of failure. *The Knee*, **7**(4), pp. 233-238.

COLLIER, J. P., MAYOR, M. B., MCNAMARA, J. L., SURPRENANT, V. A. and JENSEN, R. E. (1991) Analysis of the failure of 122 polyethylene inserts from uncemented tibial knee components. *Clinical Orthopaedics and Related Research*, **273**, pp. 232-242.

COWIN, S. C. and HEGEDUS, D. H. (1976) Bone remodeling I: theory of adaptive elasticity. *Journal of Elasticity*, **6**, pp. 313-326.

DESHMUKH, R. G., HAYES, J. H. and PINDER, I. M. (2002) Does body weight influence outcome after total knee arthroplasty? A 1-year analysis. *The Journal of Arthroplasty*, **17**(3), pp. 315-319.

DESJARDINS, J. D., WALKER, P. S., HAIDER, H. and PERRY, J. (2000) The use of a force-controlled dynamic knee simulator to quantify the mechanical performance of total knee replacement designs during functional activity. *Journal of Biomechanics*, **33**(10), pp. 1231-1242.

DEVITA, P. and HORTOBAGYI, T. (2003) Obesity is not associated with increased knee joint torque and power during level walking. *Journal of Biomechanics*, **36**(9), pp. 1355-1362.

D'LIMA, D. D., CHEN, P. C. and COLWELL, C. W. (2001) Polyethylene contact stresses, articular congruity, and knee alignment. *Clinical Orthopaedics and Related Research*, **392**, pp. 232-238.

D'LIMA, D. D., TRICE, M., URQUHART, A. G. and COLWELL, C. W. J. (2000) Comparison between the kinematics of fixed and rotating bearing

knee prostheses. *Clinical Orthopaedics and Related Research*, **380**, pp. 151-157.

EL-DEEN, M., GARCIA-FINANA, M. and JIN, Z. M. (2006) Effect of ultra-high molecular weight polyethylene thickness on contact mechanics in total knee replacement. *Proceedings of the I MECH E Part H Journal of Engineering in Medicine*, **220**, pp. 733-742.

ENGH, G. A., DWYER, K. A. and HANES, C. K. (1992) Polyethylene wear of metal-back tibial components in total and uni-compartmental knee prostheses. *Journal of Bone and Joint Surgery*, **74B**, pp. 9-17.

ESSNER, A., KLEIN, R., BUSHELOW, M., WANG, A., KVITNITSKY, M. and MAHONEY, O. (2003) The effect of sagittal conformity on knee wear. *Wear*, **255**(7-12), pp. 1085-1092.

ESTUPINAN, J. A., BARTEL, D. L. and WRIGHT, T. M. (1998) Residual stresses in ultra-high molecular weight polyethylene loaded cyclically by a rigid moving indentor in nonconforming geometries. *Journal of Orthopaedic Research*, **16**, pp. 80-88.

FERHRING, T. K. and MCAVOY, G. (1996) Fluoroscopic evaluation of the painful total knee arthroplasty. *Clinical Orthopaedics and Related Research*, **331**, pp. 226-233.

FORAN, J. R. H., MONT, M. A., RAJADHYAKSHA, A. D., JONES, L. C., ETIENNE, G. and HUNGERFORD, D. S. (2004) Total knee arthroplasty in obese patients: A comparison with a matched control group. *The Journal of Arthroplasty*, **19**(7), pp. 817-824.

FORD, C. M. and KEAVENY, T. M. (1996) The dependence of shear failure properties of trabecular bone on apparent density and trabecular orientation. *Journal of Biomechanics*, **29**(10), pp. 1309-1317.

FREGLY, B. J. 1999 *A three-dimensional compliant contact model for dynamic simulation of total knee replacements.* University of Calgary, Calgary, Alberta, Canada.

FREGLY, B. J., BEI, Y. and SYLVESTER, M. E. (2003) Experimental evaluation of an elastic foundation model to predict contact pressures in knee replacements. *Journal of Biomechanics*, **36**(11), pp. 1659-1668.

FREGLY, B. J., SAWYER, W. G., HARMAN, M. K. and BANKS, S. A. (2005) Computational wear prediction of a total knee replacement from in vivo kinematics. *Journal of Biomechanics*, **38**, pp. 305-314.

FUIKO, R., ZEMBSCH, A., LOYODDIN, M. and RITSCHL, P. (2003) Osteointegration and implant position after cementless total knee replacement. *Clinical Orthopaedics and Related Research*, **408**, pp. 201-208.

FYHRIE, D. P., CARTER, D.R. (1986) A unifying principle relating stress to trabecular bone morphology. *Journal of Orthopaedic Research*, **4**, pp. 304-317.

FYHRIE, D. P. and VASHISHTH, D. (2000) Bone stiffness predicts strength similarly for human vertebral cancellous bone in compression and for cortical bone in tension. *Bone*, **26**(2), pp. 169-173.

GALIK, K. (2002) *The effect of design variations on stresses in total ankle arthroplasty.* Doctor of Philosophy Thesis, University of Pittsburgh.

GODEST, A. C., BEAUGONIN, M., HAUG, E., TAYLOR, M. and GREGSON, P. J. (2002) Simulation of a knee joint replacement during a gait cycle using explicit finite element analysis. *Journal of Biomechanics*, **35**(2), pp. 267-275.

GOLDSTEIN, S. A., WILSON, D. L., SONSTEGART, D. A. and MATTHEWS, L. S. (1983) The mechanical properties of human tibial trabecular bone as a function of metaphyseal location. *Journal of Biomechanics*, **16**, pp. 965-969.

GRIFFIN, F. M., SCUDERI, G. R., INSALL, J. N. and COLIZZA, W. (1998) Total knee arthroplasty in patients who were obese with 10 years follow up. *Clinical Orthopaedics and Related Research*, **356**, pp. 28-33.

GUPTA, S., NEW, A. M. R. and TAYLOR, M. (2006) Bone remodelling inside a cemented resurfaced femoral head. *Clinical Biomechanics*, **21**(6), pp. 594-602.

HAIDER, H., WALKER, P. S., BLUNN, G. W. and BELL, C. J. 2001 *The sensitivity of total knee replacement kinematics to misaligned installation*. San Francisco, California.

HALLORAN, J. P., PETRELLA, A. J. and RULLKOETTER, P. J. (2005) Explicit finite element modeling of total knee replacement mechanics. *Journal of Biomechanics*, **38**(2), pp. 323-331.

HARMAN, M. K., BANKS, S. A. and HODGE, W. A. (2001) Polyethylene damage and knee kinematics after total knee arthroplasty. *Clinical Orthopaedics and Related Research*, **392**, pp. 383-393.

HARRISON, M. M., MORRELL, J. and HOPMAN, W. M. (2004) Influence of obesity on outcome after knee arthroscopy. *Arthroscopy: The Journal of Arthroscopic & Related Surgery*, **20**(7), pp. 691-695.

HAZELWOOD, S. J., MARTIN, R. B., RASHID, M. M. and RODRIGO, J. J. (2001) A mechanistic model for internal bone remodeling exhibits different dynamic responses in disuse and overload. *Journal of Biomechanics*, **34**, pp. 299-308.

HEALY, W. L., WASILEWSKI, S. A., TAKEI, R. and OBERLANDER, M. (1995) Patellofemoral complications following total knee arthroplasty: Correlation with implant design and patient risk factors. *The Journal of Arthroplasty*, **10**(2), pp. 197-201.

HOPPENFELD, S. (1976) *Physical examination of the spine and extremities.* Prentice Hall.

HUISKES, R., WEINANS, H. and DALSTRA, M. (1989) Adaptive bone remodeling and biomechanical design considerations for noncemented total hip arthroplasty. *Orthopaedics*, **12**, pp. 1255-1267.

HUISKES, R., WEINANS, H., GROOTENBOER, H. J., DALSTRA, M., FUDALA, B. and SLOOF, T. J. (1987) Adaptive bone remodelling theory applied to prosthetic-design analysis. *Journal of Biomechanics*, **20**, pp. 1135-1150.

HURWITZ, D. E., SUMNER, D. R., ANDRIACCHI, T. P. and SUGAR, D. A. (1998) Dynamic knee loads during gait predict proximal tibial bone distribution. *Journal of Biomechanics*, **31**(5), pp. 423-430.

ISHIKAWA, H., FUJIKI, H. and YASUDA, K. (1996) Contact analysis of ultrahigh molecular weight polyethylene articular plate in artificial knee

joint during gait movement. *Journal of Biomechanical Engineering*, **118**, pp. 377-386.

JIN, Z. M., DOWSON, D. and FISHER, J. (1995a) Contact pressure prediction in total knee joint replacements. Part 1: general elasticity solution for elliptical layered contact. *Proceedings of the I MECH E Part H Journal of Engineering in Medicine*, **209**, pp. 1-8.

JIN, Z. M., STEWART, T., AUGER, D. D. and DOWSON, D. (1995b) Contact pressure prediction in total knee joint replacements. Part 2: application to the design of total knee joint replacements. *Proceedings of the I MECH E Part H Journal of Engineering in Medicine*, **209**, pp. 9-15.

JONES, V. C., BARTON, D. C., FITZPATRICK, D. P., AUGER, D. D., STONE, M. H. and FISHER, J. (1999) An experimental model of tibial counterface polyethylene wear in mobile bearing knees: The influence of design and kinematics. *Bio-Medical Materials and Engineering*, **9**(3), pp. 189-196.

KEAVENY, T. M., WACHTEL, E. F., FORD, C. M. and HAYES, W. C. (1994) Differences between the tensile and compressive strengths of bovine tibial trabecular bone depend on modulus. *Journal of Biomechanics*, **27**(9), pp. 1137-1146.

KNIGHT, L. A., PAL, S., COLEMAN, J. C., BRONSON, F., HAIDER, H., LEVINE, D. L., TAYLOR, M. and RULLKOETTER, P. J. (2007) Comparison of long-term numerical and experimental total knee replacement wear during simulated gait loading. *Journal of Biomechanics*, **40**, pp. 1550-1558.

KOPPERDAHL, D. L. and KEAVENY, T. M. (1998) Yield strain behavior of trabecular bone. *Journal of Biomechanics*, **31**(7), pp. 601-608.

KRAAY, M. J., GOLDBERG, V. M., FIGGIE, M. P. and FIGGIE, I., HARRY E. (1992) Distal femoral replacement with allograft/prosthetic reconstruction for treatment of supracondylar fractures in patients with total knee arthroplasty. *The Journal of Arthroplasty*, **7**(1), pp. 7-16.

KROHN, K. (2005) Footwear alterations and bracing as treatments for knee osteoarthritis. *Current Opinion in Rheumatology*, **17**(5), pp. 653-656.

KUSTER, M. S., WOOD, G. A., STACHOWIAK, G. W. and GACHTER, A. (1997) Joint load considerations in total knee replacement. *Journal of Bone and Joint Surgery (Am)*, **79**(1), pp. 109-113.

LAFORTUNE, M. A., *ET AL*. (1992) Three-dimensional kinematics of the human knee during walking. *Journal of Biomechanics*, **25**(4), pp. 347-357.

LAZ, P. J., PAL, S., HALLORAN, J. P., PETRELLA, A. J. and RULLKOETTER, P. J. (2006) Probabilistic finite element prediction of knee wear simulator mechanics. *Journal of biomechanics*, **39**, pp. 2303-2310.

LEVITZ, C. L., LOTKE, P. A. and KARP, J. S. (1995) Long-term changes in bone mineral density following total knee replacement. *Clinical Orthopaedics*, **321**, pp. 68-72.

LI, M. G. and NILSSON, K. G. (2000) The effect of the preoperative bone quality on the fixation of the tibial component in total knee arthroplasty. *The Journal of Arthroplasty*, **15**(6), pp. 744-753.

LI, M. G. and NILSSON, K. G. (2001) No relationship between postoperative changes in bone density at the proximal tibia and the migration of the tibial component 2 years after total knee arthroplasty. *The Journal of Arthroplasty*, **16**(7), pp. 893-900.

LIAU, J. J., CHENG, C. K., HUANG, C. H., LEE, Y. M., CHUEH, S. C. and LO, W. H. (1999) The influence of contact alignment of the tibiofemoral joint of the prostheses in in vitro biomechanical testing. *Clinical Biomechanics*, **14**(10), pp. 717-721.

LIAU, J. J., CHENG, C. K., HUANG, C. H. and LO, W. H. (2002) The effect of malalignment on stresses in polyethylene component of total knee prostheses - a finite element analysis. *Clinical Biomechanics*, **17**(2), pp. 140-146.

LINDE, F., HVID, I. and MADSEN, F. (1992) The effect of specimen geometry on the mechanical behaviour of trabecular bone specimens. *Journal of Biomechanics*, **25**(4), pp. 359-368.

MARUYAMA, M., TERAYAMA, K., SUNOHARA, H., ADACHI, T., SUZUKI, S. and FUKUZAWA, T. (1994) Fracture of the tibial tray following PCA knee replacement. A report of two cases. *Archives of Orthopaedic and Trauma Surgery*, **113**(6), pp. 330-333.

MCEWEN, H. M. J., BARNETT, P. I., BELL, C. J., FARRAR, R., AUGER, D. D., STONE, M. H. and FISHER, J. (2005) The influence of design, materials and kinematics on the in vitro wear of total knee replacements. *Journal of Biomechanics*, **38**(2), pp. 357-365.

MCEWEN, H. M. J., FISHER, J., GLODSMITH, A. A. J., AUGER, D. D. and HARDAKER, C. (2001) Wear of fixed bearing and rotating platform mobile bearing knees subjected to high levels of internal and external tibial rotation. *Journal of Materials Sciences: Material in Medicine*, **12**, pp. 1049-1052.

MCGRAW, B. and MCCLENAGHAN, B. A. (2000) Gait and postural stability in obese and nonobese prepubertal boys. *Archives of Orthopaedic and Trauma Surgery*, **81**, pp. 484-489.

MINTZER, C. M., ROBERTSON, D. D. and RACKEMANN, S. (1990) Bone loss in the distal anterior femur after total knee arthroplasty. *Clinical Orthopaedics and Related Research*, **260**, pp. 135-143.

MOEINZADEH, M. H., ENGIN, A. E. and AKKAS, N. (1983) Two-dimensional dynamic modelling of human knee joint. *Journal of Biomechanics*, **16**(4), pp. 253-264.

MOGLO, K. E. and SHIRAZI-ADL, A. (2003) On the coupling between anterior and posterior cruciate ligaments, and knee joint response under anterior femoral drawer in flexion: a finite element study. *Clinical Biomechanics*, **18**(8), pp. 751-759.

MOMMERSTEEG, T. J. A., HUISKES, R., BLANKEVOORT, L., KOOLOOS, J. G. M., KAUER, J. M. G. and MAATHUIS, P. G. M. (1996) A global verification study of a quasi-static knee model with multi-bundle ligaments. *Journal of Biomechanics*, **29**(12), pp. 1659-1664.

MONT, M. A., MATHUR, S. K., KRACKOW, K. A., LOEWY, J. W. and HUNGERFORD, D. S. (1996) Cementless total knee arthroplasty in

obese patients: A comparison with a matched control group. *The Journal of Arthroplasty*, **11**(2), pp. 153-156.

MORGAN, E. F. and KEAVENY, T. M. (2001) Dependence of yield strain of human trabecular bone on anatomic site. *Journal of Biomechanics*, **34**(5), pp. 569-577.

MORRISON, J. B. (1970) The mechanics of the knee joint in relation to normal walking,. *Journal of Biomechanics*, **3**, pp. 51-61.

MURATOGLU, O. K., RUBERTI, J., MELOTTI, S., SPIEGELBERG, S. H., GREENBAUM, E. S. and HARRIS, W. A. (2003) Optical analysis of surface changes on early retrievals of highly cross-linked and conventional polyethylene tibial inserts. *Journal of Arthroplasty*, **7**(1), pp. 42-47.

NAMBA, R. S., PAXTON, L., FITHIAN, D. C. and STONE, M. L. (2005) Obesity and perioperative morbidity in total hip and total knee arthroplasty patients. *The Journal of Arthroplasty*, **20**(Supplement 3), pp. 46-50.

NILLSON, K. G., KARRHOLM, J. and LINDER, L. (1995) Femoral component migration in total knee arthroplasty: randomized study comparing cemented and uncemented fixation of the Miller-Galante I design. *Journal of Orthopaedic Research*, **13**, pp. 347-356.

NYMAN, J. S., HAZELWOOD, S. J., RODRIGO, J. J., MARTIN, R. B. and YEH, O. C. (2004) Long stemmed total knee arthroplasty with interlocking screws: a computational bone adaptation study. *Journal of Orthopaedic Research*, **22**(1), pp. 51-57.

OTTO, J. K., CALLAGHAN, J. J. and BROWN, T. D. (2001) Mobility and contact mechanics of a rotating platform total knee replacement. *Clinical Orthopaedics and Related Research*, **392**, pp. 24-37.

OTTO, J. K., CALLAGHAN, J. J. and BROWN, T. D. (2003) Gait cycle finite element comparison of rotating-platform total knee designs. *Clinical Orthopaedics and Related Research*, **410**, pp. 181-188.

PAUL, J. P. 1967 *Forces transmitted by joints in the human body*.

PERILLO-MARCONE, A., BARRETT, D. S. and TAYLOR, M. (2000) The importance of tibial alignment. *The Journal of Arthroplasty*, **15**(8), pp. 1020-1027.

PERILLO-MARCONE, A., RYD, L., JOHNSSON, K. and TAYLOR, M. (2004) A combined RSA and FE study of the implanted proximal tibia: correlation of the post-operative mechanical environment with implant migration. *Journal of Biomechanics*, **37**(8), pp. 1205-1213.

PERILLO-MARCONE, A. and TAYLOR, M. (2007) Effect of varus/valgus malalignment on bone strains in the proximal tibia after TKR: an explicit finite element study. *Journal of Biomechanical Engineering*, **129**(1), pp. 1-11.

PETERSEN, M. M., OLSEN, C., LAURITZEN, J. B. and LUND, B. (1995) Changes in bone mineral density of the distal femur following uncemented total knee arthroplasty. *The Journal of Arthroplasty*, **10**(1), pp. 7-11.

PETTY, W., MILLER, G. J., BARTEL, D. L., WRIGHT, T. M. and BURSTEIN, A. H. (1999) Total knee contact pressures: the effect of congruity and alignment. *Medscape General Medicine*, **1**(1), http://www.medscape.com/viewarticle/431538.

PIAZZA, S. J. and DELP, S. L. (2001) Three-dimensional dynamic simulation of total knee replacement motion during a step-up task. *Journal of Biomechanical Engineering*, **123**, pp. 599-606.

PLANTE-BORDENEUVE, P. and FREEMAN, M. A. (1993) Tibial high-density polyethylene wear in conforming tibiofemoral prostheses. *Journal of Bone and Joint Surgery (British)*, **75**, pp. 630-636.

RAWLINSON, J. J. and BARTEL, D. L. (2002) Flat medial-lateral conformity in total knee replacements does not minimize contact stresses. *Journal of Biomechanics*, **35**(1), pp. 27-34.

REEVES, E. A., BARTON, D. C., FITZPATRICK, D. P. and FISHER, J. (1998) A two dimensional model of cyclic strain accumulation in ultra-high molecular weight polyethylene knee replacements. *Proceedings of*

the Institute of Mechanical Engineers, Part H, Journal of Engineering in Medicine, **212**, pp. 189-198.

REILLY, D. T. and BURSTEIN, A. H. (1975) The elastic and ultimate properties of compact bone tissue. *Journal of Biomechanics*, **8**, pp. 393-405.

RIETBERGEN, B., HUISKES, R., WEINANS, H., SUMNER, D. R., TURNER, T. M. and GALANTE, J. O. (1993) The mechanism of bone remodelling and resorption around press-fitted THA stems. *Journal of Biomechanics*, **26**, pp. 369-382.

RYD, L., ALBREKTSSON, B. E. J. and CARLSSON, L. (1995) Roentgen stereophotogrammetric analysis as a predictor of mechanical loosening of knee prostheses. *Journal of Bone and Joint Surgery (British)*, **77**, pp. 377-383.

SATHASIVAM, S. and WALKER, P. S. (1997) A computer model with surface friction for the prediction of total knee kinematics. *Journal of Biomechanics*, **30**(2), pp. 177-184.

SATHASIVAM, S. and WALKER, P. S. (1998) Computer model to predict subsurface damage in tibial inserts of. *Journal of Orthopaedic Research*, **16**, pp. 564-571.

SATHASIVAM, S., WALKER, P. S., CAMPBELL, P. A. and RAYNER, K. (2001) The effect of contact area on wear in relation to fixed bearing and mobile bearing knee replacements. *Journal of Biomedical Materials Research*, **58**(3), pp. 282-290.

SCHIPPLEIN, O. D. and ANDRIACCHI, T. P. (1991) Interaction between active and passive knee stabilizers during level walking. *Journal of Orthopaedic Research*, **9**(1), pp. 113-119.

SHARKEY, P. F., HOZACK, W. J. and ROTHMAN, R. H. 2002 *Why are knee replacements failing today?* Dallas, Texas.

SHI, J. F., WANG, C. J., LAOUI, T., HALL, R. and HART, W. 2005 *The Influence of Surgical Malalignment on the stress distribution in the fixed and mobile bearing knee implants*. The Royal College of Surgeons, UK.

SOININVAARA, T. A., MIETTINEN, H. J. A., JURVELIN, J. S., SUOMALAINEN, O. T., ALHAVA, E. M. and KROGER, H. P. J. (2004) Periprosthetic femoral bone loss after total knee arthroplasty: 1-year follow-up study of 69 patients. *The Knee*, **11**(4), pp. 297-302.

SPITTLEHOUSE, A. J., GETTY, C. J. and EASTELL, R. (1999) Measurement of bone mineral density by dual-energy x-ray absorptiometry around an uncemented knee prosthesis. *The Journal of Arthroplasty*, **14**(8), pp. 957-963.

SPYROPOULOS, P., PISCIOTTA, J. C., PAVLOU, K. N., CAIRNS, M. A. and SIMON, S. R. (1991) Biomechanical gait analysis in obese men. *Arch Phys Med Rehabil*, **72**, pp. 1065-1070.

STIEHL, J. B., DENNIS, D. A., KOMISTEK, R. D. and KEBLISH, P. A. (1997) In vivo kinematic analysis of a mobile bearing total knee prosthesis. *Clinical Orthopaedics and Related Research*, **345**, pp. 60-66.

TAYLOR, M. and BARRETT, D. S. (2003) Explicit finite element simulation of eccentric loading in total knee replacement. *Clinical Orthopaedics and Related Research*, **414**, pp. 162-171.

TAYLOR, M. and TANNER, K. E. (1997) Fatigue failure of cancellous bone: a possible cause of implant migration and loosening. *Journal of Bone and Joint Surgery (British)*, **79**, pp. 181-182.

TAYLOR, M., TANNER, K. E. and FREEMAN, M. A. R. (1998) Finite element analysis of the implanted proximal tibia: a relationship between the initial cancellous bone stresses and implant migration. *Journal of Biomechanics*, **31**(4), pp. 303-310.

TAYLOR, W. R., HELLER, M. O., BERGMANN, G. and DUDA, G. N. (2004) Tibio-femoral loading during human gait and stair climbing. *Journal of Orthopaedic Research*, **22**(3), pp. 625-632.

TERRIER, A. (1999) *Adaptation of bone to mechanical stress: theoretical model, experimental identification and orthopedic application.* PhD Thesis Thesis, Swiss Federal Institute of Technology.

TISSAKHT, M., ESKANDARI, H. and AHMED, A. M. (1995) Micromotion analysis of the fixation of total knee tibial component. *Computers & Structures*, **56**, pp. 365-375.

VAN LENTHE, G. H., DE WALL MALEFIJT, M. C. and HUISKES, R. (1997) Stress shielding after total knee replacement may cause bone resorption in the distal femur. *The Journal of Bone and Joint Surgery*, **79-B**(1), pp. 117-122.

VAN LENTHE, G. H., WILLEMS, M. M. M., VERDONSCHOT, N., DE WAAL MALEFIJT, M. C. and HUISKES, R. (2002) Stemmed femoral knee prostheses. *Acta Orthopaedica Scandinavica Supplementum*, **73**(6), pp. 630-637.

VAN RIETBERGEN, B. and HUISKES, H. W. J. (2001) Load transfer and stress shielding of the hydroxyapatite-ABG hip: a study of stem length and proximal fixation. *The Journal of Arthroplasty*, **16**(8), pp. 55-63.

VAN RIETBERGEN, B., HUISKES, R., WEINANS, H., SUMNER, D. R., TURNER, T. M. and GALANTE, J. O. (1993) The mechanism of bone remodeling and resorption around press-fitted THA stems. *Journal of Biomechanics*, **26**(4-5), pp. 369-382.

VILLA, T., MIGLIAVACCA, F., GASTALDI, D., COLOMBO, M. and PIETRABISSA, R. (2004) Contact stresses and fatigue life in a knee prosthesis: comparison between in vitro measurements and computational simulations. *Journal of Biomechanics*, **37**(1), pp. 45-53.

VINCE, K. G. (2003) Why knees fail. *The Journal of Arthroplasty*, **18**(3, Part 2), pp. 39-44.

WALKER, P. S., BLUNN, G. W., BROOME, D. R., PERRY, J., WATKINS, A., SATHASIVAM, S., DEWAR, M. E. and PAUL, J. P. (1997) A knee simulating machine for performance evaluation of total knee replacements. *Journal of Biomechanics*, **30**(1), pp. 83-89.

WALKER, P. S., BLUNN, G. W. and PERRY, J. (2000a) Methodology for long-term wear testing of total knee replacements. *Clinical Orthopaedics and Related Research*, **372**, pp. 290-301.

WALKER, P. S. and SATHASIVAM, S. (2000) Design forms of total knee replacement. *Proceedings of the I MECH E Part H Journal of Engineering in Medicine*, **214**(1), pp. 101-119.

WALKER, P. S., SATHASIVAM, S., COBB, A., LEARMONTH, I. D., GROBLER, G. P., PINDER, I. M., MARCHETTI, N., SPINELLI, M. D. and WELSBY, A. (2000b) A comparison between cemented, press-fit, and HA-coated interfaces in Kinemax total knee replacement. *The Knee*, **7**(2), pp. 71-78.

WANG, A., STARK, C. and DUMBLETON, J. (1996) Mechanistic and morphological origins of ultra-high molecular weight polyethylene wear debris in total joint replacement prostheses. *Proceedings of the I MECH E Part H Journal of Engineering in Medicine*, **210**, pp. 141-155.

WASIELEWSKI, R. C., GALANTE, J. O., LEIGHTY, R. B., NATARAJAN, R. N. and ROSENBERG, A. G. (1994) Wear patterns on retrieved polyethylene tibial inserts and their relationship to technical considerations during total knee arthroplasty. *Clinical Orthopaedics*, **299**, pp. 31-43.

WEINANS, H., HUISKES, R. and GROOTENBOER, H. J. (1992) The behavior of adaptive bone-remodeling simulation models. *Journal of Biomechanics*, **25**, pp. 1425-1441.

WERNER, F. W., AYERS, D. C., MALETSKY, L. P. and RULLKOETTER, P. J. (2005) The effect of valgus/varus malalignment on load distribution in total knee replacements. *Journal of Biomechanics*, **38**(2), pp. 349-355.

WINDSOR, R. E., SCUDERI, G. R., MORAN, M. C. and N., I. J. (1989) Mechanisms of failure of the femoral and tibial components in total knee arthroplasty. *Clinical Orthopaedics*, **248**, pp. 15-19.

WINTER, D. A. (1990) *Biomechanics and motor control of human movement, 2nd ed.* New York: John Wiley & Sons.

WOLFF, J. L. (1986) *The law of bone remodelling.* Springer, Berlin.

WOOLSON, S. T. and NORTHROP, G. D. (2004) Mobile- vs. fixed-bearing total knee arthroplasty: a clinical and radiologic study. *The Journal of Arthroplasty*, **19**(2), pp. 135-140.

WRIGHT, T. M. and BARTEL, D. L. (1986) The problem of surface damage in polyethylene total knee components. *Clinical Orthopaedics*, **205**, pp. 67-74.

YANG, R.-S. and LIN, H.-J. (2001) Contact stress on polyethylene components of a new rotating hinge with a spherical contact surface. *Clinical Biomechanics*, **16**(6), pp. 540-546.

ZIHLMANN, M. S., STACOFF, A., ROMERO, J., QUERVAIN, I. K.-D. and STUSSI, E. (2005) Biomechanical background and clinical observations of rotational malalignment in TKA: Literature review and consequences. *Clinical Biomechanics*, **20**(7), pp. 661-668.

Publication

SHI, J. F., WANG, C. J., LAOUI, T., HALL, R. and HART, W. 2005 *The Influence of Surgical Malalignment on the stress distribution in the fixed and mobile bearing knee implants*. Knee Arthroplasty: Engineering Functionality 7-9 April 2005, The Royal College of Surgeons, London, UK. pp 146-149.

SHI, J. F., WANG, C. J., LAOUI, T., HALL, R. and HART, W. *A dynamic model of simulating stress distribution in the distal femur after total knee replacement*. Accepted by: Proceedings of the Institution of Mechanical Engineers, Part H, Journal of Engineering in Medicine.